Evaluating the performance of nanostructured materials as lithium-ion battery electrodes.

Mark J. Armstrong[1], Colm O'Dwyer[1], William J. Macklin[3], and Justin. D. Holmes[*1,2]
[1]University College Cork, Ireland
[2]Trinity College Dublin, Ireland
[4]Nexeon Limited, UK.

Nanostructured materials have received tremendous attention as potential Li-ion electrodes due to their unique size-dependent properties. In this review, we highlight a number of significant recent examples of nanostructured architectures as potential drivers of next-generation Li-ion batteries.

http://publish.ucc.ie/researchprofiles/D004/jholmes

Nano Research
DOI (automatically inserted by the publisher)
Review Article

Evaluating the performance of nanostructured materials as lithium-ion battery electrodes

Mark J. Armstrong[1], Colm O'Dwyer[2], William J. Macklin[4], and Justin. D. Holmes[1,3](✉)

[1]Materials Chemistry & Analysis Group, Department of Chemistry and the Tyndall National Institute, University College Cork, Cork, Ireland

[2]Applied Nanoscience Group, Department of Chemistry and the Tyndall National Institute, University College Cork, Cork, Ireland

[3]Centre for Research on Adaptive Nanostructures and Nanodevices (CRANN), Trinity College Dublin, Dublin 2, Ireland
[4]Nexeon Limited, Abingdon, Oxfordshire, UK.

Received: day month year / Revised: day month year / Accepted: day month year (automatically inserted by the publisher)

ABSTRACT

The performance of the lithium-ion cell is heavily dependent on the ability of the host electrodes to accommodate and release Li^+ ions from the local structure. While the choice of electrode materials may define parameters such as cell potential and capacity, the process of intercalation may be physically limited by the rate of solid-state Li^+ diffusion. Increased diffusion rates in lithium-ion electrodes may be achieved through a reduction in the diffusion path, accomplished by a scaling of the respective electrode dimensions. In addition, some electrodes may undergo large volume changes associated with charging and discharging, the strain of which, may be better accommodated through nanostructuring. Failure of the host to accommodate such volume changes may lead to pulverisation of the local structure and a rapid loss of capacity. In this review article, we seek to highlight a number of significant gains in the development of nanostructured lithium-ion battery architectures (both anode and cathode), as drivers of potential next-generation electrochemical energy storage devices.

KEYWORDS

Lithium ion batteries, nanostructuring, anodes, cathodes.

Introduction

Lithium-ion (Li-ion) batteries have been at the forefront of powering a host of modern consumer electronic devices since their commercial introduction in the early 1990s [1–5]. In more recent times, the requirement for alternative energy systems aiding a move away from our reliance on fossil-fuels, has seen Li-ion and other emerging technologies attract considerable attention to power an array of increasingly popular electric and hybrid-electric vehicle classes. Given the extreme popularity of Li-ion batteries, the research effort focused on improving their performance and design has been extensive. If Li-ion technology is to continue to flourish in the near future, of great importance are designs which offer both higher specific energy (W h kg^{-1}) and energy densities (W h L^{-1}). Current Li-ion batteries typically share three

Address correspondence to j.holmes@ucc.ie

common features: an anode, typically comprising a layered graphitic carbon, a cathode consisting of either $LiCoO_2$, $LiMn_2O_4$ or $LiFePO_4$, and an ionically conducting electrolyte which provides a means of transporting Li^+ to and from the component electrodes. Improvement in the design of one or more of these features may lead to Li-ion batteries with improved performance, delivering higher energy densities and characteristics such as increased capacity, charge/discharge rates and cycle lifetime. As the requirement for batteries powering ever-more demanding applications continues, such features have become increasingly important.

The role of nanostructuring

It is well known that scaling of material dimensions to that of the nanoscale may afford significantly altered material properties, which range from variances in charge and mass transport, to an increase in surface free energy arising through their high surface-to-volume ratios and increased robustness [6,7]. In terms of Li-ion battery chemistry, the solid-state diffusion of Li^+ ions in to and out of the component electrodes is fundamental to its operation; here, the diffusion of guest species (Li^+ in this instance), is commonly referred to as 'intercalation': By application of Fick's second law of diffusion within appropriate boundary conditions we obtain an approximate time constraint of species intercalation, as indicated in equation 1.01:

$$\tau = \frac{L^2}{D} \qquad (1.01)$$

where τ is the intercalation time, L is the diffusion length and D is the diffusion coefficient.

Thus, it is readily seen that the rate of intercalation is scaled respectively with the square of the diffusion length (L). Congruently, through nanostructuring we may facilitate an increase in the available rate of charge and discharge of the battery: Such rate increases have obvious implications on battery performance, offering the possibility of faster-charging batteries and batteries which are suitable for rate-demanding applications, such as is required for the emerging electric vehicle/hybrid electric vehicle (EV/HEV) classes. In addition to shortened diffusion lengths, Li^+ diffusion is also facilitated in nanoscale architectures through their high surface-to-volume ratios, which enables a high degree of electrolyte contact through the enhanced electrode–electrolyte interface, where Li^+ intercalation is entertained. The increased surface interactions may also result in enhanced solid–electrolyte interphase (SEI) layers, which allows passivation of the surface sites to the electrolyte solution, necessary for electrode stability. In addition, control of morphology through careful synthetic design, may also result in crystallographically tailored nanoarchitectures which are conducive to Li^+ transport mechanisms; such mechanisms may be difficult to attain in the bulk state. Of further benefit, the vast volume changes and associated strain effects which may result as a consequence of the (de)intercalation process (particularly expressed by alloying-type anodes), may be accommodated by the unique structural robustness afforded at the nanoscale. Given these host of benefits, numerous studies have demonstrated a marked improvement in the electrochemical performance of the nanostructured form versus the bulk counterpart.

While nanostructured electrodes may offer a range of improved performance features over existing bulk design, a consideration of any potential negative effects of their application must also be made. The first potential drawback is that an augmentation of unwarranted and poisonous side-reactions occurring at the electrode surface is possible, given the increased surface interactions expressed by nanoscale architectures; such instances may result in the formation of insulating and Li^+-impeding layers, which may severely influence the corresponding electrode operation. Secondly, any effects relating to the potential toxicity of nanoscale materials must be considered from a safety viewpoint, while in terms of

commercial viability, the complexity and increased production costs of their design must be heavily considered, where electrode preparation and associated costs are pivotal to potential industry application.

In this review article, we seek to highlight a number of significant recent examples of nanostructured Li-ion battery electrode architectures, both anode and cathode, which have been reported as potential drivers of next-generation electrochemical energy storage devices.

1 Recent developments in nanostructured anode architectures

One of the major focuses of Li-ion research over the last two decades has been in the development and discovery of novel anode architectures with enhanced Li-ion properties such as increased capacity, cycle life and rate performance, together with a consideration of production cost and environmental impact. Today's secondary Li-ion batteries commonly feature graphitic carbon as the anode material of choice, owing in part to its largely reversible Li^+ storage property, good electrical conductivity, stable SEI and ease of production. Graphitic carbon anodes, however, suffer from relatively low capacity (372 mA h g^{-1}) and sluggish rate performance. With the advent of the EV/HEV classes, future Li-ion batteries must meet the challenges of this emerging sector, necessitating a move to alternative materials with improved Li-ion capabilities [1,8,9]. A number of potential alternatives to carbon have emerged in recent times and is the focus of much research effort. The scope of this section is to familiarise the reader with some of the important recent advances which have been made towards anode architectures with improved characteristics for next-generation Li-ion batteries.

1.1 Silicon

Silicon anodes have been the focus of much research effort over a number of years owing to a number of important theoretical considerations [10]. Firstly, silicon forms a stable alloy with lithium of up to 4.4 Li^+ per formula unit Si, leading to a vast theoretical capacity of 4212 mA h g^{-1}, which is considerably higher than that of graphite (372 mA h g^{-1}). Secondly, Si anodes display long voltage plateaus at approx. 370 mV vs. Li/Li^+, thereby providing stable operating voltages when coupled with positive electrodes such as $LiCoO_2$ [10]. Lastly, Si is the second most abundant element in the Earth's crust and is thus considered a candidate for reasons of viable production cost and availability [11]. While Si anodes display potentially appealing Li-ion characteristics, it is important to note that Si suffers from two major drawbacks. The first is that Si suffers from structural changes induced on cycling, characterised by the formation of amorphous $Li_{15}Si_4$ and Li_ySi phases, leading to reduced cycling performance [12–14]. In addition, Si suffers from a large (± 400%), volume change during the (de)alloying process, the strain of which potentially leads to pulverisation of the local structure and electrical disconnect from the current collector; such an effect results in a marked loss of capacity and cycle performance [15]. Numerous examples in the literature have demonstrated the associated volume change on the local structure of the Si anode [16–18]. Nanostructured forms, however, may accommodate much of the strain associated with such alloying processes due to an increase in the surface to volume ratio associated with their reduced dimensions. One form of particular interest is the one-dimensional (1D) Si nanowire, which displays a high aspect ratio and has found numerous applications in semiconductor and other technologies [19]. Green et al. [20] were the first to propose using an arrangement of elongated silicon structures with sub-micron diameters on a substrate for the anode of a lithium-ion cell. In situ transmission electron microscopy (TEM) observations have revealed that the insertion of Li^+ into <112> oriented Si nanowires is associated with an anisotropic swelling of the nanowires, preferentially along the <110> direction, and characterised by a dumb-bell shaped cross-section [16]. The Li^+ diffusion–time study revealed deformation, resulting in fracture,

following a build-up of tensile stresses of the lithiated nanowires [16]. Such fracturing leads to poor cycle performance and thus requires an adequate understanding. The crystallographic orientation of the Si nanowire has been identified as one important aspect in governing the nature of anisotropic swelling [17,21]. Ab initio calculations revealed a preference for Li^+ diffusion in Si nanowires with a <110> growth direction [17], where Li^+ insertion occurs via layer-by-layer diffusion, originating from the surface of the nanowire (Li^+ interaction at surface sites is energetically favourable), through to the core of the nanowire with increasing energy [17]. Following Li^+ insertion, a core–shell structure develops consisting of crystalline Si and an amorphous Li_xSi shell, where an abrupt change in Li^+ concentration at the core–shell interface induces a chemical strain [21]; the amorphous shell relaxes by plastic flow [18], while the crystalline core suffers elastic deformation, potentially leading to fracturing of the local structure [21].

A number of 1D Si nanostructures (nanowires, nanotubes, etc.), have been demonstrated recently. Chan et al. [22], reported the preparation of arrays of Si nanowires grown directly on stainless steel substrates by an Au-seeded vapour–liquid–solid (VLS) mechanism. The synthetic procedure resulted in firm electrical contact with the current collector, while providing adequate strain relief, efficient 1D transport and a large electrode–electrolyte interface. Notably, utilisation of such arrays also negates the use of electrode binders or conductive additives, which may result in an increased energy density. The arrays of Si nanowires displayed a capacity of >2100 mA h g^{-1} at C rate (1 C = 4212 mA h g^{-1}, corresponding to a complete discharge in 1 h), and ~3500 mA h g^{-1} over 20 cycles at the C/5 rate, with no appreciable decline in capacity or apparent pulverisation of the nanowire structure [22]. Earlier studies of Si nanowires prepared by a VLS mechanism displayed stable cycling over 10–20 cycles [23]. Kang et al. [24], prepared single crystalline Si nanowires on stainless steel substrates by a chemical vapour deposition (CVD) method, which approached a near theoretical limit (4212 mA h g^{-1}) in the first discharge of ~4000 mA h g^{-1}. Despite displaying high Coulombic efficiency, the Si nanowires suffered from cyclic degradation resulting in a discharge capacity of ~1600 mA h g^{-1} after 50 cycles, representing a capacity loss of greater than 50% [24]. Capacity fading following structural transformation and increasing impedance may account for such losses [12,25]. Further examples of Si NW electrodes include those grown by reactive ion etching [20] or metal-assisted etching, which displayed both high surface roughness and high conductivity [26], and by a plasma-enhanced CVD method which displayed a high level of interconnection, maintaining good contact with the current collector with ~100% capacity retention at a C/2 rate [27].

A novel approach by Nexeon has been to form nanoscale Si pillar arrays on micron scale (2–25 μm) particle cores by metal assisted etching (Fig. 1), and where the resulting surface structured particles are then processed via a conventional slurry method with a binder and conductive additives to form a composite electrode coated on a copper foil substrate [28].

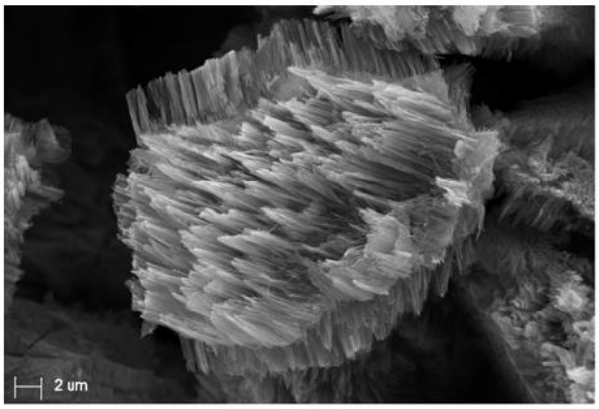

Figure 1 Pillared silicon particle produced by metal assisted etching. Reprinted with permission from ref. [28]. Copyright (2010) The Electrochemical Society.

The pillared particle composite electrodes in Li-ion cells with a $LiCoO_2$ cathode have demonstrated discharge capacities in the range 600 –1200 mA h g^{-1} associated with lithiation of the nanoscale Si pillars with cycle life performance of

up to 500 cycles (Fig. 2). Through optimisation of the pillar to core ratio within these pillared particle structures discharge capacities up to 2000 mA h g^{-1} are achievable based on full lithiation of the Si nanoscale pillars.

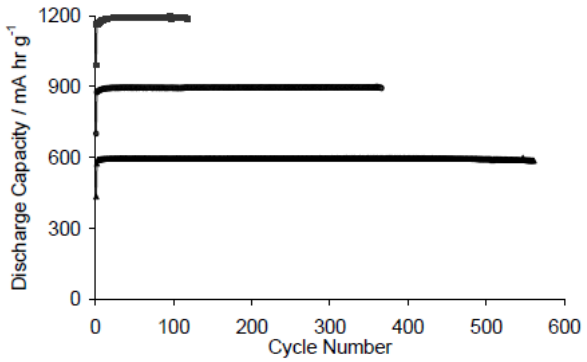

Figure 2 Cycle life performance of pillared silicon particle based composite anodes at various capacities. Reprinted with permission from ref. [28]. Copy right (2010) The Electrochemical Society.

The process of metal assisted etching on metallurgical grade silicon powders offers the prospect for low cost materials and is also readily scalable with pilot plant volumes already demonstrated. Furthermore, Nexeon has applied a similar process method of metal assisted chemical etching to much larger sized Si powders (up to 500 μm) in conjunction with the use of ultrasonic harvesting as an economic route for the production of Si fibres (nanowires), also for use as an anode material in Li-ion batteries (Fig. 3) [29]. The nanoscale dimensions of the resulting Si fibres results in a Si anode material where the full theoretical capacity of Si is accessible as reported with similar sized nanostructures produced via CVD or VLS growth methods.

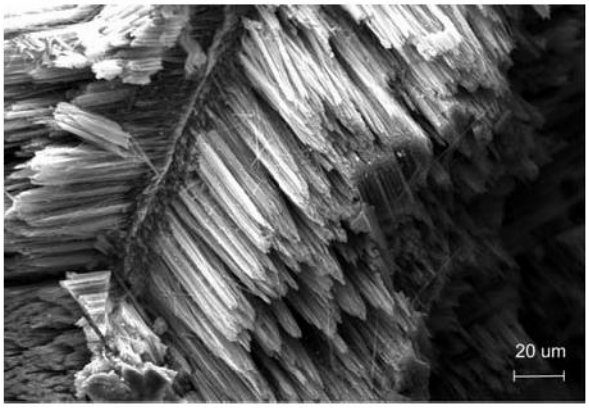

Figure 3 Si fibres produced by metal assisted chemical etching of large sized Si powders. Reprinted with permission from ref. [29]. Copy right (2010) The Electrochemical Society.

Composite Si nanowires having core–shell morphologies, or those with surface modification features, have also been proposed to enhance the cycling ability of Si nanowires, by further accommodating the strain associated with the alloying process. Carbon coated Si nanowire arrays [30,31], mesoporous Si/C nanowires [32], Si/carbon nanotube (CNT) composites [33], crystalline/amorphous core–shell nanowires [34], nanowires with polymeric coatings [35] and surface oxides [36], have thus shown improved cycling characteristics. The adoption of amorphous carbon coatings has been shown to facilitate volume expansion and further improve electrical conductivity within the nanowire array, resulting in improved cycling performance [30]. Porous, doped Si nanowires, etched from B-doped substrates have also shown appreciable performance with capacities of 1600 mA h g^{-1} reported after 250 cycles at C rate [37]. 1D Si nanotubes have shown promise as potential Li-ion anodes, whose unique morphology allows for ease of Li^+ transport through its large electrode/electrolyte interface. Volume expansion due to Li^+ insertion results in significant radial expansion (120%) as opposed to axial expansion (35%) [38,39]. As a result, the Si nanotubes are able to maintain their original morphology after several cycles while providing large capacities with relatively high retention (>85%) [43].

Two-dimensional (2D) Si nanostructures also

feature as potential candidates, although some moderation of capacity and cycle life has been experienced by pure Si nanoparticles [40]. Nest-like Si nanospheres, prepared by a solvothermal route, exhibited increased capacity, rate performance and capacity retention over their bulk Si counterparts [41], while hollow nanospheres prepared by Yao et al. [42], provided a high degree of particle interconnection, resulting in a stable cycling performance of up to 700 cycles. The stable cycle performance was attributed in part to a reduction in the available surface area of the nanospheres, thus limiting any potential inhibiting side-reactions with the electrolyte [42]. Further improvement in the anodic performance of Si nanoparticles has been displayed by composite formation [43–47], Si/CNT heterostructuring [48], or through porous arrangement [15,49–51]. The addition of alginate, a polysaccharide derived from brown algae, significantly enhanced the cycling performance of Si-based nanopowders, achieving a highly stable capacity of 1200 mA h g^{-1} after 1300 cycles (Fig. 4) [52]. Binder interactions may therefore significantly influence the performance of Si anodes [45] and as such, must possess qualities such as minimal interaction with the electrolyte, permeability to Li^+ and the ability to enhance the formation of a stable SEI layer [52].

Si–C nanocomposites prepared by a bottom-up approach also displayed enhanced anodic performance [44], where the internal porosity allowed for both rapid access of electrolyte and accommodation of volume induced stress, resulting in stable capacities of 1950 mA h g^{-1} following 100 cycles at C rate (Fig. 5).

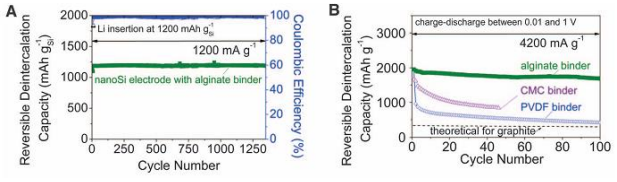

Figure 4 (A) Cycling performance of Si nanopowders enhanced by the addition of alginate binder and (B) cycling performance of the alginate binder electrodes vs. conventional sodium carboxymethylcellulose (Na-CMC) or polyvinylidene difluoride (PVDF) binders. From [52]. Reprinted with permission from AAAS.

The potential utilisation of Si as a Li-ion anode depends on the ability of the electrode structure to maintain structural robustness over successive cycling, while maintaining efficient electron transport through the structures to the current collector. Nanostructuring of Si electrodes is vital since bulk Si electrodes suffer from pulverisation over just a few cycles [11]. While capacity retention still remains for the most part somewhat problematic, Si displays significantly higher capacity and rate capability over today's conventional graphite anodes, even after hundreds of cycles.

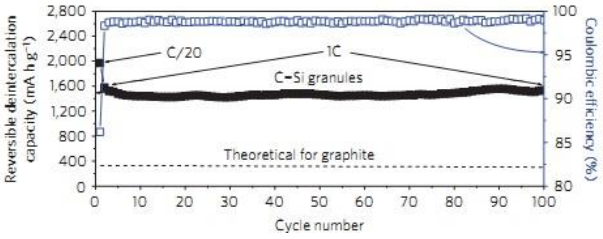

Figure 5 Cycling performance of Si–C nanocomposites prepared by a bottom-up approach. Reprinted by permission from Macmillan Publishers Ltd: Nature Materials [44] copyright (2010).

1.2 Germanium

Interest in Ge architectures stems from its ability to reversibly alloy with Li, thus forming Li_xGe ($0 \leqslant x \leqslant 4.4$) resulting in a theoretical capacity of ~1600 mA h g^{-1}. Much like its Si neighbour, Ge undergoes a large (± 370%) volume change on (de)alloying which may also lead to pulverisation of the local structure and a rapid decline in electrode performance [53]. In contrast, however, Li^+ diffusion in Ge is 400 times higher than in Si [54,55], while Ge also possesses higher (10^4) electrical conductivity, leading to the potential adoption of Ge in future high-rate Li-ion batteries. For example, Graetz et al. [54], demonstrated a rate capability of their Ge thin films to current rates as high as 1000 C.

High capacity Ge nanowires grown directly on stainless steel foils provided one of the first insights into Ge utilization as a Li-ion anode [53]. The sub-100 nm wires offered stable cycle performance

and remained structurally intact after successive cycling. In situ TEM analysis has since provided a further understanding of the structural changes which evolve during lithiation and delithiation of Ge nanowires [56]. The microscopy study revealed a two-stage transformation process, beginning with the formation of an amorphous Li_xGe phase, and followed by the formation of crystalline $Li_{15}Ge_4$. The resultant stress was partially alleviated through the formation of nanopores during delithiation (Fig. 6), outlining the structural robustness of the Ge nanowires [56]. Recently, Ge/C nanocomposites revealed a large performance increase over their pure Ge nanowire counterparts, suggesting a carbon buffer matrix may also be beneficial in restricting much of the volume-induced strain [57,58].

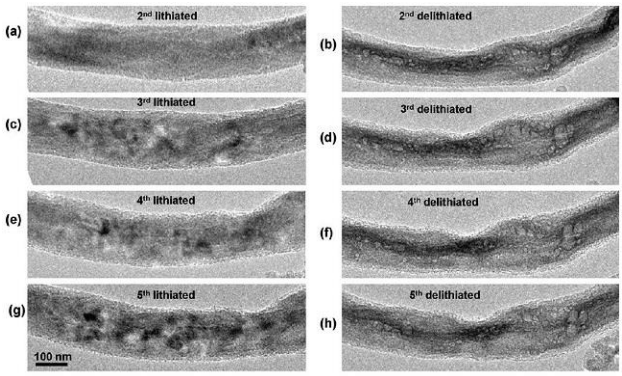

Figure 6 Reversible nanopore formation during lithiation-delithiation cycles of VLS-grown Ge nanowires. Adapted with permission from [56]. Copyright 2011 American Chemical Society .

Ge nanowires, however, invariably possess a non-uniform and unstable surface oxide, GeO_x, which is ultimately poisonous to both electronic and battery application. The surface oxide readily reacts with Li^+ to form Li_2O, thus detrimentally affecting electrode performance. Ge nanowires grown by a Sn-assisted CVD mechanism displayed a Coulombic efficiency of just ~50% in the first cycle, which was attributed in part to the existence of the GeO_x sheath [59]. Restricting the size of GeO_x layer is therefore crucial to the utilisation of Ge in future battery designs. Treatments may include etching GeO_x with HF, followed by the addition of protective organic layers, which was shown to prevent surface re-oxidation [60]. Ge nanowires surrounded by an amorphous carbon sheath offered high capacity and Coulombic efficiencies exceeding 90%, even at a high C-rate [61]. Carbon coating is suggested as a means to restrict surface re-oxidation, in addition to providing a buffer matrix for the volumetric changes induced on alloying. Other 1D nanostructures displaying enhanced anodic performance include Ge/CNT composites [62,63], dual-layer Si/Ge nanotube arrays [64] and solution-grown Ge nanotubes prepared from Ge–Sn nanowires [65]. The Ge nanotubes displayed high charge capacities (965 mA h g^{-1} at C/2 rate) and good rate performance, owing to their unique morphology [65], while Si/Ge nanotube arrays displayed excellent cycling characteristics as a result of minimal hoop strain [64].

Other candidates of note include porous Ge nanostructures [66–68] and GeO_x hierarchical structures [69], which have displayed enhanced performance owing to their porous structuring. The 3D porous nanoparticles prepared by Park et al. (Fig. 7) [66], displayed excellent capacity retention and structural stability over 100 cycles at C rate, compared to their non-porous, 0D counterparts. The zero-dimensional (0D) Ge nanoparticles did not sustain their structure on alloying, resulting in marked loss of capacity over successive cycles.

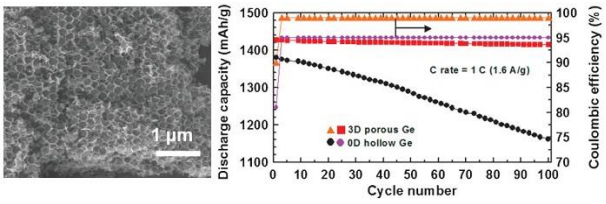

Figure 7 Porous 3D Ge nanoparticles and their performance as Li-ion anode (C-rate). Adapted from Ref. [66]. Copyright Wiley-VCH Verlag GmbH & Co. KGaA. Reproduced with permission.

Although efforts have shown Ge to be a promising candidate for future Li-ion cells, further work is envisioned for this material candidate in

order to fully realise its potential. Much like Si, Ge candidates must sustain the structural changes which evolve as a result of alloying, while methods such as organic functionalisation may be utilised to limit the influence of GeO_x layers and thus, improve its performance.

1.3 Tin

A third metal which reversibly alloys with lithium is tin (Li_xSn, $0 \leqslant x \leqslant 4.4$), and has therefore garnered considerable interest as a result of its theoretical capacity of 993 mA h g^{-1} [70–72]. The Li–Sn alloying process again results in considerable volume change (up to 300%) which, unless accommodated, results in rapid degradation in electrode performance. Relatively few recent studies have reported the synthesis of pure Sn architectures [73], and rather more commonly obtained is SnO_2, which irreversibly reacts with Li^+ to form Sn ($SnO_2 + 4Li^+ + 4e^- \rightarrow Sn + 2Li_2O$). The conversion of SnO_2 to pure Sn architectures results in significant capacity loss in the first cycle, which may subsequently stabilise as a result of a reversible alloying process.

In situ TEM analysis of the charging process on a single SnO_2 nanowire [74], revealed that volume expansion was accommodated through a 90% elongation in the axial direction, as opposed to 35% radially (Fig. 8). The formation of Li_xSn and Li_2O was responsible for the 250% total volume increase, while the resultant strain resulted in a significant twisting and bending of the nanowire. A Li^+-driven reaction front propagated along the nanowire length, resulting in a high-density dislocation zone separating crystalline SnO_2 from amorphous Li_xSn [74]. The de-alloying process, resulting in the formation of metallic Sn, was observed on discharge. Self-supported SnO_2 nanowires [75] and hybrid Sn/SnO_2 nanowires [76] have demonstrated high capacity and stable cycling as a result, and are determined to be important classes of Sn-based electrodes [77]. Other examples of 1D nanostructures include nanorod arrays which were grown hydrothermally on flexible substrates and displayed significantly increased cycling performance compared to 0D structures [78].

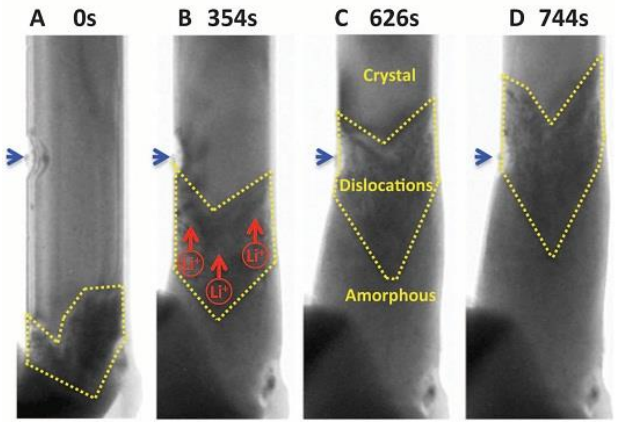

Figure 8 In-situ TEM observations of the Li^+-driven transformation of SnO_2 nanowires on charging. Dislocations result as a consequence of a Li^+ driven transformation of crystalline SnO_2 to an amorphous Li_xSn phase. From [74]. Adapted with permission from AAAS.

Sn/C or SnO_2/C composites have perhaps received the most attention, due to the volumetric buffering and electrical qualities of carbon. Carbon coated SnO_2 particles offer an insight into the effectiveness of the carbon additive, displaying enhanced cycling characteristics [79–84], while Sn/C composites have shown high performance with stable capacities reported over hundreds of cycles [85], and considerable performance increase over bulk Sn [86]. Carbon-coated Sn particles encapsulated in hollow nanofibres, for example, displayed high capacity with minimal capacity fade (Fig. 9), outlining the practical importance of the carbon additive [87].

Sn/graphene nanocomposites have also shown promising results compared to their pure Sn counterparts [88–91]. Graphene composites may offer increased surface area, higher electronic conductivity and greater mechanical strength, necessary for enhanced electrochemical performance [92]. Porous structuring may also alleviate some of the strain associated with the alloying process, while providing an increased electrode/electrolyte interface; such structures have

thus shown improved Li-ion performance [93–95]. Detrimentally, however, porosity may lead to eventual trapping of Li^+ ions during electrochemical operation, which leads to irreversible capacity fading [77]. Other notable nanostructured examples include solution-grown SnO_2 nanoflowers [96], and hydrothermally prepared hollow SnO_2 structures, both of which showed enhanced anodic performance [97].

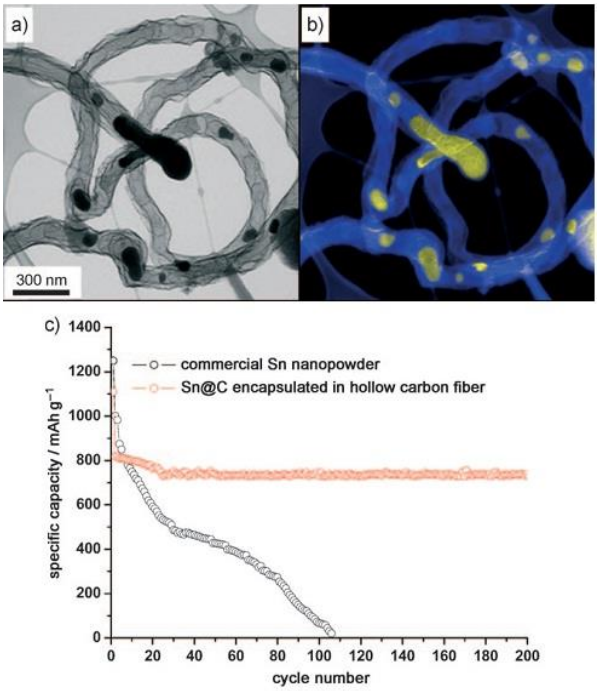

Figure 9 (a) TEM image of Sn/C particles encapsulated in hollow nanofibres and (b) elemental mapping showing C (blue) and Sn (yellow) and (c) capacity *vs.* cycle number outlining the role of the carbon-buffer in cycle performance. Adapted from [87]. Copyright Wiley-VCH Verlag GmbH & Co. KGaA. Reproduced with permission.

Recently, Sony has commercialised its Nexelion® range of Li-ion cells containing Sn–Co–C anodes. Such alloys have shown excellent cycling abilities attributed to the active–inactive relationship between Sn and Co [98–101]. Other alloys include Sn–Ni–C [102] and Sn–Cu [103] which also utilise the inactive metal and carbon as a structural buffer, thus alleviating much of the alloyed-induced strain. The commercial utilisation of Sn has demonstrated its purposeful character as a Li-ion anode, however, next-generation batteries may ultimately adopt materials with greater capacity and higher rate capability.

1.4 $Li_4Ti_5O_{12}$ (LTO)

Li-alloying compounds offer significantly higher capacities versus their intercalation rivals due to a high accommodation of up to 4.4 Li^+ per unit metal. However, the associated volume change must be accommodated if they are to be viable candidates in next generation Li-ion batteries. At present, graphite is the most common intercalation anode material owing to its relatively high capacity (372 mA h g^{-1}), high Li^+ reversibility, sound electrical conductivity and ease of production. Another important member of the intercalation family, spinel-phase $Li_4Ti_5O_{12}$ (LTO), has been proposed as a future Li-ion anode due to a number of practical considerations. The first is that LTO experiences a near zero-strain (0.2%) on intercalation, resulting in a high degree of structural integrity during electrochemical cycling [104]. Secondly, LTO displays a flat discharge profile at ~1.5 V vs. Li/Li^+, which is higher than the reduction potential of most associated electrolyte solvents. As a result of its high operating voltage, LTO experiences no surface passivation due to the reduction of carbonate solvents, or the formation of dendritic lithium, which leads to long cycle-life and improved safety [104]. In addition, LTO cells have demonstrated safety at ultra-high charge potentials, resulting in minimal thermal runaway [105]. LTO can accommodate up to 3 Li^+ per formula unit, resulting in an end-phase of $Li_7Ti_5O_{12}$ [106], with a theoretical capacity of 175 mA h g^{-1}. While such capacity is lower than graphite, intercalation rates are fast and further enhanced through nanostructuring, leading to the potential application of LTO in future high-rate Li-ion batteries [105]. While LTO displays such desirable Li-ion characteristics, it suffers from poor electronic conductivity. Poor conductivity is detrimental to the performance of a high-rate Li-ion anode where efficient electron transport is paramount. Typically, carbon coatings [107–113], carbon [114,115] or graphene nanocomposites

[116,117], dopants [118–121] or surface modifiers [122,123], may be introduced to increase electrical conductivity. Surface modification is an effective means to shorten electronic pathways and alternatives to carbon layers are increasingly attractive [122]. To this end, solution-prepared LTO nanosheets, modified with edge-terminating rutile-TiO_2, displayed both enhanced rate capability and cycle performance (Fig. 10).

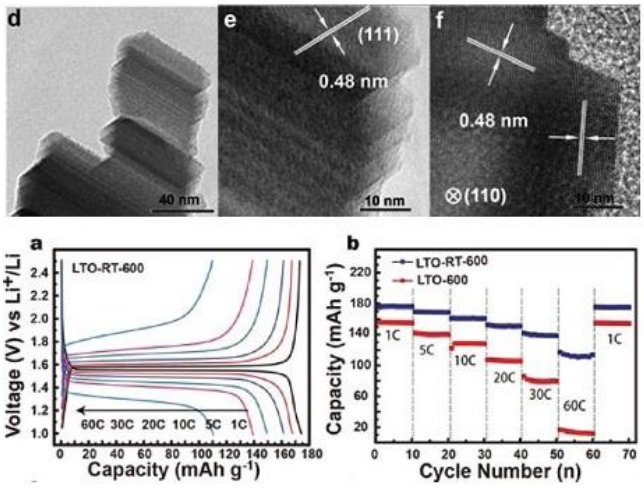

Figure 10 TEM images of TiO_2-modified LTO nanosheets (d-f) and their respective Li^+ storage properties over current rates between 1–60 C (a, b). Adapted with permission from [122]. Copyright 2012 American Chemical Society.

Additive-free LTO anodes have also shown enhanced performance, which has been ascribed to an increase in electrical conductivity of lithiated $Li_{4+x}Ti_5O_{12}$ phases formed as a result of discharge [124]. Porous [125–128] and hollow sphere [129,130] morphologies of LTO have displayed also superior performance as a result of their unique nanostructured form. Mesoporous thin-film electrodes have displayed electrical conductivity close to that of bulk LTO, resulting in appreciable performance [125]. When combined with a suitable cathode, such as lithium nickel manganese oxide (LNMO) $Li[Ni_{0.45}Co_{0.1}Mn_{1.45}]$, LTO cells display exceptional performance over hundreds of cycles at C-rate, even at rates as high as 10 C (Fig. 11) [131]. The full cells also exhibited stable cycling performance over a wide range of temperatures (from –20 to 55 °C, Fig. 12). A reported energy density of 260 W h kg^{-1} is also higher than any of today's commercial cells, highlighting the commercial viability of LTO electrodes.

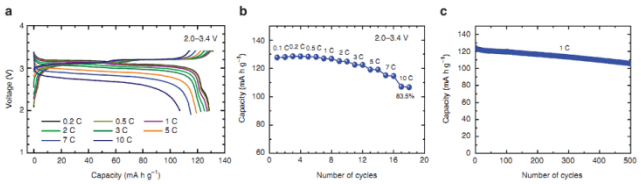

Figure 11 (a) Voltage profiles of the LTO/LNMO cells at various rates between 2.0 – 3.4 V vs. Li/Li^+, (b) total discharge capacity obtained with increasing rate and (c) cycling performance of a LTO/LNMO cell at C rate over 500 cycles. Reprinted by permission from Macmillan Publishers Ltd: Nature Communications, [131] copyright (2011).

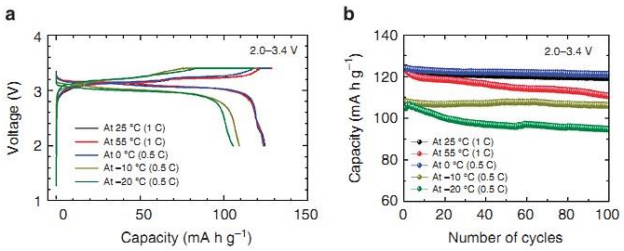

Figure 12 (a) Voltage profiles of LTO/LNMO cells between -20 – 55 °C and (b) cycling performance outlining the stable capacity over the same temperature range. Reprinted by permission from Macmillan Publishers Ltd: Nature Communications, [131] copyright (2011).

LTO electrodes have shown remarkable cycling ability and rate performance over a wide range of temperatures, while their operating voltage offers increased safety over other suggested anodes, which is of particular concern to the EV/HEV market. To its detriment, however, LTO suffers from relatively low capacity and poor electronic conductivity, which could potentially limit its application in future Li-ion batteries.

1.5 Carbon

Carbon in the form of three-dimensional (3D) graphite is the most common source of anode material in today's commercial cells. Graphite has a theoretical capacity of 372 mA h g^{-1} and intercalates

Li^+ to an end-phase of LiC_6. While graphite possesses useful qualities such as sound electrical conductivity and high Li^+ reversibility, it is lacking in total gravimetric capacity which leads to cells with potentially lower energy density. Alternative carbon architectures may boost Li^+ storage capacity as a result of a greater number of available Li^+ insertion sites. Examples of 1D carbons which have attracted attention include single-walled and multi-walled carbon nanotubes (S/MWCNTs), [132–140] carbon nanofibres [141,142] and carbon nanofibre/nanotube composites [143]. Carbon nanotubes (CNTs), consist of 2D graphene sheets rolled into single or multiple layers, which display enhanced properties such as rapid electronic conductivity and increased capacity as a result of their unique structuring. CNTs may be grown in paper-like form [135,137], or more conveniently, in free-standing form grown directly on conducting current collectors or glassy carbon [133,138]. MWCNTs grown in this fashion have displayed highly reversible cycle behaviour resulting in a capacity of 575 mA h g^{-1} after 100 cycles at a current density of 0.2 mA cm^{-2} (Fig. 13) [133]. Despite displaying long cycle-life, MWCNTs grown on stainless steel substrates suffer from pulverisation of their structure and surface defects, as a result of continued electrochemical cycling [138].

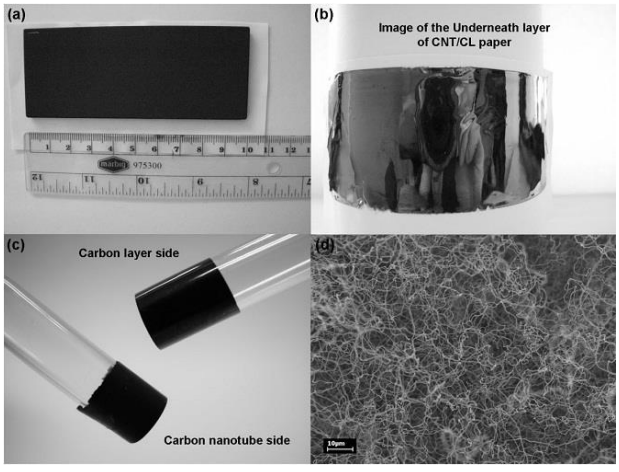

Figure 13 (a)–(c) Digital photographs of MWCNTs grown on glassy carbon layers and (d) a SEM image of the MWCNTs. Adapted from Ref. [133]. Copyright Wiley-VCH Verlag GmbH & Co. KGaA. Reproduced with permission.

A comparison of MWCNTs versus their single-walled and double-walled counterparts reveals that MWCNTs are the choice anode material due to fewer irreversible losses on cycling [135]. In addition, cyclic voltammetry studies have shown only MWCNTs behave in a similar fashion to graphitic carbon, where the surface chemistry of MWCNTs is less dominant compared to single and double-walled carbon nanotubes [135]. The intercalation chemistry of CNTs is therefore highly dependent on both their internal and external structuring, where a number of defects or surface functionalities may influence properties. Indeed, this may be illustrated when considering shorter CNTs, which have displayed enhanced performance over longer CNTs as a result of an increasing number of structural (lateral) defects [139,144]. In this case, increasing the density of graphitic edges in the MWCNT results in a greater capacity, while structurally shortening may result in fewer instances of Li^+ trapping and thus, fewer irreversible losses [139,144]. An improved rate capability was also displayed as a result of lower electrical resistance [139]. Combining MWCNTs with high surface-area mesoporous carbon has also facilitated enhanced performance due to a synergistic relationship between the high electrical conductivity of the MWCNTs and the favourable Li^+ transport properties of mesoporous carbons [141].

In demonstrating the useful properties of the MWCNT as a potential electrode scaffold, tailoring the surface functionality of MWCNTs resulted in Li-ion cells (full cells), which are stable over thousands of cycles and which display extremely high power densities (~100 kW kg^{-1}) [136]. The increased electrochemical response is attributed to reversible Faradaic interactions of Li^+ with surface oxygen, originating from the carboxylic acid (–COOH) functionalised surface. Confirmation of the role of surface oxygen was sought by reducing the functionalised MWCNTs in flowing H_2/Ar, which resulted in a 40% reduction in gravimetric capacity. Further, the charged surface resulted in

MWCNTs with an exceptional rate capability, where approximately 50% of the total gravimetric capacity could be delivered at a current density as high as 180 A g^{-1} (in this case, one complete discharge per ~2 s) [136]. Specifically tailored MWCNTs may therefore find potential use as positive electrodes in future high-rate, high-power Li-ion batteries.

Graphene, the building block of the 1D CNTs, exists as a 2D layer of sp^2-hybridised carbon one atom thick, and continues to attract considerable attention owing to its vast surface area (>2500 m^2 g^{-1}), fast electron mobility and excellent electrical conductivity [145–148]. Li^+ diffusion in graphene is heavily influenced by edge effects [149,150] where the relative strength of Li^+ interaction (adsorption and diffusion) varies according to the morphology of the edge [149]. Such edges, along with other structural defects, offer reversible Li^+ storage sites and are thus responsible for additional capacities [151,152]. Graphene nanoribbons (GNRs), a quasi-1D nanostructure offering similar electrical properties to that of SWCNTs, were studied as a potential Li-ion anode having been previously identified as a potential candidate based on its edge storing capabilities [149,153]. The GNRs were prepared by unzipping MWCNTs by a solution-based oxidation process, resulting in oxygen-rich GNRs; the GNRs were subsequently reduced under a flow of H_2/Ar. The resulting electrodes displayed increased capacity versus pristine MWCNTs with a rate of loss of 2.6%, however, the GNRs displayed considerably lower capacity versus the pre-formed oxygen-rich GNRs, which achieved a discharge capacity of 820 mA h g^{-1} versus ~290 mA h g^{-1} for the GNRs in the first cycle [153]. The oxygen-rich GNRs displayed the highest rate of loss, however, (~3% per cycle), while the increased capacity was suggested to be the result of a more-stable, chemically bonded SEI layer.

Disordered graphene nanosheets (stacks of 2D graphene), have also displayed high reversible capacities (up to ~1000 mA h g^{-1}) as a result of increasing defect densities [151,154]. The additional Li^+ storage sites therefore contribute to a more than two-fold increase in total gravimetric capacity, compared to 3D graphite. Although surface functionality has been shown to dramatically improve the electrochemical performance of MWCNTs, electrochemical testing of graphene oxide (GO) nanosheets revealed surface functionality (–O and –H terminated) did not contribute to additional capacity while in fact, the GO nanosheets were found to offer lower capacity compared to their reduced counterparts [151]. In addition to utilising structural disorder, further capacity has been obtained by the addition of carbon additives such as CNTs or fullerenes to graphene nanosheets. Such additions are shown to actively increase the inter-graphene (001) layer separation from 3.6 Å to a maximum of 4.0 Å [155]. Increasing the inter-layer spacing may result in additional Li^+ storage sites and ease of Li^+ transport, although a definitive Li^+ storage mechanism has not been proposed. The gravimetric capacity increased from 540 to 730 mA h g^{-1} for CNT addition and to 784 mA h g^{-1} for fullerene addition (at a current density of 50 mA g^{-1}), indicating the largest capacity increase is seen with the largest inter-layer separation. These results offer over twice the capacity of conventional graphite, while remaining appreciably stable. Similarly, graphene paper electrodes have also displayed increased layer separation (up to 3.79 Å) as a result of surface functionality [156], while offering properties such as high tensile strength and high electrical conductivity, while remaining suitably binder-free [156,157]. Although the capacity of such paper electrodes was shown to be lower than conventional graphite, a recent 3D configuration has shown improved Li-ion performance [158]. The 3D configuration, which was obtained by mechanically pressing a graphite oxide aerogel, displayed excellent capacity retention to as many as 5000 cycles, while offering a much improved rate performance over previous reports of graphene paper electrodes. The increased performance was attributed to the unique folded-structure of a few layers of graphene and the ease with which the electrolyte could penetrate the 3D structure [158]. Although our understanding of graphene is in a relatively infant stage, its unique electrical and

mechanical properties, together with further research, may make it an appealing candidate for future Li-ion batteries.

Other forms of nanostructured carbon materials that deserve mention include 2D carbon spheres [159] and 3D hollow carbon nanocages [160,161]. In particular, carbon nanocages (CNCs) with a nanographene shell have shown stable cycling performance with increasing graphitisation [160]. The CNCs, prepared by a supercritical fluid (SCF) method, offer capacities approaching 600 mA h g^{-1} and high rate performance as a result of their unique structuring (Fig. 14). The nanographene shell results in high inter-particle conductivity and additional Li^+ storage sites, while their hollow, porous structure, offers ease of electrolyte access, facile Li^+ transport and accommodation of Li^+ induced volume changes [160].

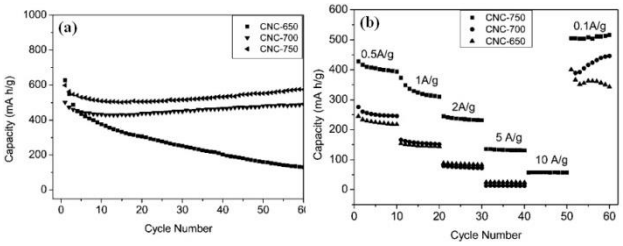

Figure 14 (a) Cycling performance of CNCs. Increasing temperature results in higher graphitisation and improved cycling and (b) rate performance of the CNCs at current densities ranging from 0.1–10 A g^{-1} [160]. Adapted with permission of The Royal Society of Chemistry.

1.6 Transition metal oxides

Transition metal oxides (TMOs), offer a third type of Li-ion anode architecture through an electrochemically-induced conversion reaction adopting the following, generalised form (equation 1.02) [71, 162]:

$$\text{nano-TMO} + 2Li^+ + 2e^- \leftrightarrow \text{nano-TM} + Li_2O \quad (1.02)$$

The formation of metallic nanoparticles during discharge is thermodynamically favourable and is associated with multi-electron transfer, while the electrochemical decomposition of Li_2O is ostensibly realised through the unique synergy that exists between the nanosized metallic domains and the characteristically inert Li_2O matrix [162]. The seemingly unfavourable reverse reaction is therefore only achievable through nanostructuring and may lead to sluggish Li^+ diffusion and rate capability. Although the associated multi-electron transfer allows for capacities in excess of conventional intercalation anodes, capacity fade as a result of structural degradation and volume change may still present a challenge. Nanostructuring may therefore not only enable successful conversion chemistry, but may also accommodate many of the structural strains induced as a result of electrochemical cycling.

1.6.1 Iron oxides

Iron oxides (Fe_2O_3, Fe_3O_4 etc.), represent a popular class of transition metal oxides and find use in numerous applications such as diagnostic imaging and other biomedical applications [163]. Large particles (~0.5 μm) of the most stable iron oxide, α-Fe_2O_3 (hematite), have previously demonstrated a large size-dependent effect on reaction with Li^+ [164], where a structural transformation occurs from the cubic to hexagonal system after insertion of an equivalent of just 0.05 mol. Li^+ [165]. Nanosized (~20 nm) Fe_2O_3 particles, however, maintained their structural integrity (corundum phase), to an equivalent of 1 mol Li^+ per Fe_2O_3 before conversion, contributing to a final capacity of 1400 mA h g^{-1} in the first discharge cycle [165]. Although early work on Fe_2O_3 anodes resulted in high initial capacities, much of the capacity was lost with extended cycling. More recently, advanced Fe_2O_3 structures such as nanoflakes [166], nanocapsules [167], nanodiscs [168], hollow nanoparticles [169], nanotubes [170], and reduced-graphene/Fe_2O_3 nanocomposites [171] have emerged with enhanced Li-ion performance. Liu et al. [170], prepared 1D α-Fe_2O_3 and C–Fe_2O_3 nanotubes grown directly on conducting substrates by a so-called "sacrificial template-accelerated hydrolysis" (STAH) method, using arrays of ZnO nanowires as hard templates. The H^+ generated due to hydrolysis of the Fe^{3+} precursor, resulted in

dissolution of the ZnO nanowire template which in turn, facilitated the hydrolysis of the Fe^{3+} precursor (Fig. 15). The addition of glucose to the Fe^{3+} precursor sol resulted in the formation of C/Fe_2O_3 nanotubes, with a layer of carbon approximately 1.5 nm thick. The resulting α-Fe_2O_3 nanotubes delivered adequate performance reaching a capacity of ~375 mA h g^{-1} after 150 cycles (C/5 rate), while the C/Fe_2O_3 nanotubes displayed a much higher capacity and excellent cycling characteristics, delivering a final capacity of 659 mA h g^{-1} after 150 cycles at the same rate. An initial intercalation mechanism was suggested which accounted for initial capacity gains and was associated with a transformation from cubic Fe_2O_3 to hexagonal $Li_2Fe_2O_3$ before conversion at 0.8 V (identifiable by a long plateau region in the discharge profile), resulting in the formation of Fe^0 and Li_2O species. The addition of carbon was suggested to offer structural support by means of a buffering effect while the improved electrical conductivity of the C/Fe_2O_3 nanotubes enabled the enhanced rate performance (up to 12C) that was reported [170].

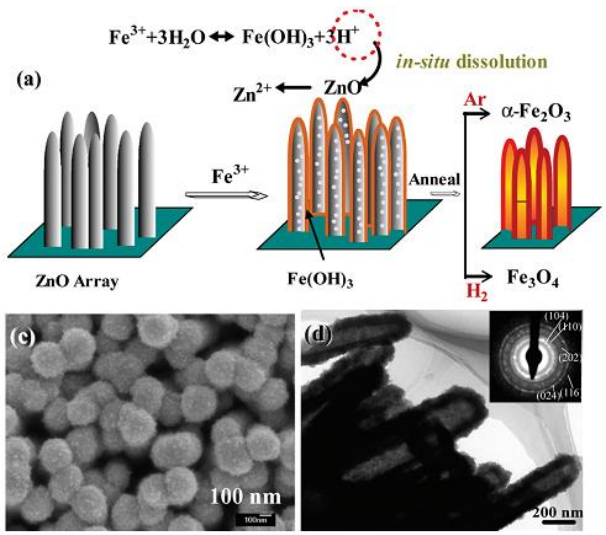

Figure 15 (a) Schematic of the STAH method used to produce α-Fe_2O_3/Fe_3O_4 nanotubes. The addition of glucose to the precursor sol resulted in C/Fe_2O_3. (c) SEM image and (d) TEM image of the resultant arrays of α-Fe_2O_3 nanotubes. Adapted with permission from [170]. Copyright 2010 American Chemical Society.

Similar performance has been demonstrated with porous α-Fe_2O_3 nanodiscs prepared by oxalic acid etching of single crystal Fe_2O_3 nanocrystals [168]. Preferential etching in the <001> direction was carried out using phosphate ($H_2PO_4^-$) as a biased capping agent. The phosphate anions, which selectively bind to lateral (110) planes of the Fe_2O_3 structure, coordinate the oxalic acid etching process from the exposed ends, ultimately yielding a 2D nanodisc structure. Rod-like structures could also be synthesised when starting with highly anisotropic α-Fe_2O_3 spindles (Fig. 16). Controlling the etching time and starting material resulted in nanodiscs with tunable porosities, offering improved electrochemical performance due to the accommodation of volume change stresses and increased surface area. The porous α-Fe_2O_3 nanodiscs displayed a large discharge capacity of 662 mA h g^{-1} after 100 cycles at a rate of C/5. Such examples outline the impact of structural modification on the electrochemical performance of Li-ion anodes.

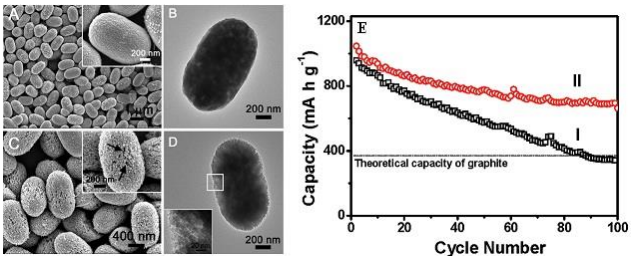

Figure 16 (A, B) SEM and TEM images of α-Fe_2O_3 nanodiscs (type I) and (C, D) type II α-Fe_2O_3 nanodiscs and (E) discharge capacity as a function of cycle number for type I and type II nanodisc samples. Adapted with permission from [168]. Copyright 2010 American Chemical Society.

Hollow α-Fe_2O_3 nanocapsules [167], reduced-graphene/Fe_2O_3 nanocomposites [171] and γ-Fe_2O_3 nanoparticles [169] in particular, have also shown high capacities in the anodic region (0.01–3 V). Hematite nanocapsules, prepared by coating spindle-like β-FeCOOH with SiO_2 followed by the thermal treatment and wet-chemical etching of the SiO_2 shell, displayed capacities as high as 888 mA h g^{-1} after 30 cycles [167]. In contrast, hollow γ-Fe_2O_3

nanoparticles, annealed between two layers of MWCNTs at 200 °C, exhibited initial capacities in excess of 1000 mA h g^{-1} [169]. The high capacity of the hollow γ-Fe_2O_3 nanoparticles was attributed to Fe cation vacancies in the host γ-Fe_2O_3 structure which could act as additional Li^+ storage sites at higher voltages, while the hollow morphology enabled rapid Li^+ transport and structural support during the electrochemically-induced phase transitions. Solid γ-Fe_2O_3 nanoparticles fared considerably worse and this delineates the effect of γ-Fe_2O_3 particle morphology on its electrochemical performance. Although extensive cycling data for the conversion of hollow γ-Fe_2O_3 nanoparticles was not reported, the work outlines the importance of structural tailoring to enhance Li-ion capacity.

Fe_3O_4 (magnetite) electrodes have also been extensively researched as potential Li-ion anodes, some reports of which are outlined in Table 1. Magnetite displays similar electrochemical properties to hematite, with a theoretical capacity of 920 mA h g^{-1} obtainable after an $8e^-$ conversion reaction (equation 1.03). Due to the poor capacity retention of pure Fe_3O_4 electrodes and their poor electronic conductivity, the addition of carbon or graphene to Fe_3O_4 electrodes has been reported in many studies (Table 1). Stable capacities in excess of 900 mA h g^{-1} have been reported.

$$Fe_3O_4 + 8Li^+ + 8e^- \leftrightarrow 3Fe^0 + 4Li_2O \quad (1.03)$$

Table 1 Some reported Fe_3O_4 nanostructures with their respective capacities (mA h g^{-1}). The rate and cycle number is given in brackets.

Composition	Morphology	Initial Capacity	Final Capacity	Ref
Fe_3O_4/C	Nanospheres	1166 (C/5)	712 (60)	[172]
Fe_3O_4/C	Nanospindles	749 (C/2)	600 (80)	[173]
Fe_3O_4/C	Nanowires	~800 (C/10)	~800 (50)	[174]
Fe_3O_4/C	Nanocrystals	~610 (C/10)	~635 (50)	[175]
Fe_3O_4/C	Nanofibres	1551 (C/5)	1007 (80)	[176]
Fe_3O_4/C	Spheres	1259 (C/5)	984 (70)	[177]
Fe_3O_4/graphene	Nanoparticles	~1320 (C/10)	~900 (50)	[178]
Fe_3O_4/graphene	Particles/sheets	~1450(C/20)	1026 (30)	[179]
Fe_3O_4/graphene	Nanoparticles	~1080 (C/10)	650 (100)	[180]
Fe_3O_4/graphene	Particles/sheets	~1450 (C/10)	1045(40)	[181]
Fe_3O_4/graphene	Particles/sheets	1637 (~C/10)	1112(5)	[182]
Fe_3O_4/graphene	Particles/sheets	1114 (C/10)	605 (50)	[183]
Fe_3O_4/rGO	Particles/sheets	1066 (C/5)	531 (50)	[184]
Fe_3O_4/C/rGO	Particles/sheets	1426 (C/5)	543 (100)	[185]

Fe_3O_4/SWNT	Rods/tubes	1080 (C/10)	1100 (C, 50)	[186]
Fe_3O_4	Spheres	1322 (C/10)	890 (60)	[187]

1.6.2 Cobalt oxides

Cobalt oxides (CoO, Co_2O_3, Co_3O_4), are another important class of 3d-metal oxides. Among them, Co_3O_4 is perhaps the most suitable candidate for Li-ion batteries and has a theoretical capacity following a complete conversion reaction ($8e^-$) of 892 mA h g^{-1}. The recovered species on charging of Co_3O_4 has been identified as CoO, resulting in a reversible $6e^-$ conversion reaction facilitating capacities approaching 670 mA h g^{-1}. As with Fe_3O_4 and other Li anodes, control of composition, particle size and morphology have been identified as important aspects affecting the electrochemical performance of Co_3O_4 anodes.

Despite earlier reports of poor capacity retention among Co_3O_4 nanowires [188], recent examples have displayed excellent Li-ion capabilities, including significant rate performance [189,190]. Initially, the poor capacity retention of the Co_3O_4 nanowires was attributed to inter-particle disconnect following complete conversion, resulting in Co nanograins electrically isolated from one-another by insulating polymeric layers [188]. Li et al. [189], prepared mesoporous Co_3O_4 nanowires having mean diameters of approx. 500 nm and a pore size of 3.3 nm, by a mild, template-free ammonia evaporation method, which could be extended to grow nanowires on a range of different substrates (Si, Ti, Cu, glass, plastic etc.), and over wide areas (up to several centimeters in length). The Co_3O_4 nanowires displayed capacities as high as 700 mA h g^{-1} after 20 cycles at C-rate (approx. 78% of the theoretical maximum), and showed significantly enhanced performance compared to powder and broken, non-supported nanowire samples. In this case, the Co nanograins formed on discharge were suggested to remain interconnected throughout the insulating Li_2O matrix, thus forming a conductive network where electron transfer may propagate through the nanowire from root to tip. Such interconnection would facilitate efficient electron transfer and its incidence is supported by the high-rate capability displayed by the Co_3O_4 nanowires (cycling at rates of 20 C and 50 C resulted in discharge capacities of 450 and 240 mA h g^{-1}, respectively) [189]. The markedly improved performance of the Co_3O_4 nanowires revealed the importance of maintaining structural integrity during electrochemical cycling. While earlier work had additionally identified an insignificant role of porosity on the electrochemical performance of Co_3O_4 particles [188], porous Co_3O_4 nanowires prepared by hydrothermal synthesis using nitrilotriacetic acid (NTA) as a structure-directing ligand, also displayed a high capacity (up to 1366 mA h g^{-1} in the first discharge cycle), and appreciable cycling ability [190]. The porosity of Co_3O_4 nanowire samples has been suggested to aid the structural integrity of the material by accommodating much of the volume strain associated with the early intercalation of Li^+ ($Li_xCo_2O_3$), and the phase changes brought about during the electrochemical conversion sequence [189]. Other reported 1D Co_3O_4 nanostructures of note include C/Co_3O_4 nanowires [191], CNT-templated porous nanotubes [192], solution-grown needle-like nanotubes [193], nanoneedles [194], and nanobelts [195]. In particular, mesoporous Co_3O_4 nanobelts, which were prepared by the calcination of α-$Co(OH)_2$ nanobelts, delivered high capacity and stable early cycling. The mesopore size could be somewhat tailored by altering the calcination temperature, which ultimately impacted the electrochemical performance. The Co_3O_4 nanobelts delivered capacities of up to ~1900 mA h g^{-1} in the first cycle (at a current density of 40 mA g^{-1}), and displayed a reversible capacity of ~1400 mA h g^{-1} after 20 cycles. Although the unique structuring enabled high capacity at relatively low rates, the nanobelts ultimately suffered from poor rate performance, with stable capacities only obtained at C-rate [195]. Other recent examples of Co_3O_4 nanostructures

demonstrated include nanosheets [196], multi-shelled hollow spheres [197] and octahedral nanocages [198]. Of these examples, the 2D nanosheet structures prepared by Zhan et al. [196], offered considerable capacity, to as much as 1450 mA h g^{-1} at the 27th cycle (end of test). The hydrothermal treatment, resulting in the transformation of $Co(OH)_2$ nanosheets to Co_3O_4 nanosheets, subsequently attained porosity as a result of the structural contraction during formation. The resulting Co_3O_4 nanosheets therefore had high surface areas as a result of their mesoporosity (average pore diameter, 3.3 nm), as measured by N_2 sorption (69 m^2 g^{-1}). The high-surface area, combined with the unique structuring enabled the Co_3O_4 nanosheets to achieve capacities far in excess of theoretical limits (1450 vs. 892 mA h g^{-1}, respectively).

Due to the poor electronic conductivity of Co_3O_4, various attempts have been made to improve the stable capacities and rate performance of Co_3O_4 anodes [199], including the addition of highly conducting additives such as graphene [199–203] and silver nanoparticles [204]. For example, Co_3O_4 nanoparticles (10–30 nm), anchored on graphene sheets displayed a considerably improved rate performance compared to bare Co_3O_4 samples at the same rate (Fig. 17) [202]. Since graphene remains essentially intact on cycling, it may offer itself as a structural scaffold, supporting the volume and phase changes brought about during the electrochemical conversion of Co_3O_4. The Co_3O_4/graphene composites displayed capacities increasing to 935 mA h g^{-1} after 30 cycles with a Coulombic efficiency of ~98%, while also displaying enhanced rate performance versus bare Co_3O_4 samples. Bare Co_3O_4 samples exhibited poor capacity retention while pure graphene samples displayed stable cycling, albeit at much lower capacity than Co_3O_4/graphene. These results suggest an important role of structural buffers and increasing electronic conductivity on the anodic performance of Co_3O_4 electrodes.

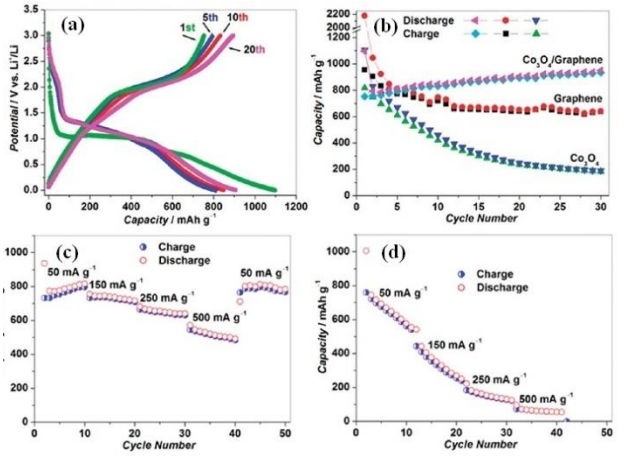

Figure 17 (a) Charge-discharge curves of Co_3O_4/graphene composites over 1 – 50 cycles, (b) capacity as a function of cycle number for Co_3O_4/graphene and bare graphene and Co_3O_4, (c) performance of Co_3O_4/graphene and (d) rate performance of bare Co_3O_4. Reproduced from [202]. Copyright 2010 American Chemical Society.

1.6.3 Other metal oxides

Oxides of other first-row transition (Mn, Ni, Cu, Zn), and second-row (Mo) metals are also considered as potential anodes and are electrochemically active in either conversion modes or via typical intercalation mechanisms depending on their nature.

Recent examples of note include reports of NiO nanocones [205], and MoO_3/C nanobelts [206], which display high capacity and excellent cycling ability. NiO nanocones, which were prepared by the electrodeposition of acidic $NiCl_2.6H_2O$ solutions directly on Ni foams, offered capacities in excess of 1000 mA h g^{-1}, even after 100 cycles. NiO offers a theoretical capacity of 717 mA h g^{-1} thus the reversible capacity delivered by the NiO nanocones was some ~50% higher than might be expected. These results also represent the highest reversible capacity reported for NiO nanostructures to-date. More encouraging still, was the high rate capability of the nanocones (rates of 20 C delivered capacities as high as 436 mA h g^{-1}), while offering capacities up to initial values on returning to relatively low current rates (C/10) [205]. In contrast, hydrothermally prepared MoO_3 nanobelts, with carbon layers in the order of 15 nm, delivered

equivalent performance, maintaining capacities greater than 1000 mA h g^{-1} after 50 cycles [206]. MoO_3, a relatively inexpensive second-row transition metal oxide, has a theoretical Li^+ capacity equivalent to 1120 mA h g^{-1} (via $6e^-$) and therefore represents an appealing Li-ion candidate. MoO_3, however, is a poor electronic conductor and may display poor electrochemical performance as a result. The carbon-coated MoO_3 nanobelts demonstrated considerable enhancement over their bare nanobelt counterparts (Fig. 18), owing in part to the increased conductivity, structural support and volumetric buffering capabilities of the carbon layer [206]. The capacities displayed by these and other examples seen previously (Table 2) are far in excess of today's conventional graphite anodes and thus may represent one of the major building blocks of future Li-ion batteries.

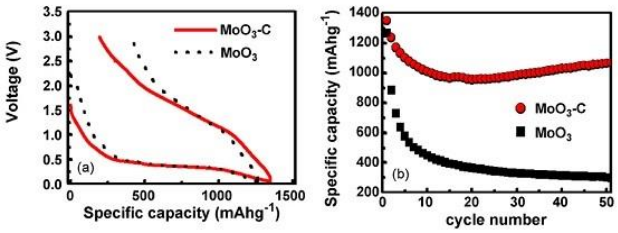

Figure 18 (a) First charge–discharge curves of MoO_3 nanobelts and (b) cycling performance of MoO_3–C and bare MoO_3 nanobelts outlining significant improvement of the carbon-coated nanobelts. Adapted from [206] with permission from Elsevier.

Table 2 Recently reported TMO anodes; discharge capacities are given in mA h g^{-1} while the relevant rate and cycle number is displayed in brackets.

Composition	Morphology	Initial Capacity	Final Capacity	Ref
MnO	Powder	~600 (50 mAg^{-1})	~650 (50)	[207]
MnO/C	Nanotubes	1129 (0.13 C)	763 (100)	[208]
α-MnO_2	Nanotubes	~600 (200 mA g^{-1})	618 (300)	[209]
MnO_2/CNTs	Coaxial (tubes)	2170 (50 mA g^{-1})	~500 (15)	[210]
MnO_2/CNTs	Nanoflakes	~800 (200 mA g^{-1})	620 (50)	[211]
MnO_2/CNFs	Particles/fibres	785 (50 mA g^{-1})	597 (50)	[212]
Mn_3O_4/rGO	NPs/sheets	810 (40 mA g^{-1})	~900 (5)	[213]
NiO	Nanowall	685 (895 mA g^{-1})	638 (80)	[214]
NiO	Foam	1020 (0.2 C)	746 (10)	[215]
NiO	Nanoflakes	~818 (50 mA g^{-1})	412 (20)	[216]
NiO	Nanocones	1151 (0.4 C)	1058 (100)	[205]
NiO/Co	Film	~1200 (100 mA g^{-1})	~600 (50)	[217]
NiO/Graphene	Nanosheets	1478 (50 mA g^{-1})	~1000 (50)	[218]
NiO/Graphene	Nanosheets	1398 (100 mA g^{-1})	982 (50)	[219]
NiO/MWCNTs	Tubes/chains	~1084 (50 mA g^{-1})	~861 (50)	[220]
NiO	Mesoporous	924 (0.1 C)	680 (50)	[221]
CuO	Pine-needles	~1015 (1C)	~626 (100)	[222]
CuO	Nanobundles	1179 (0.3 C)	666 (70)	[223]
CuO	Nanowires	~800 (0.1 C)	680 (30)	[224]
CuO	Nanowires	1040 (0.05 mA cm^{-2})	650 (100)	[225]

CuO	Nanoribbons	866 (175 mA g^{-1})	608 (275)	[226]
CuO	Nanosheets	~966(1C)	640 (100)	[227]
CuO	Nanorods	1500 (0.5 C)	650 (100)	[228]
CuO	Fibres/network	~980 (0.2 mA cm^{-2})	520 (50)	[229]
CuO	Nanotube film	911 (0.02 mA cm^{-2})	417 (30)	[230]
CuO/Graphene	Nanocomposite	~620 (65 mA g^{-1})	~600 (100)	[231]
CuO/Graphene	Nanocomposite	817 (67 mA g^{-1})	423 (50)	[232]
CuO/Graphene	Nanosheets	1092 (70 mA g^{-1})	~800 (40)	[233]
CuO/CNTs	Porous/tubes	~1200 (C/10)	~680 (100)	[234]
CuO/MWCNTs	Plates/tubes	~1380 (60 mA g^{-1})	627 (50)	[235]
ZnO	Nanorod array	1461 (0.1 mA cm^{-2})	310 (40)	[236]
ZnO	Nanosheets	1120 (50 mA g^{-1})	~400 (100)	[237]
ZnO/C	Nanorods	1150 (C/5)	~500 (50)	[238]
ZnO/Au	Flower-like	1280 (120 mA g^{-1})	~390 (50)	[239]
ZnO/Ni	Nanorods	1048 (80 mA g^{-1})	490 (30)	[240]
MoO_2	Mesoporous	960 (C/20)	750 (30)	[241]
MoO_2	Monolith	~587 (200 mA g^{-1})	~719 (20)	[242]
MoO_2/C	Nanospheres	750 (1C)	~650	[243]
MoO_2/C	Nanofibres	923 (50 mA g^{-1})	763 (50)	[244]
MoO_2/C	Nanocrystals	1040 (200 mA g^{-1})	629 (50)	[245]
MoO_3	Nanoparticles	~560 (C/2)	~620 (150)	[246]
MoO_3	Nanoparticles	1400 (C/10)	1050 (30)	[247]
MoO_3/C	Nanobelts	~1370 (C/10)	1064 (50)	[206]

2 Recent developments in nanostructured cathode architectures

Developing improved Li-ion cathodes perhaps represents the biggest opportunity for performance gain over existing battery design. Cathodes may be considered as one of the bottlenecks of the Li-ion cell, displaying capacities far lower than potential anodes while often being poor electronic conductors. Existing cathodes, namely $LiCoO_2$ and $LiMn_2O_4$ have now been in widespread use for many years despite displaying relatively limited electrochemical performance. Future Li-ion cathodes must possess the necessary requisites such as increased energy density, improved rate performance, cycle life and safety, if they are to find application in next-generation devices and EV/HEVs. Careful selection of cathode materials together with an improvement over existing design through the use of nanostructuring, dopants/composites or surface coatings, may represent several avenues to enhance Li-ion battery performance. In this section, some of the recent developments in the development of nanostructured cathode materials finding application as potential candidates in next-generation Li-ion batteries are highlighted.

2.1 Lithiated metal-oxides (LiM_xO_y)

Lithium metal oxides, LiM_xO_y (M = Co, Mn, etc.), represent an important class of Li-ion cathodes and

have found commercial application through $LiCoO_2$ extending over a number of years. Typically, LiM_xO_y cathodes are conventional intercalation hosts and involve redox chemistries of $1e^-$ transfer during electrochemical cycling. While single electron processes generally yield lower specific capacity, LiM_xO_y cathodes may operate at relatively high voltages (3.0–4.2 V) thus achieving relatively modest energy densities.

2.1.1 $LiCoO_2$

$LiCoO_2$ has been a viable success in commercial Li-ion cells years after being identified as a potential intercalation host by Goodenough et al. in 1981 [248]. While there has been a distinct move for alternative electrode hosts ($LiCoO_2$ is both toxic and relatively expensive to produce), research has still considered a number of practical $LiCoO_2$ architectures with high voltage and good rate performance [249–257]. In the interest of capacity retention, commercial $LiCoO_2$ cells typically adopt a reversible capacity to 0.5 Li^+ by setting the upper-cut off potential to 4.2 V, thus yielding working capacities approaching 150 mA h g^{-1} [258]. A theoretical capacity of 294 mA h g^{-1} awaits full utilisation of $LiCoO_2$, although capacity fade as a result of high charging potentials has so far been restricting. Perhaps the most realistic solution for preventing capacity fade may be found through surface modification, or by the addition of protective surface layers [259–261]. Surface layers, for example, may act as nanometric barriers, potentially thwarting much of the undesirable interactions at the electrode–electrolyte interface, such as those originating through the oxidation of electrolyte solutions. Such interactions may become markedly increased as a result of high charging potentials and are explicitly indicated in nanostructured materials whose higher surface areas result in greater exposure to the electrolyte. Limiting the occurrence of potentially poisonous interactions is therefore highly advantageous to the cycle life of the electrode. Recent studies have demonstrated nanometre-scale coatings of inactive Al_2O_3 on $LiCoO_2$ nanoparticles [256,262,263]. In the first example, $LiCoO_2$ particles prepared by a molten-salt synthesis using CoO, LiOH and KNO_3, were subjected to consecutive ALD cycles, each depositing a thin-film of Al_2O_3 ranging between 1.1–2.2 Å in thickness. The gravimetric capacity of the Al_2O_3-coated particles far surpassed that of bare nano- and bulk- sized $LiCoO_2$ particles over the potential range of 3.3–4.5 V. The nanoscale coatings also resulted in enhanced rate-capability, exhibiting a capacity of 133 mA h g^{-1} at a high rate of 7 C (Fig. 19). Importantly, however, when increasing the thickness of Al_2O_3 beyond 2 successive atomic layer deposition (ALD) cycles, the cells displayed worsened rate performance, due to poor Li^+ conductivity. These results demonstrate the necessity for potential barrier layers to remain appreciably thin, on the order of a few nm.

Cheng et al. [263], have also demonstrated cycling performance of Al_2O_3 coatings while extending their study to include TiO_2-coated $LiCoO_2$ particles. Both passivating layers were deposited by an ALD process using $Al(CH_3)_3$ and $Ti(OCH(CH_3)_2)_4$ as Al_2O_3 and TiO_2 precursors, respectively. Evaluation of the electrochemical performance over a range of layer thicknesses, also tailored by adjusting the number of consecutive ALD cycles, returned similar findings to the previous report [262]. Substantially increasing layer thickness (up to 500 ALD cycles), resulted in lower capacity and poor retention, even compared to bare $LiCoO_2$ particles, while the highest capacity and most stable cycling was seen in samples with the thinnest layers of Al_2O_3 (10 ALD cycles). Interestingly, TiO_2-coated $LiCoO_2$ particles fared considerably worse than their bare counterparts, which was ascribed to the insertion of Ti^{4+} into the $LiCoO_2$ host, forming a redox-active interlayer of $LiTi_yCo_{1-y}O_{2+0.5y}$, consuming TiO_2 in the process. The relationship between any potential surface layers and electrode must therefore remain inactive if surface passivation is to impart purposeful character [263].

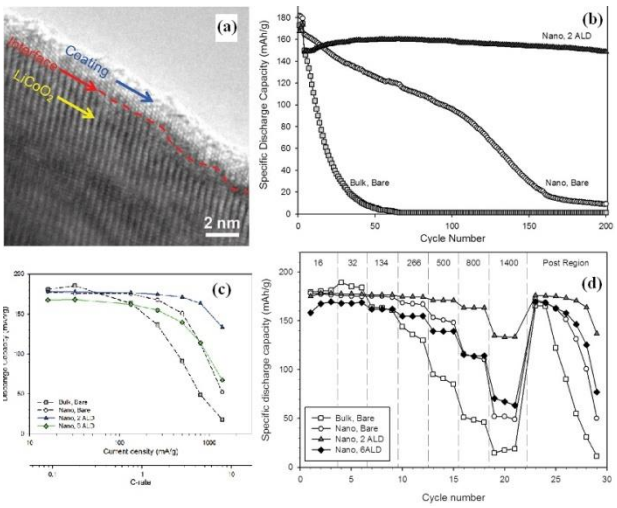

Figure 19 (a) High-resolution TEM micrograph of Al_2O_3-coated $LiCoO_2$ particles, (b) cycling performance of Al_2O_3-coated $LiCoO_2$ particles versus bare nano- and bulk- sized $LiCoO_2$ particles, (c) and (d) performance rate of Al_2O_3-coated $LiCoO_2$ particles with 2 or 6 ALD cycles, and bare nano- and bulk- sized $LiCoO_2$ particles. Adapted with permission from [262]. Copyright 2011 American Chemical Society.

2.1.2 $LiMn_xO_y$

Spinel-$LiMn_2O_4$ has emerged as one of the most promising cathode candidates and has found mainstream utilisation in Korean and Japanese Li-ion battery markets [264]. With a theoretical capacity of 142 mA h g^{-1} and a practical working voltage of between 4.0–4.2 V, $LiMn_2O_4$ cathodes could potentially display energy densities in excess of 600 W h kg^{-1}. Coupled with relatively low production costs and appreciable electrochemical performance at high discharge rates and elevated temperatures, $LiMn_2O_4$ is touted as a potential driver of future EV/HEV battery packs, notably against favourable $LiFePO_4$ candidates [264]. Recent nanostructured morphologies of note include nanowires [265–267], nanorods [268–272], nanotubes [273], nanoparticles [269,274–276] and ordered meso/porous electrodes [277,278]. Okubo et al. [275] have demonstrated an important size-effect occurring in $LiMn_2O_4$ particles, confirming that bulk particle sizes are unable to achieve complete lithiation (up to $Li_2Mn_2O_4$), due to their lower surface area. Instances where intercalation results in insertion of greater than one equivalent of Li^+ ($Li_xMn_2O_4$ $1 < x < 2$), are met by a structural transition from tetragonal to cubic spinel phase resulting in large unit cell expansion [279]. For bulk particles, a core–shell structure is suggested, where shells exist entirely of the tetragonal spinel phase which is solely active towards intercalation. Smaller diameter particles of $Li_2Mn_2O_4$ (<43 nm), however, were shown to accommodate near stoichiometric amounts of Li^+ while those of sizes <15 nm did so via solid-state processes, without domain boundaries. The boundary-less mechanism facilitated capacities of greater than 160 mA h g^{-1} at rates as high as 10 C, far exceeding those of bulk and larger sized (43 nm) particles [275]. Such size-effects could therefore account for the enhanced rate capability displayed by small diameter $LiMn_2O_4$ nanorods [270–272], and nanowires [265–267], which possess both high power and enhanced cycling ability. In particular, high-aspect ratio nanowires with mean diameters <10 nm and lengths of several μm, displayed large capacities at rates up to 75 C, and even to as much as 150 C [267]. The ultra-thin $LiMn_2O_4$ nanowires (Fig. 20), synthesised by treating solvothermally prepared α-MnO_2 nanowires with LiOH at reduced pressure, were single-crystalline in nature while their small diameter enabled accommodation of the large lattice parameter changes brought about by the cubic to tetragonal phase transitions. Larger diameter $LiMn_2O_4$ nanowires also showed good structural stability, maintaining their single-crystalline nature (as confirmed by selected area electron diffraction (SAED) analysis), even after 100 charge–discharge cycles [265]. Such results suggest that $LiMn_2O_4$ nanowires could represent the basis of potential high-power, high-rate Li-ion batteries.

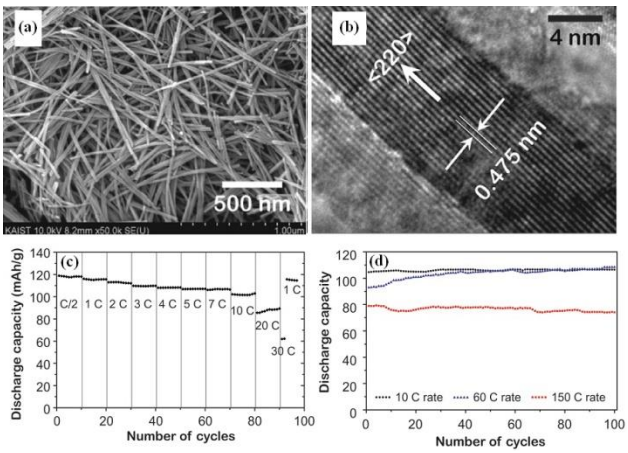

Figure 20 (a) SEM image of $LiMn_2O_4$ nanowires after solid state treatment with LiOH, (b) TEM image revealing a <220> growth direction, (c) performance rate between C/2 and 30 C and (d) discharge as a function of cycle number for rates 10 – 150 C . Adapted with permission from [267]. Copyright 2010 American Chemical Society.

Although nanostructuring of $LiMn_2O_4$ electrodes may provide a means of enhanced strain relaxation induced by electrochemical cycling, it should be noted that $LiMn_2O_4$ also suffers from reduced cycling efficiency as a result of dissolution of Mn^{3+} in organic electrolytes. Dissolution of Mn^{3+} is driven by a disproportionation reaction ($2Mn^{3+} \rightarrow Mn^{2+} + Mn^{4+}$) facilitated by HF, whose origins may arise from the interaction of surface water with $LiPF_6$ salts [264]. Various methods including nanoscale coatings [272,280–282], and dopants [270,283,284] have been introduced to protect $LiMn_2O_4$ nanostructures from dissolution, thus enhancing their cyclic behaviour. Cho prepared VO_x-coated $LiMn_2O_4$ nanorod clusters which displayed comparable performance rates while successfully reducing Mn^{3+} dissolution from 5000 ppm to 60 ppm at 80 °C (as measured by mass spectrometry) [272]. Improved cycling performance and reduced dissolution was also obtained by coating $LiMn_2O_4$ particles with lithium boron oxide (LBO) [280]. A more-detailed depiction of the unfavourable interaction of Mn^{3+} with $LiPF_6$-based electrolytes is reported by Yang et al. [270]. The single nanorod devices (Fig. 21), consisting of Al-doped $LiAl_{0.1}Mn_{1.9}O_4$, displayed a significantly reduced amount of etching compared to either pure λ-MnO_2 or $LiMn_2O_4$ nanorods after comparable exposure time in $LiPF_6$ electrolytes at 60 °C. Current–voltage (I–V) measurements collected after the same exposure times also showed reduced conductivity among the λ-MnO_2 or $LiMn_2O_4$ samples (Fig. 22), while the Al-doped $LiAl_{0.1}Mn_{1.9}O_4$ nanorod devices remained largely unchanged. Cycling studies of the $LiAl_{0.1}Mn_{1.9}O_4$ nanorod samples also showed an improvement in capacity fading versus their un-doped counterparts, further corroborating previous results. Such evidence outlines the practical importance of controlling Mn^{3+} dissolution in order to impart both structural stability and long-term cycling capabilities of future $LiMn_2O_4$ electrodes.

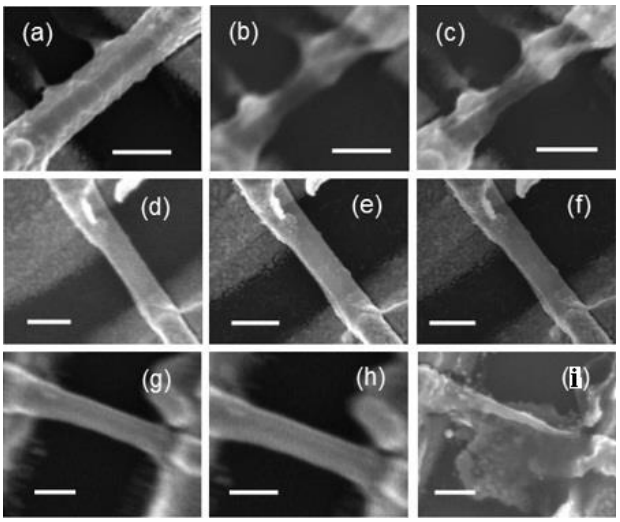

Figure 21SEM images of single nanorod devices of (a-c) $LiMn_2O_4$ after 3, 6 and 9 h respectively, (d-f) $LiAl_{0.1}Mn_{1.9}O_4$ and (g-i) λ-MnO_2 after the same exposure times. Reprinted with permission from [270]. Copyright 2009 American Chemical Society.

Although somewhat less reported in recent times, the synthesis of the $LiMnO_2$ cathode is still worth mentioning, especially since it offers over twice the theoretical capacity of LiM_2O_4 (285 vs. 140 mA h g^{-1}), while still involving the same $Mn^{4+/3+}$ redox couple [285,286]. Although the 3D framework of LiM_2O_4 allows for efficient Li^+ transfer, layered orthorhombic $LiMnO_2$ still presents a channelled framework, structurally analogous to that of $LiCoO_2$ (α-$NaFeO_2$ structure). However, early cycling of orthorhombic $LiMnO_2$ for $x > 0.5$ (Li_xMnO_2), results

in some structural transformation from the α-$NaFeO_2$ structure to that of cubic spinel ($LiMn_2O_4$) phase [287]. The transition is believed to be a result of the displacement of Mn atoms into neighbouring octahedral sites, favouring the nucleation and growth of new spinel nanodomains [4,287]. While the transition seemingly affects the initial cycling behaviour of $LiMnO_2$, an insignificant contribution is suggested for the 5th and subsequent cycles [287].

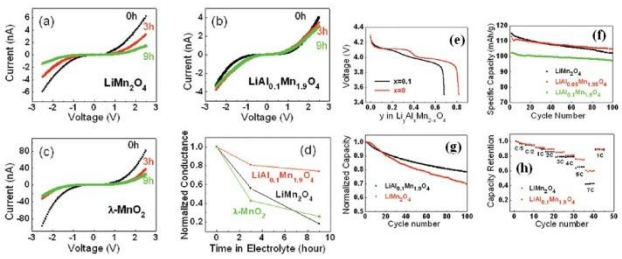

Figure 22. I-V curves of (a) $LiMn_2O_4$, (b) $LiAl_{0.1}Mn_{1.9}O_4$, (c) λ-MnO_2 and (d) normalised conductance and a function of exposure time in $LiPF_6$ electrolyte. (e) First discharge plot of $LiMn_2O_4$ and $LiAl_{0.1}Mn_{1.9}O_4$ cells at a rate of C/5, (f) cycling of $LiMn_2O_4$, $LiAl_{0.1}Mn_{1.9}O_4$ and λ-MnO_2 at a rate of C/5 at room temperature and (g) 60 °C. (h) Rate-performance of the $LiMn_2O_4$ and $LiAl_{0.1}Mn_{1.9}O_4$ cells at room temperature. Reprinted with permission from [270]. Copyright 2009 American Chemical Society.

Recently published reports of various nanostructured Li/MnO_2 architectures include nanorods/nanoparticles [288], mesoporous [289] and nanocrystalline solids [286,290,291]. For example, the hydrothermal treatment of γ-MnOOH nanorod templates with LiOH at 200 °C resulted in orthorhombic $LiMnO_2$ nanorods which delivered a capacity of 180 mA h g^{-1} after 30 cycles [288]. Notably, the nanorod structures fared considerably better than nanoparticle samples also prepared by hydrothermal methods. The increased capacity was attributed to the unique 1D morphology, through which better strain accommodation and facile Li^+ transport may have resulted. Early increases in capacity during electrochemical cycling however, suggests some spinel formation may have occurred although this remained unquantified in the study [288]. Capacity fade as a result of cubic spinel formation may, however, ultimately render $LiMnO_2$ electrodes unviable candidates unless such transitions are facilitated.

2.1.3 Mixed spinel and layered oxides

Doping of spinel-phase $LiMn_2O_4$ with metals such as Al results in enhanced electrode performance, through the structural support imparted by the metal dopant species [284]. Another possible alleviation of the HF-driven Mn^{3+} dissolution process may be afforded by the partial substitution of transition metals (Co, Ni, Cu etc.) into the solid structure, thus restricting the Mn^{3+} species under feasible operating voltages. As a prominent example, the Mn-rich $LiMn_{2-x}Ni_xO_4$ electrodes [292–299], which consist primarily of Mn^{4+}, should not succumb to such undesirable interactions with electrolytes. Substitution of Mn with Ni, as opposed to other transition metals, has been met favourably due to good cycling stability, access to the $Ni^{4+/3+}$ redox couple below 4.9 V and the appearance of only one distinct plateau in the voltage profile (~4.7 V), compared to a bi-plateauing afforded by other transition metals [299]. In particular, 5 V spinel $LiMn_{1.5}Ni_{0.5}O_4$ electrodes have attracted considerable attention in recent times and are reviewed in some detail by Santhanam and Rambabu [299]. A few drawbacks of $LiMn_{1.5}Ni_{0.5}O_4$ electrodes, however, mar their application: The formation of an impurity phase $Li_xNi_{1-x}O$ seemingly worsens electrochemical performance over time and while accessible, the $Ni^{4+/3+}$ redox couple falls at potentials where electrolyte decomposition is prevalent. Addition of other transition metal cations into $LiMn_{2-x}Ni_xO_4$ systems has been adopted and could prevent the formation of $Li_xNi_{1-x}O$ phases, together with reducing the cycling-induced lattice expansion [292,300–304]. As an example, partial substitution of Fe for Mn or Ni in $LiMn_{1.5}Ni_{0.5}O_4$ electrodes has led to enhanced electrochemical activity, most notably in terms of cycling stability and rate performance [292]. Moving away from spinel-phase oxides, layered candidates such as $Li[Ni_{1/3}Co_{1/3}Mn_{1/3}]O_2$ [305–312], or the so-called

"Li-excess" solid solution Li_2MnO_3-$LiMO_2$ electrodes, (e.g., $Li[Li_{1/9}Ni_{1/3}Mn_{5/9}]$ [313] and $Li[Ni_xLi_{(1/3-2x/3)}Mn_{(2x-3-x/3)}]O_2$ [296,314,315], have attracted much attention owing to an enhancement of capacity and cyclic behaviour. Kim et al. [296], prepared $Li[Li_{0.15}Ni_{0.25}Mn_{0.6}]O_2$ nanowires primarily consisting of the layered hexagonal α-$NaFeO_2$ phase, having high aspect ratio and diameters of approximately 30 nm, by a pH-controlled hydrothermal treatment of $Ni_{0.3}Mn_{0.7}O_2$ precursors at 200 °C. The nanowires displayed a high surface area of 65 $m^2\ g^{-1}$ with lengths exceeding 1 μm (Fig. 23). At the rate of 0.3 C, the $Li[Li_{0.15}Ni_{0.25}Mn_{0.6}]O_2$ nanowires displayed high performance, reaching a capacity of 367 mA h g^{-1} in the first cycle and up to ~285 mA h g^{-1} in the following 80 cycles. By varying the pH, the same synthesis conditions produced nanoplate morphologies of $Li[Li_{0.15}Ni_{0.25}Mn_{0.6}]O_2$ which fared considerably worse than their nanowire counterparts (Fig. 24). Notably, the rate capability of the nanowire samples was far improved, displaying ~250 mA h g^{-1} at a high rate of 7 C. The nanowire electrodes also remained structurally intact after 80 charge–discharge cycles, outlining their potential use as high-rate Li^+-ion cathodes.

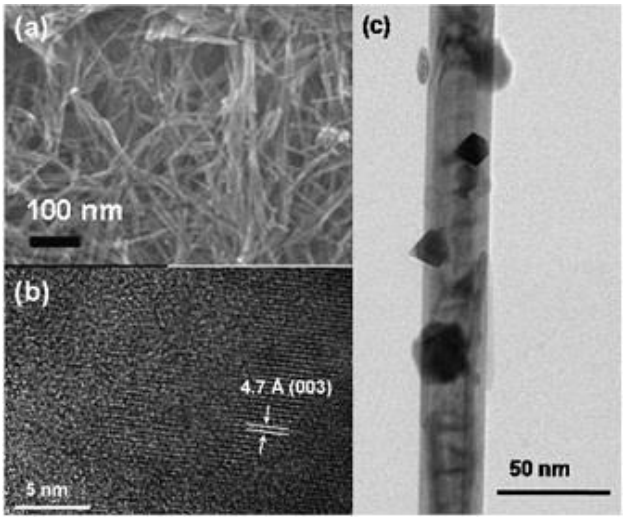

Figure 23 (a) to (c) TEM images of the $Li[Li_{0.15}Ni_{0.25}Mn_{0.6}]O_2$ nanowires after hydrothermal treatment at pH 2 and at 200°C [296]. Reproduced by permission of The Royal Society of Chemistry.

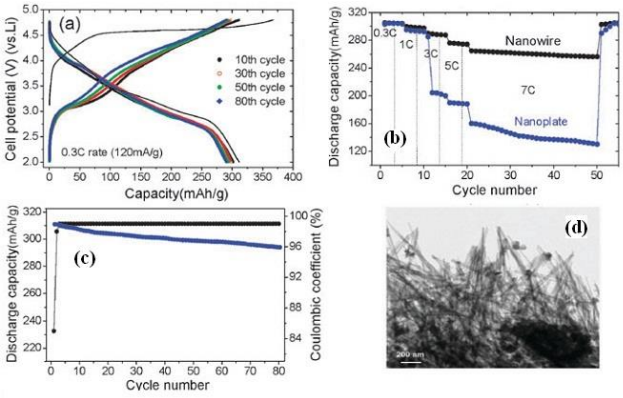

Figure 24(a) Voltage profiles of $Li[Li_{0.15}Ni_{0.25}Mn_{0.6}]O_2$ nanowires at a rate of 0.3 C between 4.8 – 2.0 V, (b) rate and (c) cyclic performance/Coulombic efficiency and (d) TEM image of the nanowire electrodes after 80 charge-discharge cycles [296]. Reproduced by permission of The Royal Society of Chemistry.

In comparison, crystallographically tailored $Li[Li_{0.17}Ni_{0.25}Mn_{0.58}]O_2$ nanoplates prepared by Wei and co-workers [314], exhibited appreciable cycle life and discharge capacities exceeding 200 mA h g^{-1}, with high-rate performance at current rates up to 6 C. The high performance of the $Li[Li_{0.17}Ni_{0.25}Mn_{0.58}]O_2$ nanoplates was attributed to their precise crystallographic orientation which was favourable to Li^+ interaction: In the layered α-$NaFeO_2$ structures, Li^+ intercalation is only entertained in a direction parallel to the Li^+-layers. The (001) planes, which lie perpendicular to the c-axis in the α-$NaFeO_2$ crystal, remain dominant when nanoplate growth is facilitated in a direction perpendicular to the c-axis. Such orientation leads to large inefficiencies as the dominant (001) planes do not provide an appropriate path for Li^+ transport. Growth perpendicular to (001) planes (along the c-axis), however, results in (001) or (100) dominant planes which are active to Li^+ transport (Fig. 25). Thus, tailoring a synthesis to obtain either a- or b-axis oriented nanoplates could facilitate an improved electrochemical response. Such a product was obtained by a shortened hydrothermal synthesis which led to the growth of nanoplates in the <010> and <001> directions, resulting in nanoplates whose (010) faces predominate. At a rate

of ~0.2 C, the crystallographically-tuned nanoplates delivered a discharge capacity of 238 mA h g^{-1} after 100 cycles. The nanoplates also performed well at the high testing rate of 6 C, delivering a capacity approximately twice that of a more thermodynamically-favoured nanoplate sample, which grew along the <001> direction and whose (001) faces predominate. Further electrochemical gain could be sought by increasing the ratio of (010)- to (001)-nanoplates in the tailored sample, which was estimated by XRD to be in the order of 6.4:1, respectively [314]. Such results however, outline the importance of synthetically tailoring layered α-$NaFeO_2$ nanomaterials if one is to develop an improved electrochemical response. The structural stability, high operating voltage, relatively high capacity and good rate performance of α-$NaFeO_2$-structured LNMO electrodes make them appealing future candidates.

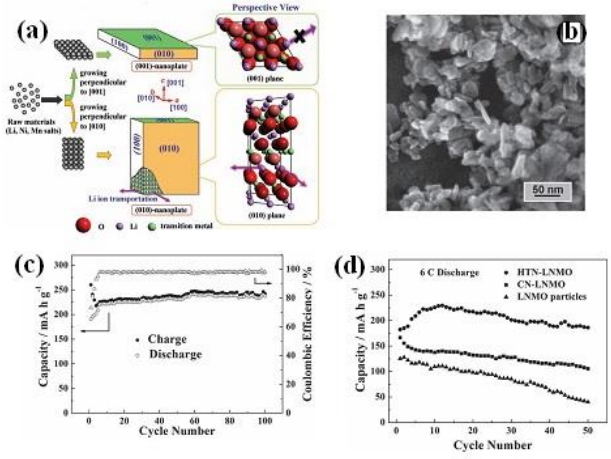

Figure 25 (a) Illustrative representation of the synthesis of (001) and (010) dominant $Li[Li_{0.17}Ni_{0.25}Mn_{0.58}]O_2$ nanoplates, (b) SEM image of the (010) nanoplates, (c) cycling and Coulombic efficiency studies of (010) nanoplates at a current density of 60 mA g^{-1} between 2.0 – 4.8 V and (d) cycling of (010)-nanoplates (HTN-LNMO), (001)-nanoplates (CN-LMNO) and LNMO particles at 6 C rate. Adapted from [314]. Copyright Wiley-VCH Verlag GmbH & Co. KGaA. Reproduced with permission.

2.1.4 Vanadium/lithiated vanadium oxide (V_2O_5/LiV_3O_8)

V_2O_5 offers access to its redox couples at relatively high potentials, making it an attractive candidate as a positive Li-ion electrode. Through its layered structure, as shown in Fig. 26, intercalation of guest species such as Li^+, is facilitated through perovskite-like vacancies [316,317]. As a consequence of intercalation, V_2O_5 undergoes a series of structural modifications, based on a puckering or gliding of the layers, depending on the amount of Li^+ inserted ($Li_xV_2O_5$). These modifications involve the reversible formation of an α-phase for values of $x < 0.1$, to an ε-phase for $0.35 < x < 0.7$, and to a δ-phase for $0.9 < x \leq 1.0$. A metastable γ- phase develops subsequently offering reversible intercalation over $0 < x < 2.0$, yielding theoretical capacities in the region of 290 mA h g^{-1} [318,319]. Although further capacity is initially possible, saturation of the γ- phase with Li^+ ($x > 2.0$) leads to the formation of an irreversible cubic ω-phase having a typical rock-salt structure. Whilst this structure minimises internal electrostatic interactions [318], electrochemical cycling of the ω-phase is often only considered for values of x between $0.4 < x < 3.0$ [320]. Completely reversible Li^+ intercalation has yet to be demonstrated by electrochemical means; thus far, complete de-lithiation has only been achieved through chemical treatment of V_2O_5 nanorods with Br_2, resulting in the reformation of the pristine orthorhombic phase [321]. Since the formation of cubic ω-V_2O_5 for both bulk and nanostructured V_2O_5 is known at potentials <2.0 V, electrochemical cycling with strict lower cut-off potentials may hinder its formation if applicable, resulting in stable cycling of the γ-phase over the region of $0.0 \leq x \leq 2.0$.

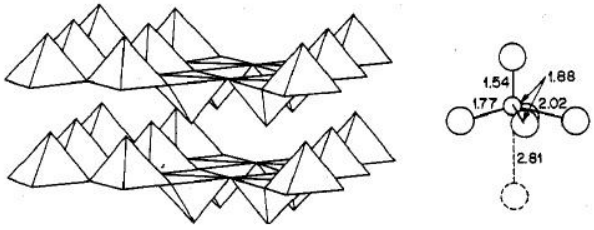

Figure 26 Structure of layered V_2O_5 (left) depicting square pyramidal VO_5 units which share both corner and edges and the

associated bond distances (right) within a VO_6 octahedra, which facilitate a separation and weak interaction between layers. Reproduced with permission from [322]. Copyright 1979 American Chemical Society.

A great deal of research has been published recently concerning the electrochemistry of nanostructured V_2O_5, owing to its significant intercalation properties. Various morphologies which have been reported recently include nanorods [321,323,324], nanowires/fibres [323,325–333], nanobelts [334–337], nanotubes [331,338,339], spheres [340–343], nanourchins [344,345], meso/porous particles [326,341,346,347], carbon nanocomposites [348–350], and thin-films [351,352]. 1D nanostructures (i.e., nanowires, nanofibres, nanobelts and nanotubes), have been of particular interest given their unique physical properties and have been prepared by various techniques, most notably by electrospinning [326,328,329,331,332] and hydrothermal methods [324,325,327,335,338,353,354]. Electrospinning is an interesting technique where a high voltage is employed to accelerate a liquid jet of charged polymeric solution towards a grounded collector. A continuous fibre forms as a result of stretching due to electrostatic repulsions between surface charges, and the evaporation of solvent [355]. An overview of the process and application of electrospinning has been succinctly summarised in various review articles, to which the reader is referred [355,356]. Wang et al. [331] recently prepared 1D V_2O_5 nanostructures by an electrospinning method combined with subsequent thermal annealing (Fig. 27). Three distinct morphologies were obtained by controlling the annealing temperature, producing porous nanotubes (400 °C), hierarchical nanofibres (500 °C) and single-crystalline nanobelts (600 °C), from the as-obtained electrospun nanofibres. The formation of the individual morphologies was ascribed to temperature dependent mechanisms, where the transition from the smooth electrospun nanofibres to porous nanotubes occurred at temperatures above 400 °C due to the complete thermal decomposition of PVP, while the continuous growth of V_2O_5 nanograins at higher temperatures regions (500–600 °C), resulted in the loss of porous morphologies forming first hierarchical nanofibres and finally to the larger, single-crystalline nanobelts. The 1D porous nanotubes exhibited stable cycling performance over 250 cycles in the range of 2.5–4.0 V, with near theoretical initial capacities attained (138 mA h g^{-1}) at 0.1 A g^{-1}, with a capacity retention of ~80% at the 250th cycle (Fig. 28). Furthermore, the porous nanotubes displayed stable cycling (~72% capacity retention), under test rates up to 6 A g^{-1}, while at current densities as high as 15 A g^{-1}, the nanotubes still delivered ~65 mA h g^{-1} resulting in a discharge energy density of 201 Wh kg^{-1} and a high power density of ~40.2 kW kg^{-1}. Cycling of the nanotubes over the range of 2.0–4.0 V resulted in high initial capacities (~276 mA h g^{-1}), although rapid capacity fading was evident over successive cycles. The cyclic stability was improved in the hierarchical nanofibres and further still among the single-crystalline nanobelts, although such morphologies displayed lower capacities over comparative test rates. The increase in cyclic stability among the nanobelt electrodes was ascribed to their specific crystallographic orientation, which limited the thickness in the unfavourable [001] direction (c-axis). The thin nanobelt morphology was maintained over 100 electrochemical cycles which indicated the nanobelt structure was able to withstand the volume strain associated with successive intercalation mechanisms. Importantly, the contrasting electrochemical performance of the individual nanostructures prepared by the same electrospinning method outlines the importance of crystallization factors and morphology on the overall Li-ion performance of V_2O_5 cathodes.

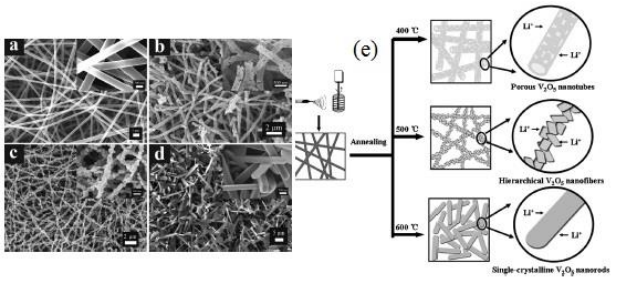

Figure 27 SEM images of (a) as-prepared electrospun nanofibres, (b) porous nanotubes, (c) hierarchical nanofibres and (d) single-crystalline nanobelts. (e) Schematic representation of the formation of the individual nanostructures. Adapted from [331]. Copyright Wiley-VCH Verlag GmbH & Co. KGaA. Reproduced with permission.

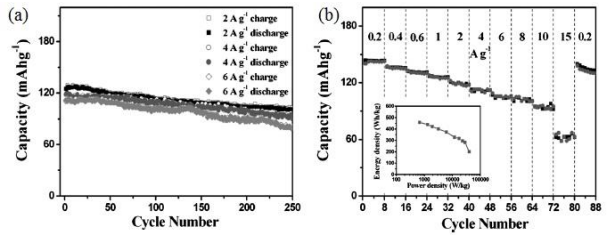

Figure 28 Electrochemical performance of the porous V_2O_5 nanotubes showing (a) discharge capacity as a function of cycle number and (b) rate performance over current densities 0.2 – 15 – 0.2 A g^{-1}. Adapted from [331]. Copyright Wiley-VCH Verlag GmbH & Co. KGaA. Reproduced with permission

The importance of structure, crystallinity and order for V_2O_5 was also demonstrated to strongly influence its Li-ion insertion capacities. V_2O_5 nanotubes synthesised using amine templates impeded Li ion insertion by blocking sites due to functionalisation of the high surface area of tubes, rendering them worse than simple xerogel counterparts. All vanadate structures are heavily reliant on the vanadate conformation and valency [357,358]. After hydrothermal treatment, the resultant morphologies and constituent phases are dependent on the degree of hydration, or protonation, within the vanadium oxide lamina and not solely on the intercalated structural organic template used. By forming nanourchin morphologies (Fig. 29), O'Dwyer et al. [359] demonstrated that the reduced amine uptake during synthetic functionalisation when making nanotubes in radial arrays such as nanourchin forms, frees up the V_2O_5 (010) surface within the high surface area material, allowing improved density and rate for Li ion insertion.

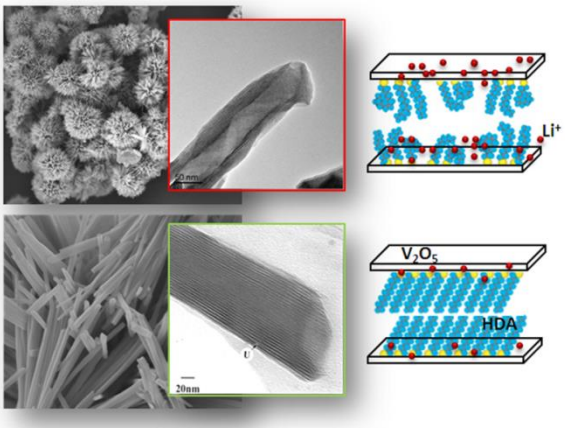

Figure 29 Nano-urchin and nanotubes of V2O5 grown using a primary amine template. Minimizing the density of amine between V_2O_5 lamina markedly improved the ability of the nanotube to intercalate a higher capacity of Li-ions. Adapted from [359]. Copyright Wiley-VCH Verlag GmbH & Co. KGaA. Reproduced with permission.

High-resolution TEM studies revealed the unique observation of nanometer-scale nanocrystals of pristine unreacted V_2O_5 throughout the length of the nanotubes in the nanourchin. Electrochemical intercalation studies revealed that the very well ordered xerogel-based nanotubes exhibit similar specific capacities (235 mA h g^{-1}) to Na^+-exchange nanorolls of VO_x (200 mA h g^{-1}). By comparison, the theoretical maximum value is reported to be 240 mA h g^{-1}. The nanotubes of the nanourchin 3-D assemblies, however, exhibit high charge capacities exceeding 437 mA h g^{-1}, which demonstrates the benefit of template removal and nanostructuring of the crystalline phases in V_2O_5 structures.

Electrospinning has also been employed recently in the synthesis of 1D V_2O_5 nanowires which display enhanced Li-ion performance [326,328,329,332]. For example, Mai et al. [329], prepared ultra-long V_2O_5 nanowires with diameters between 100–200 nm and lengths of several millimetres, by electrospinning a solution of poly

(vinyl alcohol) and NH_4VO_3 under an applied voltage of 20 kV. The as-obtained fibres were subsequently treated at 480 °C in air which facilitated the concurrent decomposition of the PVA scaffold and crystallisation of V_2O_5. The resultant hierarchical V_2O_5 nanowires, which were composed of connected V_2O_5 nanorods, displayed initial and 50th discharge capacities of 275 and 187 mA h g^{-1} (68% retention), respectively, between 2.0–4.0 V at a current density of 30 mA g^{-1}. Cycling over the 1.75–4.0 range (ω-phase), resulted in higher initial capacities (390 mA h g^{-1}), although the cells attained a lower capacity retention of ~52% at the same discharge rate. Confirmation of the morphological advantage was presented by comparison to hydrothermally prepared V_2O_5 nanorods which displayed ~110 mA h g^{-1} under the same conditions [329]. In contrast, centimetre long V_2O_5 nanowires of between 80–120 nm in diameter prepared by conventional hydrothermal methods, delivered a high initial capacity of 351 mA h g^{-1} and up to 175 mA h g^{-1} after 20 cycles between 1.75–4.0 V at a current density of 50 mA g^{-1}. Although some capacity fade was evident, the V_2O_5 nanowire samples still delivered a Coulombic efficiency of ~99%, highlighting the good reversibility in the charge–discharge process. The V_2O_5 nanowires also displayed high performance in other applications such as field emission and photoconductivity, outlining their potential capacity for use in photodetectors or optoelectronic devices [325]. A novel hybrid material consisting of 1D V_2O_5 nanowires and 2D graphene nanosheets, which was prepared by a hydrothermal treatment of V_2O_5 powder with H_2O_2, delivered high Li-ion performance as a result of the kinetic enhancement of the highly conducting graphene nanosheets [327]. V_2O_5 itself has an electrical conductivity of between 10^{-2}–10^{-3} S cm^{-1} in the bulk form [360], which may limit its application in high-rate Li-ion batteries. Increasing electrical conductivity within a V_2O_5 cathode is therefore likely to benefit the overall rate performance. Indeed, the V_2O_5 nanowire–graphene nanosheet composite delivered high initial discharge capacities of 412 mA h g^{-1} at a current density of 50 mA g^{-1}, and up to 316 mA h g^{-1} at current densities as high as 1.6 A g^{-1} (1.5–4.0 V). Electrochemical cycling resulted in some capacity fading; however, the composite electrode still delivered capacities of up to 190 mA h g^{-1} at the C rate (400 mA g^{-1}). Improvement in the cyclic stability of such V_2O_5 composites could lead to their use in higher rate-demanding applications. Although 1D nanostructures are appealing candidates given their unique properties, V_2O_5 nanostructures taking other forms have also shown high capacity and stable cycling. A recent notable example is demonstrated by Zhang et al. [361], who prepared carbon-coated V_2O_5 nanocrystals which delivered high capacities (~130 mA h g^{-1}) at test rates of up to 68 C (10 A g^{-1}). Such rate capability is thus far unknown amongst V_2O_5 cathodes. The carbon-coated V_2O_5 crystals were prepared by the impregnation of mesoporous carbon monolith templates with molten V_2O_5 at a temperature of 750 °C under vacuum, followed by the removal of most of the carbon template by thermal treatment at 600 °C in air. The resultant carbon-coated V_2O_5 nanocrystals of 10–20 nm in diameter, aggregated to form secondary particles of several hundred nanometres in diameter. In addition to the high rate performance, the carbon-coated V_2O_5 cathodes displayed stable cycling over 50 cycles at current densities ranging between 1–10 A g^{-1} (Fig. 30). More explicitly, capacities as high as 255 mA h g^{-1} could be recovered after 50 cycles at a current density of 2 A g^{-1}, and up to 155 mA h g^{-1} at 5 A g^{-1}. These results lie among the highest reported capacities for V_2O_5 under such current rates, which has been ascribed to the short Li^+ diffusion lengths of the nanoscale particles, combined with the interstitial spacing which allows for efficient electrolyte access and the increased electronic conductivity offered by the carbon coatings. Moreover, the high cyclic stability, which is often problematic in V_2O_5 electrodes, coupled with the relatively facile synthesis route could make them potential candidates as future high performance Li-ion cathodes.

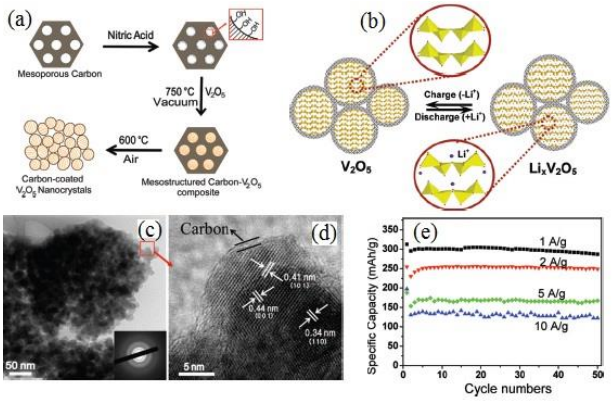

Figure 30 Schematic representation of (a) the synthesis route to obtain carbon-coated V_2O_5 nanocrystals, (b) the structuring features allowing facile intercalation, (c-d) TEM images of carbon-coated V_2O_5 nanocrystals (inset: selected area electron diffraction pattern) and (e) cycling performance at current densities of 1, 2, 5 and 10 A g^{-1}. Adapted with permission from [361]. Copyright 2011 American Chemical Society.

The lithiated tri-vanadate, LiV_3O_8, is another class of vanadium oxide material which has attracted attention, largely due to its high theoretical capacity of 372 mA h g^{-1}, assuming a complete 4 e^- transfer mechanism. Such capacities are one of the highest known amongst all positive electrodes. LiV_3O_8 also displays a layered structure consisting of VO_6 octahedra and distorted VO_5 trigonal bipyramids grouped as sheets, which share edges and corners [362]. A number of LiV_3O_8 nanostructures have been reported in the literature recently, including nanorods [363–368], nanowires [369], nanosheets [370,371], and nanoparticles [372]. Xu et al. [369], have recently synthesised one of the first large-scale examples of LiV_3O_8 nanowires by a topotactic conversion of structurally analogous $H_2V_3O_8$ nanowires. The $H_2V_3O_8$ nanowires, which were prepared previously by hydrothermal methods, were subsequently mixed in an ethanolic solution of LiOH and thermally treated 400–500 °C. The resultant LiV_3O_8 nanowires remained largely similar to their $H_2V_3O_8$ precursors, although some structural changes, such as the loss of smooth surfaces were evidenced from microscopy analysis. The chosen annealing temperature was determined to be an important factor in the overall electrochemical performance of the LiV_3O_8 nanowires, where temperatures of 450 °C led to the highest performance, which was ascribed to the high degree of crystallinity and largest surface area among all prepared samples (400, 450 and 500 °C). Galvanostatic testing over the potential range of 1.5–4.0 V, returned encouraging results with initial discharge capacities of 176 mA h g^{-1} reported at a high current density of 1.5 A g^{-1}, which attained up to 160 mA h g^{-1} after some 400 charge–discharge cycles. Similarly, the first and 600th cycles collected at a higher current density of 2 A g^{-1}, still returned 137 and 120 mA h g^{-1}, respectively. At lower test rates (20 mA g^{-1}), up to 318 mA h g^{-1} could be attained, which remained largely stable over 20 cycles. Such results outline the tremendous potential of 1D LiV_3O_8 in future high rate Li-ion batteries.

In another recent example, Shi and co-workers [368], demonstrated significantly high capacity in their [100]-oriented LiV_3O_8 nanorods, which were encased in an amorphous LiV_3O_8 wrapping (Fig. 31). The thin-film sample, which was prepared by RF-sputtering onto stainless steel substrates, was controlled by adjusting levels of Ar and O_2. Importantly, the level of O_2 was found to affect the nature of LiV_3O_8 crystallisation, where a dominantly [100] oriented sample could be obtained by maintaining a 2:1 ratio of Ar:O_2, respectively. The crystallographically-tailored LiV_3O_8 thin-films returned a first discharge capacity as high as 388 mA h g^{-1} at the C/5 rate, and 350 mA h g^{-1} after 40 cycles (Fig. 31(b)). In the same instance, the Coulombic efficiency remained at ~100%, indicating a high degree of reversibility in the cycling process. The high capacity was attributed to the unique structuring, where the amorphous LiV_3O_8 wrapping provided a 3D pathway for Li^+ diffusion to the favourable (100) plane, while further, the amorphous wrapping may itself provide Li^+ storage before transfer to the (100) plane. Also encouraging, was the high rate performance of the wrapped LiV_3O_8 nanorods, where large capacities of 102 mA h g^{-1} could be obtained at a rate of 40 C (a ~45 s discharge), and up to ~80 mA h g^{-1} at a rate of 50 C

[368]. Both the stable, high capacity cycling and high rate performance of this example outline the tremendous potential of the LiV_3O_8 cathode. Future work may evolve to produce further examples of nanostructured LiV_3O_8 cathodes displaying paralleled performance.

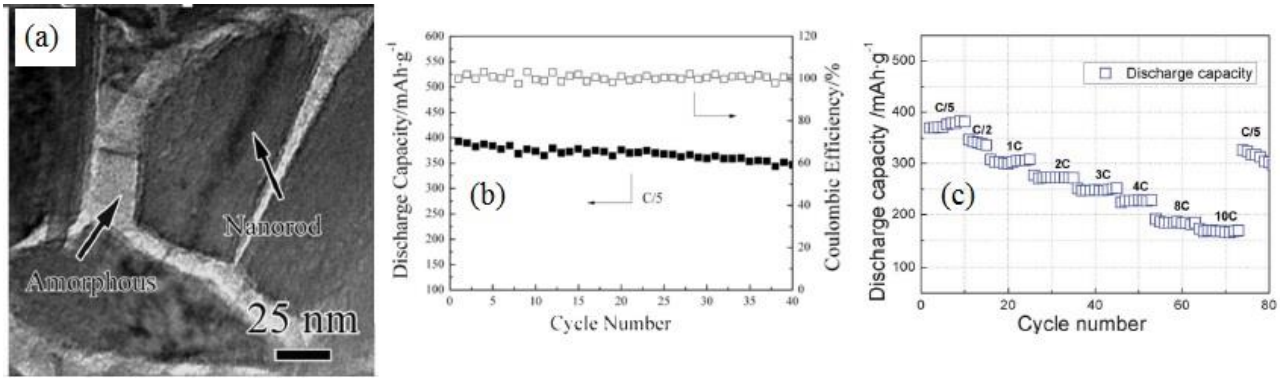

Figure 31 (a) TEM image of a LiV_3O_8 film showing LiV_3O_8 nanorods wrapped in an amorphous LiV_3O_8 layer, (b) discharge capacity as a function of cycle number and the related Coulombic efficiency taken over the potential range 1.5 – 4.0 V and at charge-discharge rate of C/5 and (c) the performance rate of the LiV_3O_8 film showing discharge capacities over the rates C/5, C/2, 1 C, 2 C, 3 C, 4 C, 8 C and 10 C [368]. Adapted with permission of The Royal Society of Chemistry.

2.2 Polyanion cathodes

2.2.1 $LiFePO_4$ (LFP)

LFP cathodes have received tremendous academic attention over recent years since its introduction by Padhi et al. [373]. Given its extreme popularity, several recent review articles have covered its progress in detail [374–376]. LFP's olivine framework enables rapid Li^+ transport [377], and is stabilised by the electron-withdrawing nature of the PO_4^{3-} polyanion. The strong P–O covalent bond reduces the relative strength of the covalent interaction to the neighbouring Fe, thus lowering the $Fe^{4+/3+}$ redox couple energy and providing stable operating voltages of ~3.5 V, with good reversibility [378]. LFP electrodes are also relatively inexpensive to prepare, non-toxic and environmentally benign, all factors which have become increasingly important over recent years. LFP electrodes do, however, suffer from relatively low theoretical capacities (~170 mA h g^{-1}), and poor electrical conductivity (10^{-9} S cm^{-1}), which may set a degree of limitation on its future application. Developing nanostructured LFP-based electrodes with enhanced properties through surface modifications such as carbon coating or via carbon compositing is now commonplace [379–420], and has enabled almost complete intrinsic utilisation of LFP. Table 3 highlights a selection of some recent developments in LFP nanoarchitectures.

The mechanism of Li^+ intercalation in LFP electrodes has been a hotbed of intense study [421–424], and is even more the remarkable given LFP's high-rate capability whilst remaining both a poor ionic and electrical conductor. A generalised notion is that Li^+ de/intercalation occurs via a two-phase nucleation and growth process involving both Li_xFePO_4 and $Li_{1-x}FePO_4$ end-phases. Intercalation is, however, predicted to differ on reducing particle size to nanodimensions given the variation in surface and interface energies at the nanoscale [375]. Recently, the high-rate capability of LFP nanoparticles has been identified as a result of a single-phase transformation process, thus removing the kinetic limitations of nucleation and growth of two separate, $LiFePO_4$ and $FePO_4$ phases [423,425]. Although considerations are far from complete on this matter, nanostructuring is predicted to offer significant benefits to the intercalation chemistry of LFP cathodes and is now predictably commonplace.

Zhu et al. [392] have recently demonstrated one of the first examples of truly single-crystalline

$LiFePO_4$ nanowires which contain a uniform and moderately thick (2–5 nm) carbon-coating, leading to enhanced electrochemical ability. The ~100 nm wires, which are smaller than those previously reported for LFP [426,427], were deposited on stainless steel substrates by electrospinning an aqueous solution of $Fe(NO_3)_3$, LiH_2PO_4 and poly(ethylene oxide) (PEO), using an accelerating voltage of 15 kV before thermal annealing at 700 °C under flowing N_2. TEM analysis revealed that the LFP nanowires grew along the c-axis, leading to facile Li^+ transport and a potentially high-rate response along the shortened b- and a-axis, while the carbon coating ensured adequate electrical conductivity and minimal aggregation throughout the electrode.

Table 3 LFP nanostructured electrodes; the rate and cycle number are given in brackets.

Composition	Morphology	Initial Capacity	Final Capacity	Ref
$LiFePO_4$	Powder (various)	~150 (C/10)	~150 (20)	[428]
$LiFePO_4$	Nanoparticles	~160 (C/10)	~160 (100)	[429]
$LiFePO_4$	Nanoparticles	~120 (C/10)	~120 (60)	[425]
$LiFePO_4$	Porous (hollow)	~165 (1 C)	~165 (80)	[427]
$LiFePO_4$	Nanoporous	~135 (2 C)	~135 (50)	[430]
$LiFePO_4$	Powder (various)	166 (C/10)	~165 (50)	[431]
$LiFePO_4$	Platelets	151 (C/10)	~151 (30)	[432]
$LiFePO_4$	Powder (various)	167 (C/10)	142 (30)	[433]
$LiFePO_4$	Dumbbell	100 (C/30)	110 (70)	[434]
$LiFePO_4$	Nanorods	150 (5 C)	~155 (5)	[435]
$LiFePO_4$	Mesocrystals	150 (2 C)	~155 (150)	[436]
$LiFePO_4$/C/PPy	Porous spheres	~140 (0.1C)	~150 (20)	[437]
$LiFePO_4$/C/PPy	Nanocrystals	~155 (0.1 C)	~155 (20)	[438]
$LiFePO_4$/C	Porous spheres	153 (0.1 C)	~150 (5)	[439]
$LiFePO_4$/C	Nanoparticles	126 (20 C)	~112 (1000)	[440]
$LiFePO_4$/C	Nanoplates	~165 (0.1 C)	~160 (50)	[441]
$LiFePO_4$/C	Nanocrystals	~160 (0.2 C)	158 (100)	[442]
$LiFePO_4$/C	Nanowires	150 (1 C)	146 (100)	[392]
$LiFePO_4$/C	Nanocomposite	~163 (0.1 C)	162 (100)	[406]
$LiFePO_4$/C	Nanoplates	~165 (0.1 C)	~165 (50)	[402]
$LiFePO_4$/C	Nanocomposite	~168 (0.1 C)	~160 (1100)	[384]
$LiFePO_4$/C	Nanorods	~160 (0.1 C)	~160 (30)	[403]
$LiFePO_4$/CNT	Nanocomposite	~160 (10 mA g^{-1})	~160 (10)	[399]
$LiFePO_4$/GO	Nanocomposite	~145 (1 C)	~145 (5)	[443]
$LiFePO_4$/ZnO_2	Particles	~140 (0.1 C)	~143 (100)	[444]

Li-ion performance (Fig. 32), was recorded over several discharge rates with a first discharge capacity of 169 mA h g^{-1} (between 2.5–4.3 V vs. Li/Li^+), and as much as 93 mA h g^{-1} at the high discharge rate of 10 C. Cycling of the LFP nanowires resulted in stable performance with 146 mA h g^{-1} obtained after 100 cycles at the C rate. Furthermore, the LFP nanowires remained structurally stable (evidenced to at least 25 cycles), which was observed by the single-crystalline nature under TEM imaging and SAED analysis. A high electrochemical performance was also achieved at the elevated operating temperature of 60 °C, with such cells displaying stable cycling (C rate) close to the theoretical maximum; capacity retention was expressed as 98% of the initial capacity after 100 charge-discharge cycles [392]. The electrochemical performance of the single-crystalline LFP nanowires exceeded those of CNT–LFP tri-axial nanowire composites prepared by a similar electrospinning process [426]. The increased performance is attributed to the smaller diameter nanowires (~100 nm), versus the larger CNT-LFP composite (~500 nm), resulting in shorter Li^+ diffusion paths. While the low-current performance of the LFP nanowires displays close to theoretical capacity (170 mA h g^{-1}), further performance increases at high rates could potentially be sought by scaling the diameters of c-axis nanowires further, particularly as ionic and electronic transport in single crystalline LFP is governed by particle size [445], and through a quasi, two-dimensional movement along the b–c plane [446].

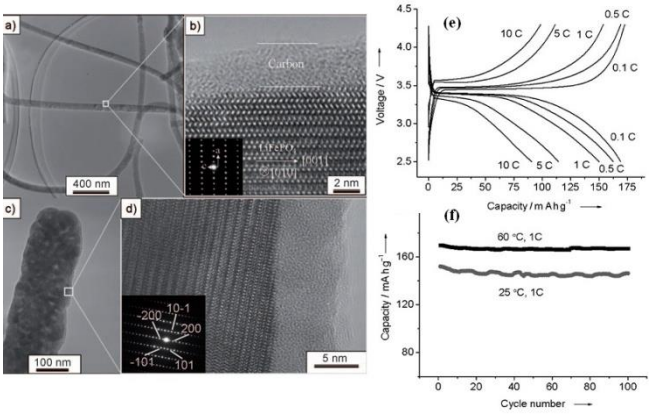

Figure 32 TEM images of (a,b) single-crystalline LFP nanowires, (c,d) LFP nanowires collected *ex-situ* after 25 charge-discharge cycles, (e) typical voltage curves for LFP nanowires at various rates between 2.5 – 4.3 V and (f) cycling performance of the LFP nanowires at a rate of 1 C at 60 and 25 °C. Adapted from [392]. Copyright Wiley-VCH Verlag GmbH & Co. KGaA. Reproduced with permission.

A high rate capability and appreciable cyclic stability is also found amongst nanoplate morphologies of LFP, whose unique nanostructuring results in diminishing b-axis dimensions conducive to Li^+ transport [402,440,441]. Therefore, the thickness of LFP nanoplates, together with the nature of their synthesis, is likely to heavily impact the electrochemical performance of LFP nanoplates. Saravanan and co-workers [402,441] recently demonstrated the advantage of using nanoplate morphologies and compared the unique structuring to spindle and diamond-shaped LFP cathodes [402]. The LFP nanoplates were prepared by a solvothermal process (ethylene glycol) at 270 °C, using Fe(oxalate) as an iron precursor, LiH_2PO_4 as Li^+ and PO_4^{3-}C sources, and D-gluconic acid, serving as carbon former. After a subsequent thermal treatment at 450 °C under a reducing atmosphere, carbon-coated LFP nanoplates were obtained whose thickness was in the order of 30–40 nm. Replacing the Fe precursor with $Fe(acac)_2$, (acacH = acetylacetonate) $Fe(gluconate)_2$ or Fe(PMIDA) (PMIDA = *N*-(phosphonomethyl)iminodiacetate) resulted in LFP spindles (aggregated nanoplates), diamonds or thick plate (200–300 nm) morphologies, respectively.

During galvanostatic testing (Fig. 33), the LFP nanoplate morphologies fared considerably better than thick plate morphologies, whose increased thickness resulted in the expansion of the b-axis parameter, and LFP spindles, whose thinner (~20 nm) but tightly agglomerated LFP nanoplates did not allow for efficient electrolyte access [402]. The hierarchical, open structuring of the LFP nanoplates, which allowed near theoretical capacities at low-rates (C/10), therefore underlines the appreciable contribution that morphology has on the electrochemical response of LFP and other potential electrodes.

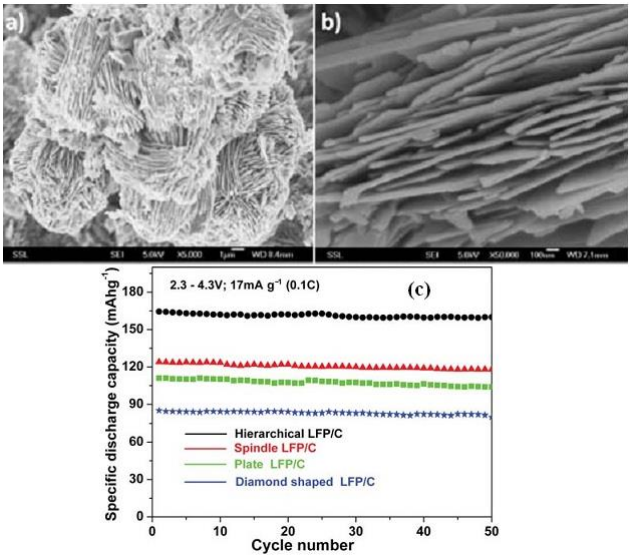

Figure 33 (a, b) SEM images of $LiFePO_4$/C nanoplates with thicknesses of 30 – 40 nm prepared by a solvothermal process at 270 °C (scale bar 1 μm and 100 nm) and (c) discharge capacity as a function of cycle number for the hierarchical LFP/C nanoplates, spindle, diamond and thick plate morphology LFP electrodes [402]. Adapted with permission of The Royal Society of Chemistry.

LFP nanoparticles are also appealing choices and have extended cycling ability and good rate capability [384,425,429,440]. As a notable example, Yang et al. [440], prepared large-scale carbon-coated LFP nanoparticles by a PEG-assisted (PEG = polyethylene glycol) hydrothermal reaction of $FeSO_4$, H_3PO_4 and LiOH at 180 °C for 24 h. Adjusting the synthetic conditions such as reaction time, temperature and the PEG:H_2O ratio, could yield products having nanoparticle, nanoplate and microplate morphologies depending on exact conditions. The rod-like LFP nanoparticles, which had an average size of 58 nm, were favoured at higher reaction temperatures (180–220 °C), and displayed enhanced performance over their nanoplate counterparts. Both samples fared considerably better than the thick LFP plates, which is in agreement with previous reports [402]. With an addition of 30 wt.% of the conductive carbon black Super P, the LFP nanoparticles displayed extended cycle performance at a high discharge rate of 20 C, resulting in capacities in the region of 112 mA h g^{-1} after 1000 cycles (~89% capacity retention). A similar high-rate performance was also displayed by the LFP/C nanoplates, although such morphologies ultimately offered a poorer capacity retention (~78%), yielding a final capacity of approximately 100 mA h g^{-1} after 1000 cycles.

The high rate capability of LFP nanoparticles is thus far showcased in the example of Kang and Ceder [377], whose surface-modified LFP nanoparticles displayed exceptional performance, even at test rates as high as 397 C. The authors suggest increasing Li^+ conduction across the surface of the LFP nanoparticle towards the (010) facet is likely to facilitate rapid intercalation kinetics since it is known that intercalation of Li^+ into bulk LFP crystals is only possible in the [010] direction. An amorphous layer of lithium phosphate was chosen as the surface enhancer due to its abilities to enhance Li^+ mobility and the potential for such surfaces to be doped with metallic atoms resulting in enhanced electronic conductivity. TEM analysis confirmed the amorphous nature of the surface layer, showing it to be in the region of 5 nm against the 50 nm diameter of the LFP nanoparticles. The electrochemical testing (Fig. 34), revealed the surface-modified LFP electrodes could return high Li-ion performance with near theoretical capacity attained at discharge rates of 2 C, and up to 80% of capacity at a high rate of 50 C. Cycling of the nanoparticles at rates of 20 and 60 C resulted in

stable performance with no apparent reduction in capacity after 50 cycles. Utilising a configuration of 60 wt.% carbon black as conductive agent, albeit industrially impractical but important in terms of achieving conductivity through the electrode assembly, revealed that the surface-modified LFP nanoparticles could attain capacities of ~100 and ~60 mA h g^{-1} after 100 cycles at rates of 197 and 397 C, respectively. These results demonstrate the ability of LFP as a potential high power electrode capable of ultrafast charging and discharging, which may necessarily bring dramatic change to the way that batteries are conceived in the future [377]. The results outlined in this section demonstrate that LFP electrodes may represent the most common alternative to $LiCoO_2$ or $LiMn_2O_4$ cathodes for some time to come. The high-rate and near-theoretical capacity display of LFP electrodes, coupled with their relatively affordable production cost and low environmental impact make them one of the most promising Li-ion solutions. In addition, the appreciable thermal stability and high charge rates at relatively high operating temperatures (~60 °C), may allow its targeted use in automotive EV/HEV applications [264]. Although LFP electrodes display some incompatibility at elevated temperature (dissolution of Fe^{3+} under storage in conventional electrolytes is known), various electrolyte (e.g., Li_2CO_3) and electrode additives (coatings, etc.), may be used to limit problematic interactions with organic-based electrolyte solutions [264].

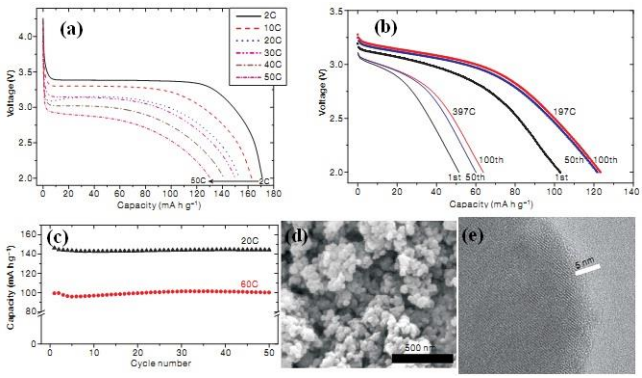

Figure 34 (a) Typical voltage curves for surface-modified LFP nanoparticles at different discharge rates (2 – 50 C), (b) voltage curves of surface-modified LFP nanoparticles at the high rates of 197 and 397 C (carbon addition 65 wt. %), (c) cycling performance of the nanoparticles at 20 and 60 C, (d) SEM and (e) TEM images of the surface-modified LFP nanoparticles [377]. Adapted with permission from Macmillan Publishers Ltd: Nature Materials [377]. Copyright (2009).

2.2.2 Other transition metal phosphates ($LiMPO_4$)

Transition metal phosphates such as $LiMnPO_4$, $LiCoPO_4$ and $LiVOPO_4$, have also been studied as potential cathodes, notably as their theoretical capacity and working potentials may exceed those of $LiFePO_4$. One such example is $LiMnPO_4$ [447–458], which is isostructural to that of olivine $LiFePO_4$, while possessing a higher operating voltage (4.1 vs. 3.5 V, respectively) [378,448], and hence energy densities which could exceed 700 Wh kg^{-1}. At this point, it should be suggested that $LiMnPO_4$ represents a more realistic candidate compared to $LiCoPO_4$ or $LiNiPO_4$, since the working voltage of $LiCoPO_4$ or $LiNiPO_4$ electrodes (4.9 and 5.1 V, respectively), currently lies outside regions of stability of the commonly-employed organic (carbonate) electrolytes [378]. Early examples of $LiMnPO_4$ electrodes, however, were unable to demonstrate appreciable electrochemical activity [373], until a solid-state reaction involving the addition of carbon black to the reactant mixture enabled a capacity of 140 mA h g^{-1} to be extracted [448]. The addition of carbon black resulted in a reduction of particle size while acting as an electrically conductive agent, which is particularly necessary for the operation of $LiMnPO_4$ electrodes given that the inherent electrical conductivity in

$LiMnPO_4$ (10^{-10} S cm^{-1}) is considerably lower than that of $LiFePO_4$ (10^{-8} S cm^{-1}) [457]. In more recent reports, carbon-coated nanostructures have enabled stable cycling as a result of diminishing Li^+ diffusion paths, accommodation of the volume induced change on cycling (~9.5%) [459], and enhanced electrical conductivity. Choi and co-workers [458], have demonstrated enhanced performance of carbon-coated $LiMnPO_4$ nanoplates, with stable cycling and high gravimetric capacity. The $LiMnPO_4$ nanoplates, which were in the order of 50 nm thick, were prepared by a surfactant (oleic acid)-assisted solid-state reaction of $MnCO_3$ and $NH_4H_2PO_4$, with molten paraffin serving as co-solvent. Although TEM analysis revealed the thinnest portion of the nanoplates was in fact along the a-axis (unfavourable for Li^+ transport), the $LiMnPO_4$ nanoplates still delivered near theoretical capacity at a C/50 rate, reaching a discharge capacity of 168 mA h g^{-1}. Cycling at higher C rates, however, resulted in diminished performance (a discharge capacity of 54 mA h g^{-1} was achieved), unless a fixed charging rate of C/25 rate was adopted. With such charging rates, stable capacities to over 50 charge discharge cycles at test rates up to 2 C were obtained. Oh and co-workers [447], prepared $LiMnPO_4$/C nanocomposite powders with test rates of up to 10 C reported. The $LiMnPO_4$/C nanocomposites were prepared by an ultrasonic spray pyrolysis method followed by subsequent ball-milling, resulting in $LiMnPO_4$ particles of between 10–50 nm. Similarly, the $LiMnPO_4$/C cells were charged to 4.5 V at the slow rate of C/20 for the cycle tests (plus additional holding at 4.5 V until C/100), where the addition of 30 wt.% carbon black during ball-milling was found to offer the highest capacity of ~130 mA h g^{-1} (C/2 rate). Cycling at the higher operating temperature of 55 °C resulted in initial capacity gains (vs. 25 °C), due to an increase in the Li^+ diffusion rate experienced at the higher temperature, however, the $LiMnPO_4$/C cells suffered from capacity decline as a result of the HF-driven Mn^{3+} dissolution in organic electrolyte. $LiMnPO_4$/C cells with an optimal level of carbon addition (30 wt.%), displayed greater stability which was suggested to be the result of a more adequate carbon coverage throughout the electrode (40 wt.% C addition led to an agglomeration of C particles) [447]. While these results offer an insight into the possible utilisation of $LiMnPO_4$ as a future Li-ion cathode, the inherently low ionic and electronic conductivities, coupled with an incompatibility at elevated temperature [455], likely preclude its use in future high-rate Li-ion batteries. Further work is therefore needed to redress such limitations.

A competitive alternative to Fe and Mn based phosphates could be found through the lithiated vanadyl phosphates, namely $LiVOPO_4$ [460–463], the fluorinated derivative $LiVPO_4F$ [464,465], and $Li_3V_2(PO_4)_3$ [466–489]. $LiVOPO_4$ which crystallises in two electrochemically active α- (triclinic) and β-(orthorhombic) forms, has a theoretical capacity of 166 mA h g^{-1} and through a ~3.9 V operating voltage, may yield specific energy densities in excess of ~640 Wh kg^{-1}. Equally, $Li_3V_2(PO_4)_3$, which has a high theoretical capacity of 197 mA h g^{-1}, could yield cells whose specific energies exceed 750 Wh kg^{-1}. Recently, Saravanan et al. [490], prepared hollow sphere morphologies of α-$LiVOPO_4$, a phase which is suggested to be more crystallographically favourable to Li^+ intercalation than its polymorph twin, β-$LiVOPO_4$ [491]. The structure of α-$LiVOPO_4$ may be described as columns of close-packed vanadium oxide octahedra, where the interstitial sites are filled alternatively by P and Li atoms. In contrast, β-$LiVOPO_4$ contains a P atom in every other empty site while the Li atoms are located between the coordination polyhedra of the V and P atoms, and neighboured by six oxygen atoms to form a distorted octahedra. The edge lengths of which are much smaller (2.463–3.404 Å), than twice the ionic radius of the Li^+ ion (4.24 Å) [491]. Consequently, β-$LiVOPO_4$ may suffer from poor rate capability. The α-$LiVOPO_4$ spheres, which themselves were comprised of agglomerated nanoplates, were prepared by an ethylene glycol (EG)-assisted solvothermal treatment of $V(acac)_3$, LiOH and $NH_4H_2PO_4$ between 240–260 °C. The hollow spheres, which could be tailored somewhat by adjusting the solvothermal conditions such as

reaction time, temperature and EG content, delivered a first discharge capacity of 145 mA h g^{-1} (~87% of the theoretical capacity) between 3.0–4.5 V at the C/10 rate. Cycling under the same conditions resulted in initial capacity fade, which stabilised after ~25 cycles and delivered approximately 100 mA h g^{-1} after 50 cycles. The rate capability was also demonstrated up to current rates of 13 C, which delivered up to 22 mA h g^{-1} over the same potential regime. Monoclinic $Li_3V_2(PO_4)_3$ has perhaps attracted greater attention [466–489], owing in part to its higher theoretical capacity (~199 mA h g^{-1}, assuming 3 Li^+ insertions are attained). Carbon coatings or carbon composite formation is commonplace due to the inherently poor electronic conductivity of $Li_3V_2(PO_4)_3$ (2.4×10^{-7} S cm^{-1}), which has resulted in cells attaining competitive performance. Early examples of hydrothermally prepared core–shell $Li_3V_2(PO_4)_3$@C composites, comprised of ~400 nm $Li_3V_2(PO_4)_3$ particles and a carbon shell of ~10 nm thickness, displayed a discharge capacity of approximately 130 mA h g^{-1} under a current density of 28 mA g^{-1}. The carbon-coated samples exhibited both enhanced rate capability and cyclic stability, retaining a discharge capacity of ~98.5% over 50 cycles while restricting the growth of passivating SEI layers [480]. Liu et al. [484], have recently exploited the electronic properties of graphene by forming a $Li_3V_2(PO_4)_3$/graphene nanocomposite which displayed considerable rate capability. The $Li_3V_2(PO_4)_3$/graphene nanocomposite was prepared by mixing $Li_3V_2(PO_4)$ precursors in a solution of partially reduced graphene oxide followed by sintering at 800 °C under N_2. The resultant $Li_3V_2(PO_4)_3$ nanoparticles (~40 nm), were uniformly dispersed and enwrapped in the partially reduced graphene sheets, thus forming a highly conductive network. The nanocomposite electrode delivered high electrochemical performance, with near theoretical discharge capacities achieved (~130 mA h g^{-1}), delivered at the C/10 rate (between 3.0–4.3 V vs. Li/Li^+). Cyclic voltammetry measurements of the $Li_3V_2(PO_4)_3$/graphene nanocomposite revealed a shaper set of redox pairs compared to pure $Li_3V_2(PO_4)_3$, with a smaller potential separation between peaks, indicating an increase in electrical conductivity and lower Ohmic resistance. On cycling between 3.0–4.8 V, where a third Li^+ extraction is possible up to 4.8 V, the $Li_3V_2(PO_4)_3$/graphene nanocomposite delivered high initial capacity at the C and 2C rates (>150 mA h g^{-1}), however, cells retained only ~80% of the initial capacity after 100 cycles [484].

Nanoscale coatings other than carbon have also been implemented to improve the performance of $Li_3V_2(PO_4)_3$ [482,488,489]. Recently, Zhang et al. [489], prepared $Li_3V_2(PO_4)_3$/C samples coated with a 3–5 nm layer of SiO_2 by mixing $Li_3V_2(PO_4)_3$/C powders in an ethanolic solution containing 1, 2 or 3 wt.% tetraethyl orthosilicate (TEOS). The SiO_2-coated powders fared noticeably better through rate testing (up to 5 C), and cycling studies than uncoated $Li_3V_2(PO_4)_3$/C electrodes; the increased performance was attributed to an overall structural stabilisation and retardation of V dissolution over progressive electrochemical cycling [489]. Xun and co-workers [488] prepared $Li_3V_2(PO_4)_3$ powders modified with a <5 nm $Li_4P_2O_7$ coating by an off-stoichiometric reaction between Li_2CO_3, $NH_4H_2PO_4$ (in 5% molar excess) and V_2O_3. In a similar fashion to Ceder et al. [377], the $Li_4P_2O_7$ coatings led to enhanced rate performance and stability as a result of increases in Li^+ diffusion and additionally in this case, through a reduction in debilitating side-reactions at potentials >4.0 V [488]. The management of capacity fade as a result of unwanted interaction with electrolyte at higher potential regions is currently of great importance if full utilisation of $Li_3V_2(PO_4)_3$ is to be achieved.

2.3 Transition metal silicates (Li_2MSiO_4)

A new family of cathode materials have been presented recently based on the tetrahedral orthosilicates which, theoretically, are capable of a two electron intercalation process involving the $M^{4+/3+}$ and $M^{3+/2+}$ redox couples [492,493]. The dual-electron process may therefore yield cathodes with capacities exceeding 300 mA h g^{-1}, while the relative strength of the Si-O bond may impart a necessary structural stability. Fe, Mn or Co have

typically been utilised, with more attention recently devoted to Li_2FeSiO_4 structures, due in part to reasons of safety and cost. The structure of Li_2FeSiO_4 has been a focus of a number of recent studies owing to its rich display of polymorphism [494–499], where a number of different polymorphs, designated as β_I, β_{II}, γ_0, γ_{II} and γ_s (see Fig. 35), have been identified and account for an experimental variation in the electrochemical performance of Li_2FeSiO_4 cathodes [498–500].

Li_2FeSiO_4, as with other polyanion cathodes, are poor electronic conductors leading to the utilisation of particle size reduction combined with carbon-coating or carbon composite formation to enhance Li-ion performance [501–511]. Reversible intercalation has only been entertained for one of two Li^+ ions per formula unit in Li_2FeSiO_4, resulting in cells whose experimental capacities fall in the region of ~130–160 mA h g^{-1}.

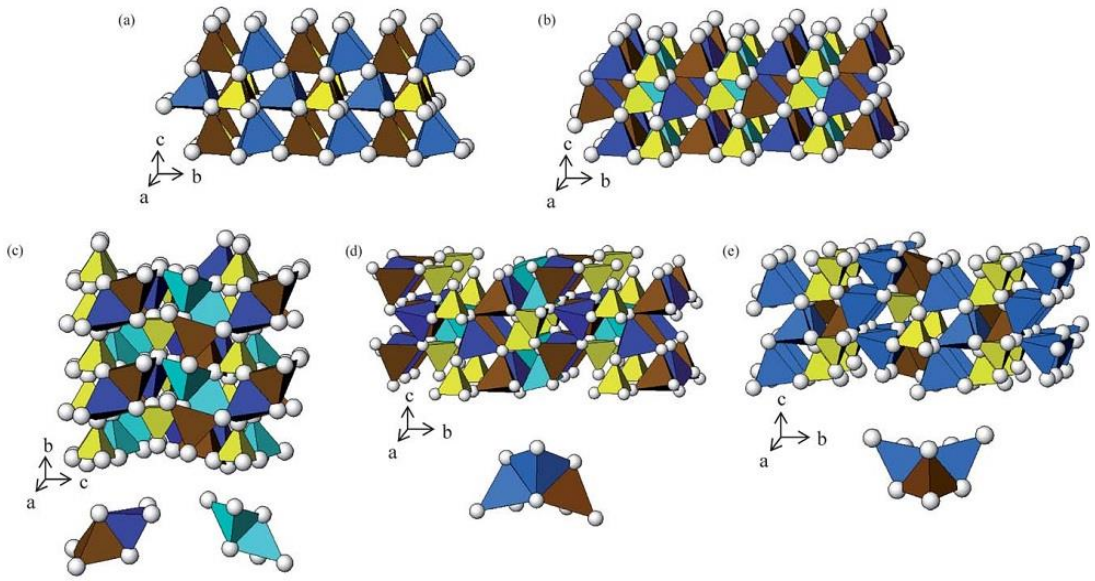

Figure 35 The known polymorphs of Li_2FeSiO_4; (a) β_{II}, where corner-sharing tetrahedra align in one direction with LiO_4 chains running along the a-axis parallel to alternating FeO_4 and SiO_4 units, (b) β_I, corner-sharing tetrahedra aligning in one direction and chains of alternating LiO_4 and FeO_4 units positioned along the a-axis and parallel to alternating FeO_4 and SiO_4 units, (c) γ_s, half of tetrahedra are in opposite directions with pairs of LiO_4/FeO_4 and LiO_4/LiO_4 edge-sharing tetrahedra (shown underneath), (d) γ_0, grouping of three tetrahedra units with the outer two units positioned in the same direction. The sequencing is Li-Li-M (shown underneath) and (e) γ_{II}, akin to structure (d) however, the sequencing involves Li-M-Li (shown underneath). Colours: yellow (SiO_4), brown (FeO_4), blue (LiO_4). The two blue shades represent distinct Li sites. Reproduced with permission from [492]. Copyright 2011 American Chemical Society.

Rangappa et al. [512], however, have recently demonstrated the first cycling of two Li^+ ions in Li_2MSiO_4 electrodes (M = Fe, Mn), at elevated temperature through a supercritical fluid preparation of 2D Li_2MSiO_4 nanoplates. Li_2FeSiO_4 nanoplates were synthesised by adding an aqueous solution of LiOH and ascorbic acid to $FeCl_2{\cdot}4H_2O$ and TEOS dissolved in ethanol. Supercritical fluid (SCF) conditions were attained by heating the prepared solution in a high-pressure cell at 350–420 °C under a pressure of 38 MPa for 4–10 min. The highly crystalline Li_2FeSiO_4 nanoplates were subsequently combined with a conducting polymer (poly(3,4-ethylenedioxythiophene), PEDOT) and MWCNTs by a ball-milling process to improve

the electronic conductivity. The SCF approach, which results in suitable reaction media having both properties of a gas and liquid, has been utilised previously in the preparation of other nanostructures (particularly 1D semiconductors), but has been a relatively uncommon approach thus far in the synthesis of battery materials. The Li_2FeSiO_4 nanosheet composite electrodes displayed predictable capacities of ~160 mA h g^{-1} under room temperature at the rate of C/50, which is in line with a one Li^+ mechanism; however, on testing at elevated temperature (45 ± 5 °C), the Li_2FeSiO_4 composite delivered up to 340 mA h g^{-1} representing near-complete two electron cycling. Similar voltage curves (Fig. 36), were obtained between the first and second discharge cycles which would indicate that no major structural change occurred following the initial charge. Such changes are a dominant feature of Li_2FeSiO_4 electrodes, where stable cycling is only achieved after cation rearrangement to a stable phase and have been outlined in various reports [498,500]. XRD studies of cycled cells revealed that structural change occurred after the first charge cycle leading to the formation of a new, seemingly metastable phase. This newly formed phase remained unchanged over subsequent cycles until a further phase developed which was characterised by the loss of all diffraction peaks and addition of a single peak at 2θ = 44°. The formation of the new phase, occurring after 20 charge discharge cycles, was accompanied by a rapid decline in electrochemical performance. While this example has demonstrated the first reversible cycling of two Li^+ ions in Li_2FeSiO_4 electrodes, further work is needed to elucidate the nature of such transitions in order to attain stable, long-term cycling. Currently, it appears that Li_2FeSiO_4 may remain a single Li^+ host which may require a move toward other cathodes with higher capacity and increased rate capability.

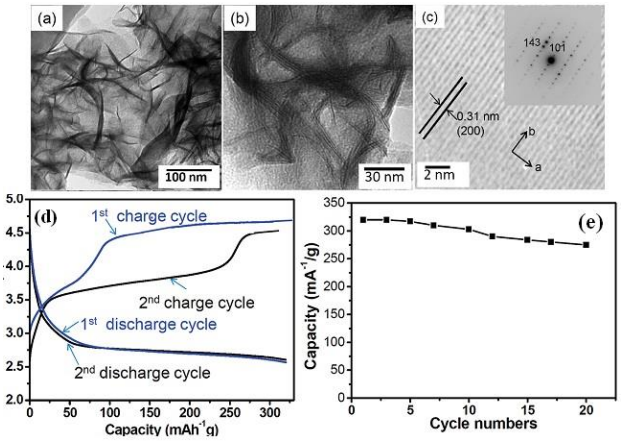

Figure 36 (a, b and c) TEM images of Li_2FeSiO_4 nanoplates prepared by SCF method, (d) voltage curves of the Li_2FeSiO_4 nanoplates at a rate of C/50 and temperature of 45 °C and (e) cycling performance of the Li_2FeSiO_4 nanoplates. Adapted with permission from [512]. Copyright 2012 American Chemical Society

3. Summary and outlook

Our dependency on Li-ion and emerging alternatives in the coming years will no doubt require further enhancements in the performance of existing anode and cathode materials, their architectures and the properties of good electrolytes that are thermodynamically stable at the operation voltage. The development of large-scale Li-ion batteries, particularly for applications such as EV/HEVs, will likely facilitate interest in the drive for electrodes with higher power density, excellent rate capability and cycle life and importantly, safety characteristics which underpin their use, particularly at extremes of operating temperature. Li-ion battery research has seen a second resurgence in academic and industrial development since the oil crisis of the late seventies, owing primarily to the projected need for a reduction in CO_2 emissions which is hoped can be alleviated by increasing the density of EVs and related hybrids. The rechargeable battery based on lithium chemistry represents one of the biggest success stories of the research-to-industry models. Importantly, nanostructuring of the active materials has enabled the development of

electrode architectures with many of the requisites to meet the demanding applications for which they are intended, and it is likely through nanostructuring that future generations of Li-ion batteries shall meet the demand that such batteries will generate. One extension of the understanding gleaned from thousands of papers focused almost entirely on the materials issues with Li-ion technologies, is the ability to fashion structures and arrangements of materials that could potentially accommodate larger anions such as Mn^{2+} or Al^{3+}. This approach exploits a higher valence but requires a material that is capable of even more volumetric expansion of its structure with large ionic radius of the intercalating ions. The trade-off is the possibility of multiple electrons per redox event and thus higher energy densities at a given voltage. Such approaches would need minimal battery electrolyte development if the hexafluorophosphate anion salt is used, and options exist for the incorporation of higher voltage-stable ionic liquid based electrolytes. Indeed, monoelectronic charge transfer events can also be found in Na-ion technology, which has benefits of sodium abundance, but limitations arise from material pulverization due to the larger ionic size and a limited number of materials capable of successful, stable and repeatable Na-ion intercalation. In these cases, the nanostructuring of materials is likely to help filter suitable chemistries for their development.

In this review, we have highlighted just some of the advancements which have been made in both anode and cathode nanoarchitectures to meet the challenging goal of better performing, safer and longer life Li-ion batteries. Ultimately, the industry shall likely decide the fate of the prospective design and electrode choice, based on performance, safety and cost in each application. Some expensive materials growth, deposition and formation methods are still required for new materials and battery chemistries especially where knowledge of a very well defined material and its electrochemical response are critical. With high quality growth methods used as a test-bed, routes towards more up-scalable and lower cost alternatives can be developed based on a detailed understanding of new materials. In situ TEM is currently being used to identify the real effect of Li^+ intercalation into new nanomaterials without the complications that are difficult to assess in disordered powders [513–515].

High-performance batteries are now a direct requirement in the change to renewable and sustainable energy applications. The requirement for charge storage modules for new transport means is very important—it is the biggest consumer application requirement yet. With the growing demand for larger-sized Li-ion batteries for automotive and in the future smart grid energy storage applications, the issue of battery safety will continue to present a challenge. The flammability of the conventional organic carbonate solvent based electrolytes remains a key issue. The desire to migrate to an all solid-state system is heightened in these larger battery designs and so one can anticipate that this represents a key area for future material development and hence, an opportunity for new classes of nanoscale materials.

The information derived from the plethora of investigations into nanomaterials performance should help define optimum chemistries, sizes, assemblies, conductivities, structural and electrochemical properties etc., to optimize specific next-generation battery needs and the demanding performance and safety requirements of plug-in hybrid electric vehicles. Advances in modelling have helped greatly in predicting solid solution phases for a range of charge storage technologies, and in particular, Ceder et al. [516], among others, are pioneering a library of alloys, compounds and structures from first principles calculations and density functional theory so that Li insertion potentials, voltage windows and structural response to charging and discharging can be predicted.

Recent approaches are testing the possibility

of enhancing the rate capability (charging and discharging), by using 3D nanoarchitectures of individual nanostructures to improve the packing density of the electrode materials, without unwanted short-circuiting or self-discharge acceleration. In such cases, the active material can be deposited at a thickness close to the Li-ion diffusion length, thereby reducing the limitation of solid-state diffusion. Such approaches typically use photonic crystals, or opal, templates to create inverse opal structures or other 3D forms of assemblies. These materials can also be filled with electrolytes that are liquid or polymer based, forming interpenetrating networks. Recent demonstrations have shown that ultrafast-charging batteries can be fashioned by controlling porosity in active materials [517–521]. The downside is the severe reduction in specific energy due to the porosity, but the technology may prove useful for large surface area applications.

In more recent times, there has been a large resurgence in the research and development of $Li–O_2$ and Li–S chemistries, particularly since such systems offer theoretically vast specific energies, far in excess of their predicted Li-ion equivalents. A number of excellent review articles are available on such systems, to which the reader is referred.[522–527]. It is envisioned that $Li–O_2$ and Li–S chemistries may challenge the dominancy of Li-ion batteries in the future; aqueous and non-aqueous $Li–O_2$ designs, for example, could potentially offer up to ~3500 W h kg^{-1}, an approximately ten-fold increase based on today's $LiCoO_2$/graphite Li-ion cells (~390 W h kg^{-1}), while Li–S designs could offer in the region of 2570 W h kg^{-1}. Although such chemistries have been known for some time, there today still exists obstacles to their prospective use which has led to relatively low levels of commercial uptake thus far. In particular, the use of Li-metal anodes presents challenges to the safety of rechargeable battery designs which must be overcome, while the extended reversible charge storage, particularly relating to that of $Li–O_2$ systems, also remains a feature for improvement. Further research and development shall no doubt bring a greater understanding and appreciation of their chemistries and is indeed necessary to achieve an adequate understanding of their application and cost. In turn, however, $Li–O_2$ and Li–S batteries of the future may offer a viable and necessary alternative to the Li-ion battery, especially for applications requiring greater performance.

It seems likely the next generation of lithium-ion batteries fully based on nanomaterials will soon be here. There is plenty to inspire development in the living world—biofuel cells, high-voltage liquid-electrolyte microbatteries based on processes naturally occurring in electric eels, and battery nanomaterials assembled using viruses and bacteria, have already been demonstrated. The virus-enabled battery design is intriguing: Genetically engineered viruses can first coat themselves with iron phosphate and then knit carbon nanotubes to create a network of highly conductive material. Extensions could be envisaged whereby biological or polymeric species can both assemble materials within a battery, and accommodate the stresses that occur within materials, in addition to maintaining electrical conductivity, and perhaps heal and maintain contact between broken down materials typically found in some Li-ion batteries after many charge-discharge cycles.

In the immediate future, the promise of nanotechnology and nanomaterials will be tested and the likelihood is that next generation high performance rechargeable batteries, even sustainable ones, will have their electrodes designed using nanoscale materials. Advances in $Li–O_2$ designs, Li–S batteries and other systems such as fuel cell technology, may seriously challenge the current dominancy of Li-ion batteries in the 2025–2030 timeframe; however, for the next decade at least, Li-ion batteries remain at the forefront of powering modern consumer devices and in supporting the growing number of electric vehicles on our roads.

Acknowledgements

This work was supported by Science Foundation Ireland (SFI) Grant no. 07/SRC/I1172.

References

[1] Armand, M.; Tarascon, J. Building better batteries. *Nature* **2008**, *451*, 652–657.

[2] Stein, A. Energy storage: Batteries take charge. *Nat. Nanotechnol.* **2011**, *6*, 262–263.

[3] Goodenough, J. B.; Kim, Y. Challenges for rechargeable Li batteries. *Chem. Mater.* **2010**, *22*, 587–603.

[4] Bruce, P. G.; Scrosati, B.; Tarascon, J.-M. Nanomaterials for rechargeable lithium batteries. *Angew. Chem. Int. Edit.* **2008**, *47*, 2930–2946.

[5] Aricò, A.; Bruce, P.; Scrosati, B.; Tarascon, J.; Van, W. Nanostructured materials for advanced energy conversion and storage devices. *Nat. Mater.* **2005**, *4*, 366–377.

[6] Song, M.-K.; Park, S.; Alamgir, F. M.; Cho, J.; Liu, M. Nanostructured electrodes for lithium-ion and lithium-air batteries: The latest developments, challenges, and perspectives. *Mat. Sci. Eng. R* **2011**, *72*, 203–252.

[7] Aricò, A. S.; Bruce, P.; Scrosati, B.; Tarascon, J. M.; van Schalkwijk, W. Nanostructured materials for advanced energy conversion and storage devices. *Nat. Mater.* **2005**, *4*, 366–377.

[8] Etacheri, V.; Marom, R.; Elazari, R.; Salitra, G.; Aurbach, D. Challenges in the development of advanced Li-ion batteries: a review. *Energy Environ. Sci.* **2011**, *4*, 3243–3262.

[9] Tiwari, J. N.; Tiwari, R. N.; Kim, K. S. Zero-dimensional, one-dimensional, two-dimensional and three-dimensional nanostructured materials for advanced electrochemical energy devices. *Prog. Mater. Sci.* **2012**, *57*, 724–803.

[10] Szczech, J. R.; Jin, S. Nanostructured silicon for high capacity lithium battery anodes. *Energy Environ. Sci.* **2011**, *4*, 56–72.

[11] Kasavajjula, U.; Wang, C.; Appleby, A. J. Nano-and bulk-silicon-based insertion anodes for lithium-ion secondary cells. *J. Power Sources* **2007**, *163*, 1003–1039.

[12] Chan, C. K.; Ruffo, R.; Hong, S. S.; Huggins, R. a.; Cui, Y. Structural and electrochemical study of the reaction of lithium with silicon nanowires. *J. Power Sources* **2009**, *189*, 34–39.

[13] Li, J.; Dahn, J. R. An in situ X-ray diffraction study of the reaction of Li with crystalline Si. *J. Electrochem. Soc.* **2007**, *154*, A156–A161.

[14] Kang, Y.-M.; Lee, S.-M.; Kim, S.-J.; Jeong, G.-J.; Sung, M.-S.; Choi, W.-U.; Kim, S.-S. Phase transitions explanatory of the electrochemical degradation mechanism of Si based materials. *Electrochem. Commun.* **2007**, *9*, 959–964.

[15] Beattie, S. D.; Larcher, D.; Morcrette, M.; Simon, B.; Tarascon, J.-M. Si electrodes for Li-ion batteries—a new way to look at an old problem. *J. Electrochem. Soc.* **2008**, *155*, A158–A163.

[16] Liu, X. H.; Zheng, H.; Zhong, L.; Huang, S.; Karki, K.; Zhang, L. Q.; Liu, Y.; Kushima, A.; Liang, W. T.; Wang, J. W. et al. Anisotropic swelling and fracture of silicon nanowires during lithiation. *Nano Lett.* **2011**, *11*, 3312–3318.

[17] Zhang, Q.; Zhang, W.; Wan, W.; Cui, Y.; Wang, E. Lithium insertion in silicon nanowires: An ab initio study. *Nano Lett.* **2010**, *10*, 3243–3249.

[18] Sethuraman, V. a.; Chon, M. J.; Shimshak, M.; Srinivasan, V.; Guduru, P. R. In situ measurements of stress evolution in silicon thin films during electrochemical lithiation and delithiation. *J. Power Sources* **2010**, *195*, 5062–5066.

[19] Barth, S.; Hernandez-Ramirez, F.; Holmes, J. D.; Romano-Rodriguez, A. Synthesis and applications of one-dimensional semiconductors. *Prog. Mater. Sci.* **2010**, *55*, 563–627.

[20] Green, M.; Fielder, E.; Scrosati, B.; Wachtler, M.; Moreno, J. S. Structured silicon anodes for lithium battery applications. *Electrochem. Solid-State Lett.* **2003**, *6*, A75–A79.

[21] Yang, H.; Huang, S.; Huang, X.; Fan, F.; Liang, W.; Liu, X. H.; Chen, L.-Q.; Huang, J. Y.; Li, J.; Zhu, T.; Zhang, S. Orientation-dependent interfacial mobility governs the anisotropic swelling in lithiated silicon nanowires. *Nano Lett.* **2012**, *12*, 1953–1958.

[22] Chan, C. K.; Peng, H.; Liu, G.; McIlwrath, K.; Zhang, X. F.; Huggins, R. A; Cui, Y. High-performance lithium battery anodes using silicon nanowires. *Nat. Nanotechnol.* **2008**, *3*, 31–35.

[23] Laik, B.; Eude, L.; Pereiraramos, J.; Cojocaru, C.; Pribat, D.; Rouviere, E. Silicon nanowires as negative electrode for lithium-ion microbatteries. *Electrochim. Acta* **2008**, *53*, 5528–5532.

[24] Kang, K.; Lee, H.-S.; Han, D.-W.; Kim, G.-S.; Lee, D.; Lee, G.; Kang, Y.-M.; Jo, M.-H. Maximum Li storage in Si nanowires for the high capacity three-dimensional Li-ion battery. *Appl. Phys. Lett.* **2010**, *96*, 053110.

[25] Ruffo, R.; Hong, S. S.; Chan, C. K.; Huggins, R. a.; Cui, Y. Impedance analysis of silicon nanowire lithium ion battery anodes. *J. Phys. Chem. C* **2009**, *113*, 11390–11398.

[26] Peng, K.; Jie, J.; Zhang, W.; Lee, S.-T. Silicon nanowires for rechargeable lithium-ion battery anodes. *Appl. Phys. Lett.* **2008**, *93*, 033105.

[27] Nguyen, H. T.; Yao, F.; Zamfir, M. R.; Biswas, C.; So, K. P.; Lee, Y. H.; Kim, S. M.; Cha, S. N.; Kim, J. M.; Pribat, D. Highly interconnected Si nanowires for improved stability Li-ion battery anodes. *Adv. Energy Mater.* **2011**, *1*, 1154–1161.

[28] Loveridge, M.; Lain, M.; Liu, F.; Coowar, F.; Macklin, B.; Green, M. High performance silicon anode materials for next generation lithium ion batteries. *Abstract #12 The 15th International Meeting on Lithium Batteries. The Electrochemical Society* **2010**.

[29] Liu, F.; Lain, M.; Loveridge, M.; Coowar, F.; Macklin, B.; Green, M. Low cost silicon fibres For lithium ion batteries. *Abstract #47 The 15th International Meeting on Lithium Batteries. The Electrochemical Society* **2010**.

[30] Huang, R.; Fan, X.; Shen, W.; Zhu, J. Carbon-coated silicon nanowire array films for high-performance lithium-ion battery anodes. *Appl. Phys. Lett.* **2009**, *95*, 133119.

[31] Ji, L.; Zhang, X. Fabrication of porous carbon/Si composite nanofibers as high-capacity battery electrodes. *Electrochem. Commun.* **2009**, *11*, 1146–1149.

[32] Kim, H.; Cho, J. Superior lithium electroactive mesoporous Si@carbon core–shell nanowires for lithium battery anode material. *Nano Lett.* **2008**, *8*, 3688–3691.

[33] Chan, C. K.; Patel, R. N.; O'Connell, M. J.; Korgel, B. A; Cui, Y. Solution-grown silicon nanowires for lithium-ion battery anodes. *ACS Nano* **2010**, *4*, 1443–1450.

[34] Cui, L.-F.; Ruffo, R.; Chan, C. K.; Peng, H.; Cui, Y. Crystalline-amorphous core–shell silicon nanowires for high capacity and high current battery electrodes. *Nano Lett.* **2009**, *9*, 491–495.

[35] Yao, Y.; Liu, N.; McDowell, M. T.; Pasta, M.; Cui, Y. Improving the cycling stability of silicon nanowire anodes with conducting polymer coatings. *Energy Environ. Sci.* **2012**, *5*, 7927–7930.

[36] McDowell, M. T.; Lee, S. W.; Ryu, I.; Wu, H.; Nix, W. D.; Choi, J. W.; Cui, Y. Novel size and surface oxide effects in silicon nanowires as lithium battery anodes. *Nano Lett.* **2011**, *11*, 4018–4025.

[37] Ge, M.; Rong, J.; Fang, X.; Zhou, C. Porous doped silicon nanowires for lithium ion battery anode with long cycle life. *Nano Lett.* **2012**, *12*, 2318–2323.

[38] Park, M.-H.; Kim, M. G.; Joo, J.; Kim, K.; Kim, J.; Ahn, S.; Cui, Y.; Cho, J. Silicon nanotube battery anodes. *Nano Lett.* **2009**, *9*, 3844–3847.

[39] Song, T.; Xia, J.; Lee, J.-H.; Lee, D. H.; Kwon, M.-S.; Choi, J.-M.; Wu, J.; Doo, S. K.; Chang, H.; Park, W. Il et al. Arrays of sealed silicon nanotubes as anodes for lithium ion batteries. *Nano Lett.* **2010**, *10*, 1710–1716.

[40] Kim, H.; Seo, M.; Park, M.-H.; Cho, J. A critical size of silicon nano-anodes for lithium rechargeable batteries. *Angew. Chem. Int. Edit.* **2010**, *49*, 2146–2149.

[41] Ma, H.; Cheng, F.; Chen, J.-Y.; Zhao, J.-Z.; Li, C.-S.; Tao, Z.-L.; Liang, J. Nest-like silicon nanospheres for high-capacity lithium storage. *Adv. Mater.* **2007**, *19*, 4067–4070.

[42] Yao, Y.; McDowell, M. T.; Ryu, I.; Wu, H.; Liu, N.; Hu, L.; Nix, W. D.; Cui, Y. Interconnected silicon hollow nanospheres for lithium-ion battery anodes with long cycle life. *Nano Lett.* **2011**, *11*, 2949–2954.

[43] Chou, S.-L.; Wang, J.-Z.; Choucair, M.; Liu, H.-K.; Stride, J. A.; Dou, S.-X. Enhanced reversible lithium storage in a nanosize silicon/graphene composite. *Electrochem. Commun.* **2010**, *12*, 303–306.

[44] Magasinski, a; Dixon, P.; Hertzberg, B.; Kvit, A.; Ayala, J.; Yushin, G. High-performance lithium-ion anodes using a hierarchical bottom-up approach. *Nat. Mater.* **2010**, *9*, 353–358.

[45] Ding, N.; Xu, J.; Yao, Y.; Wegner, G.; Lieberwirth, I.; Chen, C. Improvement of cyclability of Si as anode for Li-ion batteries. *J. Power Sources* **2009**, *192*, 644–651.

[46] Lee, J. K.; Smith, K. B.; Hayner, C. M.; Kung, H. H. Silicon nanoparticles-graphene paper composites for Li ion battery anodes. *Chem. Commun.* **2010**, *46*, 2025–2027.

[47] Hu, Y.-S.; Demir-Cakan, R.; Titirici, M.-M.; Müller, J.-O.; Schlögl, R.; Antonietti, M.; Maier, J. Superior storage performance of a Si@SiO_x/C nanocomposite as anode material for lithium-ion batteries. *Angew. Chem. Int. Edit.* **2008**, *47*, 1645–1649.

[48] Wang, W.; Kumta, P. N. Nanostructured hybrid silicon/carbon nanotube heterostructures: Reversible high-capacity lithium-ion anodes. *ACS Nano* **2010**, *4*, 2233–2241.

[49] Kim, H.; Han, B.; Choo, J.; Cho, J. Three-dimensional porous silicon particles for use in high-performance lithium secondary batteries. *Angew. Chem. Int. Edit.* **2008**, *47*, 10151–10154.

[50] Zheng, Y.; Yang, J.; Wang, J.; NuLi, Y. Nano-porous Si/C composites for anode material of lithium-ion batteries. *Electrochim. Acta* **2007**, *52*, 5863–5867.

[51] Jiang, T.; Zhang, S.; Qiu, X.; Zhu, W.; Chen, L. Preparation and characterization of silicon-based three-dimensional cellular anode for lithium ion battery. *Electrochem. Commun.* **2007**, *9*, 930–934.

[52] Kovalenko, I.; Zdyrko, B.; Magasinski, A.; Hertzberg, B.; Milicev, Z.; Burtovyy, R.; Luzinov, I.; Yushin, G. A major constituent of brown algae for use in high-capacity Li-ion batteries. *Science* **2011**, *334*, 75–79.

[53] Chan, C. K.; Zhang, X. F.; Cui, Y. High capacity Li ion battery anodes using ge nanowires. *Nano Lett.* **2008**, *8*, 307–309.

[54] Graetz, J.; Ahn, C. C.; Yazami, R.; Fultz, B. Nanocrystalline and thin film germanium electrodes with high lithium capacity and high rate capabilities. *J. Electrochem. Soc.* **2004**, *151*, A698–A702.

[55] Laforge, B.; Levan-Jodin, L.; Salot, R.; Billard, A. Study of germanium as electrode in thin-film battery. *J. Electrochem. Soc.* **2008**, *155*, A181–A188.

[56] Liu, X. H.; Huang, S.; Picraux, S. T.; Li, J.; Zhu, T.; Huang, J. Y. Reversible nanopore formation in Ge nanowires during lithiation–delithiation cycling: An in situ transmission electron microscopy study. *Nano Lett.* **2011**, *11*, 3991–3997.

[57] Tan, L. P.; Lu, Z.; Tan, H. T.; Zhu, J.; Rui, X.; Yan, Q.; Hng, H. H. Germanium nanowires-based carbon composite as anodes for lithium-ion batteries. *J. Power Sources* **2012**, *206*, 253–258.

[58] Yoon, S.; Park, C.-M.; Sohn, H.-J. Electrochemical characterizations of germanium and carbon-coated germanium composite anode for lithium-ion batteries. *Electrochem. Solid-State Lett.* **2008**, *11*, A42–A45.

[59] Ko, Y.-D.; Kang, J.-G.; Lee, G.-H.; Park, J.-G.; Park, K.-S.; Jin, Y.-H.; Kim, D.-W. Sn-induced low-temperature growth of Ge nanowire electrodes with a large lithium storage capacity. *Nanoscale* **2011**, *3*, 3371–3375.

[60] Collins, G.; Holmes, J. D. Chemical functionalisation of silicon and germanium nanowires. *J. Mater. Chem.* **2011**, *21*, 11052–11069.

[61] Seo, M.-H.; Park, M.; Lee, K. T.; Kim, K.; Kim, J.; Cho, J. High performance Ge nanowire anode sheathed with carbon for lithium rechargeable batteries. *Energy Environ. Sci.* **2011**, *4*, 425–428.

[62] DiLeo, R. A.; Ganter, M. J.; Landi, B. J.; Raffaelle, R. P. Germanium–single-wall carbon nanotube anodes for lithium ion batteries. *J. Mater. Res.* **2011**, *25*, 1441–1446.

[63] Cui, G.; Gu, L.; Kaskhedikar, N.; van Aken, P. a.; Maier, J. A novel germanium/carbon nanotubes nanocomposite for lithium storage material. *Electrochim. Acta* **2010**, *55*, 985–988.

[64] Song, T.; Cheng, H.; Choi, H.; Lee, J. Si/Ge Double layered nanotube array as lithium ion battery anode. *ACS Nano* **2012**, *6*, 303–309.

[65] Park, M.-H.; Cho, Y.; Kim, K.; Kim, J.; Liu, M.; Cho, J. Germanium nanotubes prepared by using the Kirkendall effect as anodes for high-rate lithium batteries. *Angew. Chem. Int. Edit.* **2011**, *50*, 9647–9650.

[66] Park, M.-H.; Kim, K.; Kim, J.; Cho, J. Flexible dimensional control of high-capacity Li-ion-battery anodes: from 0D hollow to 3D porous germanium nanoparticle assemblies. *Adv. Mater.* **2010**, *22*, 415–418.

[67] Seng, K. H.; Park, M.-H.; Guo, Z. P.; Liu, H. K.; Cho, J. Self-assembled germanium/carbon nanostructures as high-power anode material for the lithium-ion battery. *Angew. Chem. Int. Edit.* **2012**, *51*, 5657–5661.

[68] Yang, L. C.; Gao, Q. S.; Li, L.; Tang, Y.; Wu, Y. P. Mesoporous germanium as anode material of high capacity and good cycling prepared by a mechanochemical reaction. *Electrochem. Commun.* **2010**, *12*, 418–421.

[69] Wang, X.-L.; Han, W.-Q.; Chen, H.; Bai, J.; Tyson, T. A.; Yu, X.-Q.; Wang, X.-J.; Yang, X.-Q. Amorphous hierarchical porous GeO_x as high-capacity anodes for Li ion batteries with very long cycling life. *J. Am. Chem. Soc.* **2011**, *133*, 20692–20695.

[70] Deng, D.; Kim, M. G.; Lee, J. Y.; Cho, J. Green energy storage materials: Nanostructured TiO_2 and Sn-based anodes for lithium-ion batteries. *Energy Environ. Sci.* **2009**, *2*, 818–837

[71] Wu, H. Bin; Chen, J. S.; Hng, H. H.; Lou, X. W. D. Nanostructured metal oxide-based materials as advanced anodes for lithium-ion batteries. *Nanoscale* **2012**, *4*, 2526–2542.

[72] Wang, Z.; Zhou, L.; David Lou, X. W. Metal oxide hollow nanostructures for lithium-ion batteries. *Adv. Mater.* **2012**, *24*, 1903–1911.

[73] Bazin, L.; Mitra, S.; Taberna, P. L.; Poizot, P.; Gressier, M.; Menu, M. J.; Barnabé, A.; Simon, P.; Tarascon, J.-M. High rate capability pure Sn-based nano-architectured electrode assembly for rechargeable lithium batteries. *J. Power Sources* **2009**, *188*, 578–582.

[74] Huang, J. Y.; Zhong, L.; Wang, C. M.; Sullivan, J. P.; Xu, W.; Zhang, L. Q.; Mao, S. X.; Hudak, N. S.; Liu, X. H.; Subramanian, A. et al. In situ observation of the electrochemical lithiation of a single SnO_2 nanowire electrode. *Science* **2010**, *330*, 1515–1520.

[75] Ko, Y.-D.; Kang, J.-G.; Park, J.-G.; Lee, S.; Kim, D.-W. Self-supported SnO_2 nanowire electrodes for high-power lithium-ion batteries. *Nanotechnology* **2009**, *20*, 455701.

[76] Meduri, P.; Pendyala, C.; Kumar, V.; Sumanasekera, G. U.; Sunkara, M. K. Hybrid tin oxide nanowires as stable and high capacity anodes for Li-ion batteries. *Nano Lett.* **2009**, *9*, 612–616.

[77] Park, M.-S.; Kang, Y.-M.; Wang, G.-X.; Dou, S.-X.; Liu, H.-K. The effect of morphological modification on the electrochemical properties of SnO_2 nanomaterials. *Adv. Funct. Mater.* **2008**, *18*, 455–461.

[78] Liu, J.; Li, Y.; Huang, X.; Ding, R.; Hu, Y.; Jiang, J.; Liao, L. Direct growth of SnO_2 nanorod array electrodes for lithium-ion batteries. *J. Mater. Chem.* **2009**, *19*, 1859–1864.

[79] Lou, X. W.; Li, C. M.; Archer, L. A. Designed synthesis of coaxial SnO_2@carbon hollow nanospheres for highly reversible lithium storage. *Adv. Mater.* **2009**, *21*, 2536–2539.

[80] Chou, S.-L.; Wang, J.-Z.; Zhong, C.; Rahman, M. M.; Liu, H.-K.; Dou, S.-X. A facile route to carbon-coated SnO_2 nanoparticles combined with a new binder for enhanced cyclability of Li-ion rechargeable batteries. *Electrochim. Acta* **2009**, *54*, 7519–7524.

[81] Lou, X.; Deng, D. Preparation of SnO_2/carbon composite hollow spheres and their lithium storage properties. *Chem. Mater.* **2008**, 6562–6566.

[82] Qiao, H.; Zheng, Z.; Zhang, L.; Xiao, L. SnO_2@C core–shell spheres: Synthesis, characterization, and performance in reversible Li-ion storage. *J. Mater. Sci.* **2008**, *43*, 2778–2784.

[83] Liu, J.; Li, W.; Manthiram, A. Dense core–shell structured SnO_2/C composites as high performance anodes for lithium ion batteries. *Chem. Commun.* **2010**, *46*, 1437–1439.

[84] Chen, J.; Cheah, Y. SnO_2 nanoparticles with controlled carbon nanocoating as high-capacity anode materials for lithium-ion batteries. *J. Phys. Chem. C* **2009**, 20504–20508.

[85] Derrien, G.; Hassoun, J.; Panero, S.; Scrosati, B. Nanostructured Sn–C composite as an advanced anode material in high-performance lithium-ion batteries. *Adv. Mater.* **2007**, *19*, 2336–2340.

[86] Hassoun, J.; Derrien, G.; Panero, S.; Scrosati, B. A Nanostructured Sn–C composite lithium battery electrode with unique stability and high electrochemical performance. *Adv. Mater.* **2008**, *20*, 3169–3175.

[87] Yu, Y.; Gu, L.; Wang, C.; Dhanabalan, A.; van Aken, P. A.; Maier, J. Encapsulation of Sn@carbon nanoparticles in bamboo-like hollow carbon nanofibers as an anode material in lithium-based batteries. *Angew. Chem. Int. Edit.* **2009**, *48*, 6485–6489.

[88] Wang, G.; Wang, B.; Wang, X.; Park, J.; Dou, S.; Ahn, H.; Kim, K. Sn/graphene nanocomposite with 3D architecture for enhanced reversible lithium storage in lithium ion batteries. *J. Mater. Chem.* **2009**, *19*, 8378–8384.

[89] Yao, J.; Shen, X.; Wang, B.; Liu, H.; Wang, G. In situ chemical synthesis of SnO_2–graphene nanocomposite as anode materials for lithium-ion batteries. *Electrochem. Commun.* **2009**, *11*, 1849–1852.

[90] Du, Z.; Yin, X.; Zhang, M.; Hao, Q.; Wang, Y.; Wang, T. In situ synthesis of SnO_2/graphene nanocomposite and their application as anode material for lithium ion battery. *Mater. Lett.* **2010**, *64*, 2076–2079.

[91] Wang, X.; Zhou, X.; Yao, K.; Zhang, J.; Liu, Z. A SnO_2/graphene composite as a high stability electrode for lithium ion batteries. *Carbon* **2011**, *49*, 133–139.

[92] Kim, H.; Kim, S.-W.; Park, Y.-U.; Gwon, H.; Seo, D.-H.; Kim, Y.; Kang, K. SnO_2/graphene composite with high lithium storage capability for lithium rechargeable batteries. *Nano Res.* **2010**, *3*, 813–821.

[93] Demir-Cakan, R.; Hu, Y. Facile one-pot synthesis of mesoporous SnO_2 microspheres via nanoparticles assembly and lithium storage properties. *Chem. Mater.* **2008**, 1227–1229.

[94] Guo, Z. P.; Du, G. D.; Nuli, Y.; Hassan, M. F.; Liu, H. K. Ultra-fine porous SnO_2 nanopowder prepared via a molten salt process: A highly efficient anode material for lithium-ion batteries. *J. Mater. Chem.* **2009**, *19*, 3253–3257.

[95] Li, L.; Yin, X.; Liu, S.; Wang, Y.; Chen, L.; Wang, T. Electrospun porous SnO_2 nanotubes as high capacity anode materials for lithium ion batteries. *Electrochem. Commun.* **2010**, *12*, 1383–1386.

[96] Ning, J.; Dai, Q.; Jiang, T.; Men, K.; Liu, D.; Xiao, N.; Li, C.; Li, D.; Liu, B.; Zou, B. et al. Facile synthesis of tin oxide nanoflowers: A potential high-capacity lithium-ion-storage material. *Langmuir* **2009**, *25*, 1818–1821.

[97] Yin, X.; Li, C.; Zhang, M. One-step synthesis of hierarchical SnO_2 hollow nanostructures via self-assembly for high power lithium ion batteries. *J. Phys. Chem. C* **2010**, 8084–8088.

[98] Ferguson, P. P.; Todd, A. D. W.; Dahn, J. R. Comparison of mechanically alloyed and sputtered tin–cobalt–carbon as an anode material for lithium-ion batteries. *Electrochem. Commun.* **2008**, *10*, 25–31.

[99] Ferguson, P. P.; Martine, M. L.; George, A. E.; Dahn, J. R. Studies of tin–transition metal–carbon and tin–cobalt–transition metal–carbon negative electrode materials prepared by mechanical attrition. *J. Power Sources* **2009**, *194*, 794–800.

[100] Chen, Z.; Qian, J.; Ai, X.; Cao, Y.; Yang, H. Preparation and electrochemical performance of Sn–Co–C composite as anode material for Li-ion batteries. *J. Power Sources* **2009**, *189*, 730–732.

[101] Hassoun, J.; Panero, S.; Mulas, G.; Scrosati, B. An electrochemical investigation of a Sn–Co–C ternary alloy as a negative electrode in Li-ion batteries. *J. Power Sources* **2007**, *171*, 928–931.

[102] Guo, H.; Zhao, H.; Jia, X. Spherical Sn–Ni–C alloy anode material with submicro/micro complex particle structure for lithium secondary batteries. *Electrochem. Commun.* **2007**, *9*, 2207–2211.

[103] Ke, F.-S.; Huang, L.; Cai, J.-S.; Sun, S.-G. Electroplating synthesis and electrochemical properties of macroporous Sn–Cu alloy electrode for lithium-ion batteries. *Electrochim. Acta* **2007**, *52*, 6741–6747.

[104] Zhu, G.-N.; Wang, Y.-G.; Xia, Y.-Y. Ti-based compounds as anode materials for Li-ion batteries. *Energy Environ. Sci.* **2012**, *5*, 6652–6667.

[105] Amine, K.; Belharouak, I.; Chen, Z.; Tran, T.; Yumoto, H.; Ota, N.; Myung, S.-T.; Sun, Y.-K. Nanostructured anode material for high-power battery system in electric vehicles. *Adv. Mater.* **2010**, *22*, 3052–3057.

[106] Lu, X.; Zhao, L.; He, X.; Xiao, R.; Gu, L.; Hu, Y.-S.; Li, H.; Wang, Z.; Duan, X.; Chen, L.; Maier, J.; Ikuhara, Y. Lithium storage in $Li_4Ti_5O_{12}$ spinel: the full static picture from electron microscopy. *Adv. Mater.* **2012**, *24*, 3233–3238.

[107] Zhu, G.-N.; Liu, H.-J.; Zhuang, J.-H.; Wang, C.-X.; Wang, Y.-G.; Xia, Y.-Y. Carbon-coated nano-sized $Li_4Ti_5O_{12}$ nanoporous micro-sphere as anode material for high-rate lithium-ion batteries. *Energy Environ. Sci.* **2011**, *4*, 4016–4022.

[108] Jung, H.-G.; Myung, S.-T.; Yoon, C. S.; Son, S.-B.; Oh, K. H.; Amine, K.; Scrosati, B.; Sun, Y.-K. Microscale spherical carbon-coated $Li_4Ti_5O_{12}$ as ultra high power anode material for lithium batteries. *Energy Environ. Sci.* **2011**, *4*, 1345–1351.

[109] Yu, H.; Zhang, X.; Jalbout, A. F.; Yan, X.; Pan, X.; Xie, H.; Wang, R. High-rate characteristics of novel anode $Li_4Ti_5O_{12}$/polyacene materials for Li-ion secondary batteries. *Electrochim. Acta* **2008**, *53*, 4200–4204.

[110] Cheng, L.; Yan, J.; Zhu, G.-N.; Luo, J.-Y.; Wang, C.-X.; Xia, Y.-Y. General synthesis of carbon-coated nanostructure $Li_4Ti_5O_{12}$ as a high rate electrode material for Li-ion intercalation. *J. Mater. Chem.* **2010**, *20*, 595–602.

[111] Wang, G. J.; Gao, J.; Fu, L. J.; Zhao, N. H.; Wu, Y. P.; Takamura, T. Preparation and characteristic of carbon-coated $Li_4Ti_5O_{12}$ anode material. *J. Power Sources* **2007**, *174*, 1109–1112.

[112] Yuan, T.; Yu, X.; Cai, R.; Zhou, Y.; Shao, Z. Synthesis of pristine and carbon-coated $Li_4Ti_5O_{12}$ and their low-temperature electrochemical performance. *J. Power Sources* **2010**, *195*, 4997–5004.

[113] Cheng, L.; Li, X.-L.; Liu, H.-J.; Xiong, H.-M.; Zhang, P.-W.; Xia, Y.-Y. Carbon-coated $Li_4Ti_5O_{12}$ as a high rate electrode material for Li-ion intercalation. *J. Electrochem. Soc.* **2007**, *154*, A692–A697.

[114] Liu, H.; Feng, Y.; Wang, K.; Xie, J. Synthesis and electrochemical properties of $Li_4Ti_5O_{12}$/C composite by the PVB rheological phase method. *J. Phys. Chem. Solids* **2008**, *69*, 2037–2040.

[115] Gao, J.; Ying, J.; Jiang, C.; Wan, C. High-density spherical $Li_4Ti_5O_{12}$/C anode material with good rate capability for lithium ion batteries. *J. Power Sources* **2007**, *166*, 255–259.

[116] Zhu, N.; Liu, W.; Xue, M.; Xie, Z.; Zhao, D.; Zhang, M.; Chen, J.; Cao, T. Graphene as a conductive additive to enhance the high-rate capabilities of electrospun $Li_4Ti_5O_{12}$ for lithium-ion batteries. *Electrochim. Acta* **2010**, *55*, 5813–5818.

[117] Shen, L.; Yuan, C.; Luo, H.; Zhang, X.; Yang, S.; Lu, X. In situ synthesis of high-loading $Li_4Ti_5O_{12}$–graphene hybrid nanostructures for high rate lithium ion batteries. *Nanoscale* **2011**, *3*, 572–574.

[118] Hao, Y.-J.; Lai, Q.-Y.; Lu, J.-Z.; Ji, X.-Y. Effects of dopant on the electrochemical properties of $Li_4Ti_5O_{12}$ anode materials. *Ionics* **2007**, *13*, 369–373.

[119] Huang, S.; Wen, Z.; Zhu, X.; Lin, Z. Effects of dopant on the electrochemical performance of $Li_4Ti_5O_{12}$ as electrode material for lithium ion batteries. *J. Power Sources* **2007**, *165*, 408–412.

[120] Wolfenstine, J.; Allen, J. L. Electrical conductivity and charge compensation in Ta doped $Li_4Ti_5O_{12}$. *J. Power Sources* **2008**, *180*, 582–585.

[121] Qi, Y.; Huang, Y.; Jia, D.; Bao, S.-J.; Guo, Z. P. Preparation and characterization of novel spinel $Li_4Ti_5O_{12-x}Br_x$ anode materials. *Electrochim. Acta* **2009**, *54*, 4772–4776.

[122] Wang, Y.-Q.; Gu, L.; Guo, Y.-G.; Li, H.; He, X.-Q.; Tsukimoto, S.; Ikuhara, Y.; Wan, L.-J. Rutile-TiO_2 nanocoating for a high-rate $Li_4Ti_5O_{12}$ anode of a lithium-ion battery. *J. Am. Chem. Soc.* **2012**, *134*, 7874–7879.

[123] Wang, Y.; Liu, H.; Wang, K.; Eiji, H.; Wang, Y.; Zhou, H. Synthesis and electrochemical performance of nano-sized $Li_4Ti_5O_{12}$ with double surface modification of Ti(III) and carbon. *J. Mater. Chem.* **2009**, *19*, 6789–6795.

[124] Song, M.-S.; Benayad, A.; Choi, Y.-M.; Park, K.-S. Does $Li_4Ti_5O_{12}$ need carbon in lithium ion batteries? Carbon-free electrode with exceptionally high electrode capacity. *Chem. Commun.* **2012**, *48*, 516–518.

[125] Haetge, J.; Hartmann, P. Nanocrystalline framework for high rate rechargeable lithium batteries: Relationships among charge storage, electrical conductivity, and nanoscale structure. *Chem. Mater.* **2011**, *23*, 4384–4393.

[126] Shen, L.; Yuan, C.; Luo, H.; Zhang, X.; Xu, K.; Xia, Y. Facile synthesis of hierarchically porous $Li_4Ti_5O_{12}$ microspheres for high rate lithium ion batteries. *J. Mater. Chem.* **2010**, *20*, 6998–7004.

[127] Woo, S.-W.; Dokko, K.; Kanamura, K. Preparation and characterization of three dimensionally ordered macroporous $Li_4Ti_5O_{12}$ anode for lithium batteries. *Electrochim. Acta* **2007**, *53*, 79–82.

[128] Zhao, L.; Hu, Y.-S.; Li, H.; Wang, Z.; Chen, L. Porous $Li_4Ti_5O_{12}$ coated with N-doped carbon from ionic liquids for Li-ion batteries. *Adv. Mater.* **2011**, *23*, 1385–1388.

[129] Jiang, C.; Zhou, Y.; Honma, I.; Kudo, T.; Zhou, H. Preparation and rate capability of $Li_4Ti_5O_{12}$ hollow-sphere anode material. *J. Power Sources* **2007**, *166*, 514–518.

[130] Tang, Y.; Yang, L.; Fang, S.; Qiu, Z. $Li_4Ti_5O_{12}$ hollow microspheres assembled by nanosheets as an anode material for high-rate lithium ion batteries. *Electrochim. Acta* **2009**, *54*, 6244–6249.

[131] Jung, H.-G.; Jang, M. W.; Hassoun, J.; Sun, Y.-K.; Scrosati, B. A high-rate long-life $Li_4Ti_5O_{12}/Li[Ni_{0.45}Co_{0.1}Mn_{1.45}]O_4$ lithium-ion battery. *Nature Commun.* **2011**, *2*, 516.

[132] Landi, B. J.; Ganter, M. J.; Cress, C. D.; DiLeo, R. A.; Raffaelle, R. P. Carbon nanotubes for lithium ion batteries. *Energy Environ. Sci.* **2009**, *2*, 638–654.

[133] Chen, J.; Minett, A. I.; Liu, Y.; Lynam, C.; Sherrell, P.; Wang, C.; Wallace, G. G. Direct growth of flexible carbon nanotube electrodes. *Adv. Mater.* **2008**, *20*, 566–570.

[134] Yang, S.; Song, H.; Chen, X.; Okotrub, A. V.; Bulusheva, L. G. Electrochemical performance of arc-produced carbon nanotubes as anode material for lithium-ion batteries. *Electrochim. Acta* **2007**, *52*, 5286–5293.

[135] Chew, S. Y.; Ng, S. H.; Wang, J.; Novák, P.; Krumeich, F.; Chou, S. L.; Chen, J.; Liu, H. K. Flexible free-standing carbon nanotube films for model lithium-ion batteries. *Carbon* **2009**, *47*, 2976–2983.

[136] Lee, S. W.; Yabuuchi, N.; Gallant, B. M.; Chen, S.; Kim, B.-S.; Hammond, P. T.; Shao-Horn, Y. High-power lithium batteries from functionalized carbon-nanotube electrodes. *Nat. Nanotechnol.* **2010**, *5*, 531–537.

[137] Landi, B. J.; Ganter, M. J.; Schauerman, C. M.; Cress, C. D.; Raffaelle, R. P. Lithium ion capacity of single wall carbon nanotube paper electrodes. *J. Phys. Chem. C* **2008**, *112*, 7509–7515.

[138] Masarapu, C.; Subramanian, V.; Zhu, H.; Wei, B. Long-cycle electrochemical behavior of multiwall carbon nanotubes synthesized on stainless steel in Li ion batteries. *Adv. Funct. Mater.* **2009**, *19*, 1008–1014.

[139] Wang, X. X.; Wang, J. N.; Chang, H.; Zhang, Y. F. Preparation of short carbon nanotubes and application as an electrode material in Li-ion batteries. *Adv. Funct. Mater.* **2007**, *17*, 3613–3618.

[140] Guo, B.; Wang, X.; Fulvio, P. F.; Chi, M.; Mahurin, S. M.; Sun, X.-G.; Dai, S. Soft-templated mesoporous carbon-carbon nanotube composites for high performance lithium-ion batteries. *Adv. Mater.* **2011**, *23*, 4661–4666.

[141] Ji, L.; Zhang, X. Fabrication of porous carbon nanofibers and their application as anode materials for rechargeable lithium-ion batteries. *Nanotechnology* **2009**, *20*, 155705.

[142] Qie, L.; Chen, W.-M.; Wang, Z.-H.; Shao, Q.-G.; Li, X.; Yuan, L.-X.; Hu, X.-L.; Zhang, W.-X.; Huang, Y.-H. Nitrogen-doped porous carbon nanofiber webs as anodes for lithium ion batteries with a superhigh capacity and rate capability. *Adv. Mater.* **2012**, *24*, 2047–2050.

[143] Zhang, J.; Hu, Y.-S.; Tessonnier, J.-P.; Weinberg, G.; Maier, J.; Schlögl, R.; Su, D. S. CNFs@CNTs: Superior carbon for electrochemical energy storage. *Adv. Mater.* **2008**, *20*, 1450–1455.

[144] Yang, S.; Huo, J.; Song, H.; Chen, X. A comparative study of electrochemical properties of two kinds of carbon nanotubes as anode materials for lithium ion batteries. *Electrochim. Acta* **2008**, *53*, 2238–2244.

[145] Geim, A. K.; Novoselov, K. S. The rise of graphene. *Nat. Mater.* **2007**, *6*, 183–191.

[146] Brownson, D. A. C.; Kampouris, D. K.; Banks, C. E. An overview of graphene in energy production and storage applications. *J. Power Sources* **2011**, *196*, 4873–4885.

[147] Sun, Y.; Wu, Q.; Shi, G. Graphene based new energy materials. *Energy Environ. Sci.* **2011**, *4*, 1113–1132.

[148] Pumera, M. Graphene-based nanomaterials for energy storage. *Energy Environ. Sci.* **2011**, *4*, 668–674.

[149] Uthaisar, C.; Barone, V. Edge effects on the characteristics of Li diffusion in graphene. *Nano Lett.* **2010**, *10*, 2838–2842.

[150] Pollak, E.; Geng, B.; Jeon, K.-J.; Lucas, I. T.; Richardson, T. J.; Wang, F.; Kostecki, R. The interaction of Li^+ with single-layer and few-layer graphene. *Nano Lett.* **2010**, *10*, 3386–3388.

[151] Pan, D.; Wang, S.; Zhao, B.; Wu, M.; Zhang, H.; Wang, Y.; Jiao, Z. Li storage properties of disordered graphene nanosheets. *Chem. Mater.* **2009**, *21*, 3136–3142.

[152] Lian, P.; Zhu, X.; Liang, S.; Li, Z.; Yang, W.; Wang, H. Large reversible capacity of high quality graphene sheets as an anode material for lithium-ion batteries. *Electrochim. Acta* **2010**, *55*, 3909–3914.

[153] Bhardwaj, T.; Antic, A.; Pavan, B.; Barone, V.; Fahlman, B. D. Enhanced electrochemical lithium storage by graphene nanoribbons. *J. Am. Chem. Soc.* **2010**, *132*, 12556–12558.

[154] Guo, P.; Song, H.; Chen, X. Electrochemical performance of graphene nanosheets as anode material for lithium-ion batteries. *Electrochem. Commun.* **2009**, *11*, 1320–1324.

[155] Yoo, E.; Kim, J.; Hosono, E.; Zhou, H.; Kudo, T.; Honma, I. Large reversible Li storage of graphene nanosheet families for use in rechargeable lithium ion batteries. *Nano Lett.* **2008**, *8*, 2277–2282.

[156] Wang, C.; Li, D.; Too, C.; Wallace, G. Electrochemical properties of graphene paper electrodes used in lithium batteries. *Chem. Mater* **2009**, 2008–2010.

[157] Abouimrane, A.; Compton, O. C.; Amine, K.; Nguyen, S. T. Non-annealed graphene paper as a binder-free anode for lithium-ion batteries. *J. Phys. Chem. C* **2010**, *114*, 12800–12804.

[158] Liu, F.; Song, S.; Xue, D.; Zhang, H. Folded structured graphene paper for high performance electrode materials. *Adv. Mater.* **2012**, *24*, 1089–1094.

[159] Yang, S.; Feng, X.; Zhi, L.; Cao, Q.; Maier, J.; Müllen, K. Nanographene-constructed hollow carbon spheres and their favorable electroactivity with respect to lithium storage. *Adv. Mater.* **2010**, *22*, 838–842.

[160] Wang, K.; Li, Z.; Wang, Y.; Liu, H.; Chen, J.; Holmes, J.; Zhou, H. Carbon nanocages with nanographene shell for high-rate lithium ion batteries. *J. Mater. Chem.* **2010**, *20*, 9748–9753.

[161] Li, G.; Xu, L.; Hao, Q.; Wang, M.; Qian, Y. Synthesis, characterization and application of carbon nanocages as anode materials for high-performance lithium-ion batteries. *RSC Adv.* **2012**, *2*, 284–291.

[162] Poizot, P.; Laruelle, S.; Grugeon, S.; Dupont, L.; Tarascon, J. M. Nano-sized transition-metal oxides as negative-electrode materials for lithium-ion batteries. *Nature* **2000**, *407*, 496–469.

[163] Hao, R.; Xing, R.; Xu, Z.; Hou, Y.; Gao, S.; Sun, S. Synthesis, functionalization, and biomedical applications of multifunctional magnetic nanoparticles. *Adv. Mater.* **2010**, *22*, 2729–2742.

[164] NuLi, Y.; Zeng, R.; Zhang, P.; Guo, Z.; Liu, H. Controlled synthesis of α-Fe_2O_3 nanostructures and their size-dependent electrochemical properties for lithium-ion batteries. *J. Power Sources* **2008**, *184*, 456–461.

[165] Larcher, D.; Masquelier, C.; Bonnin, D. Effect of particle size on lithium intercalation into α-Fe_2O_3. *J. Electrochem. Soc.* **2003**, *150*, A133–A139.

[166] Reddy, M. V.; Yu, T.; Sow, C. H.; Shen, Z. X.; Lim, C. T.; Subba Rao, G. V.; Chowdari, B. V. R. α-Fe_2O_3

nanoflakes as an anode material for Li-ion batteries. *Adv. Funct. Mater.* **2007**, *17*, 2792–2799.

[167] Kim, H. S.; Piao, Y.; Kang, S. H.; Hyeon, T.; Sung, Y.-E. Uniform hematite nanocapsules based on an anode material for lithium ion batteries. *Electrochem. Commun.* **2010**, *12*, 382–385.

[168] Chen, J. S.; Zhu, T.; Yang, X. H.; Yang, H. G.; Lou, X. W. Top-down fabrication of α-Fe_2O_3 single-crystal nanodiscs and microparticles with tunable porosity for largely improved lithium storage properties. *J. Am. Chem. Soc.* **2010**, *132*, 13162–13164.

[169] Koo, B.; Xiong, H.; Slater, M. D.; Prakapenka, V. B.; Balasubramanian, M.; Podsiadlo, P.; Johnson, C. S.; Rajh, T.; Shevchenko, E. V Hollow iron oxide nanoparticles for application in lithium ion batteries. *Nano Lett.* **2012**, *12*, 2429–2435.

[170] Liu, J.; Li, Y.; Fan, H.; Zhu, Z.; Jiang, J.; Ding, R.; Hu, Y.; Huang, X. Iron oxide-based nanotube arrays derived from sacrificial template-accelerated hydrolysis: Large-area design and reversible lithium storage. *Chem. Mater.* **2010**, *22*, 212–217.

[171] Zhu, X.; Zhu, Y.; Murali, S.; Stoller, M. D.; Ruoff, R. S. Nanostructured reduced graphene oxide/Fe_2O_3 composite as a high-performance anode material for lithium ion batteries. *ACS Nano* **2011**, *5*, 3333–3338.

[172] Chen, J. S.; Zhang, Y.; Lou, X. W. D. One-pot synthesis of uniform Fe_3O_4 nanospheres with carbon matrix support for improved lithium storage capabilities. *ACS Appl. Mater. Interfaces* **2011**, *3*, 3276–3279.

[173] Zhang, W.-M.; Wu, X.-L.; Hu, J.-S.; Guo, Y.-G.; Wan, L.-J. Carbon coated Fe_3O_4 nanospindles as a superior anode material for lithium-ion batteries. *Adv. Funct. Mater.* **2008**, *18*, 3941–3946.

[174] Muraliganth, T.; Vadivel Murugan, A.; Manthiram, A. Facile synthesis of carbon-decorated single-crystalline Fe3O4 nanowires and their application as high performance anode in lithium ion batteries. *Chem. Commun.* **2009**, 7360–7362.

[175] Cui, Z.; Jiang, L. High-yield gas–liquid interfacial synthesis of highly dispersed Fe_3O_4 nanocrystals and their application in lithium-ion batteries. *Chem. Mater.* **2009**, *21*, 1162–1166.

[176] Wang, L.; Yu, Y.; Chen, P. C.; Zhang, D. W.; Chen, C. H. Electrospinning synthesis of C/Fe_3O_4 composite nanofibers and their application for high performance lithium-ion batteries. *J. Power Sources* **2008**, *183*, 717–723.

[177] Zhang, Q.; Shi, Z.; Deng, Y.; Zheng, J.; Liu, G.; Chen, G. Hollow Fe_3O_4/C spheres as superior lithium storage materials. *J. Power Sources* **2012**, *197*, 305–309.

[178] Chen, D.; Ji, G.; Ma, Y.; Lee, J. Y.; Lu, J. Graphene-encapsulated hollow Fe_3O_4 nanoparticle aggregates as a high-performance anode material for lithium ion batteries. *ACS Appl. Mater. Interfaces* **2011**, *3*, 3078–3083.

[179] Zhou, G.; Wang, D.-W.; Li, F.; Zhang, L.; Li, N.; Wu, Z.-S.; Wen, L.; Lu, G. Q. (Max); Cheng, H.-M. Graphene-wrapped Fe_3O_4 anode material with improved reversible capacity and cyclic stability for lithium ion batteries. *Chem. Mater.* **2010**, *22*, 5306–5313.

[180] Wang, J.-Z.; Zhong, C.; Wexler, D.; Idris, N. H.; Wang, Z.-X.; Chen, L.-Q.; Liu, H.-K. Graphene-encapsulated Fe_3O_4 nanoparticles with 3D laminated structure as superior anode in lithium ion batteries. *Chem. Eur. J.* **2011**, *17*, 661–667.

[181] Lian, P.; Zhu, X.; Xiang, H.; Li, Z.; Yang, W.; Wang, H. Enhanced cycling performance of Fe_3O_4–graphene nanocomposite as an anode material

for lithium-ion batteries. *Electrochim. Acta* **2010**, *56*, 834–840.

[182] Su, J.; Cao, M.; Ren, L.; Hu, C. Fe_3O_4–graphene nanocomposites with improved lithium-storage and magnetism properties. *J. Phys. Chem. C* **2011**, *115*, 14469–14477.

[183] Li, X.; Huang, X.; Liu, D.; Wang, X. Synthesis of 3D hierarchical Fe_3O_4/graphene composites with high lithium storage capacity and for controlled drug delivery. *J. Phys. Chem. C* **2011**, *115*, 21567–21573.

[184] Ji, L.; Tan, Z.; Kuykendall, T. R.; Aloni, S.; Xun, S.; Lin, E.; Battaglia, V.; Zhang, Y. Fe_3O_4 nanoparticle-integrated graphene sheets for high-performance half and full lithium ion cells. *Phys. Chem. Chem. Phys.* **2011**, *13*, 7170–7177.

[185] Li, B.; Cao, H.; Shao, J.; Qu, M. Enhanced anode performances of the Fe_3O_4–carbon–rGO three dimensional composite in lithium ion batteries. *Chem. Commun.* **2011**, *47*, 10374–10376.

[186] Ban, C.; Wu, Z.; Gillaspie, D. T.; Chen, L.; Yan, Y.; Blackburn, J. L.; Dillon, A. C. Nanostructured Fe_3O_4/SWNT electrode: Binder-free and high-rate Li-ion anode. *Adv. Mater.* **2010**, *22*, E145–E149.

[187] Wang, S.; Zhang, J.; Chen, C. Fe_3O_4 submicron spheroids as anode materials for lithium-ion batteries with stable and high electrochemical performance. *J. Power Sources* **2010**, *195*, 5379–5381.

[188] Shaju, K. M.; Jiao, F.; Débart, A.; Bruce, P. G. Mesoporous and nanowire Co_3O_4 as negative electrodes for rechargeable lithium batteries. *Phys. Chem. Chem. Phys.* **2007**, *9*, 1837–1842.

[189] Li, Y.; Tan, B.; Wu, Y. Mesoporous Co_3O_4 nanowire arrays for lithium ion batteries with high capacity and rate capability. *Nano Lett.* **2008**, *8*, 265–270.

[190] Li, C.; Yin, X.; Chen, L.; Li, Q.; Wang, T. Synthesis of cobalt ion-based coordination polymer nanowires and their conversion into porous Co_3O_4 nanowires with good lithium storage properties. *Chem. Eur. J.* **2010**, *16*, 5215–5221.

[191] Zhang, P.; Guo, Z. P.; Huang, Y.; Jia, D.; Liu, H. K. Synthesis of Co_3O_4/carbon composite nanowires and their electrochemical properties. *J. Power Sources* **2011**, *196*, 6987–6991.

[192] Du, N.; Zhang, H.; Chen, B. D.; Wu, J. B.; Ma, X. Y.; Liu, Z. H.; Zhang, Y. Q.; Yang, D. R.; Huang, X. H.; Tu, J. P. Porous Co_3O_4 nanotubes derived from $Co_4(CO)_{12}$ clusters on carbon nanotube templates: A highly efficient material for Li-battery applications. *Adv. Mater.* **2007**, *19*, 4505–4509.

[193] Lou, X. W.; Deng, D.; Lee, J. Y.; Feng, J.; Archer, L. A. Self-supported formation of needlelike Co_3O_4 nanotubes and their application as lithium-ion battery electrodes. *Adv. Mater.* **2008**, *20*, 258–262.

[194] Lou, X. W.; Deng, D.; Lee, J. Y.; Archer, L. A. Thermal formation of mesoporous single-crystal Co_3O_4 nano-needles and their lithium storage properties. *J. Mater. Chem.* **2008**, *18*, 4397–4401.

[195] Tian, L.; Zou, H.; Fu, J.; Yang, X.; Wang, Y.; Guo, H.; Fu, X.; Liang, C.; Wu, M.; Shen, P. K. et al. Topotactic conversion route to mesoporous quasi-single-crystalline Co_3O_4 nanobelts with optimizable electrochemical performance. *Adv. Funct. Mater.* **2010**, *20*, 617–623.

[196] Zhan, F.; Geng, B.; Guo, Y. Porous Co_3O_4 nanosheets with extraordinarily high discharge capacity for lithium batteries. *Chem. Eur. J.* **2009**, *15*, 6169–6174.

[197] Wang, X.; Wu, X.-L.; Guo, Y.-G.; Zhong, Y.; Cao, X.; Ma, Y.; Yao, J. Synthesis and lithium storage

properties of Co_3O_4 nanosheet-assembled multishelled hollow spheres. *Adv. Funct. Mater.* **2010**, *20*, 1680–1686.

[198] Wang, X.; Yu, L.; Wu, X. Synthesis of single-crystalline Co_3O_4 octahedral cages with tunable surface aperture and their lithium storage properties. *J. Phys. Chem. C* **2009**, *113*, 15553–15558.

[199] Chen, S. Q.; Wang, Y. Microwave-assisted synthesis of a Co_3O_4–graphene sheet-on-sheet nanocomposite as a superior anode material for Li-ion batteries. *J. Mater. Chem.* **2010**, *20*, 9735–9739.

[200] Li, B.; Cao, H.; Shao, J.; Li, G.; Qu, M.; Yin, G. Co_3O_4@graphene composites as anode materials for high-performance lithium ion batteries. *Inorg. Chem.* **2011**, *50*, 1628–1632.

[201] Zhu, J.; Sharma, Y. K.; Zeng, Z.; Zhang, X.; Srinivasan, M.; Mhaisalkar, S.; Zhang, H.; Hng, H. H.; Yan, Q. Cobalt oxide nanowall arrays on reduced graphene oxide sheets with controlled phase, grain size, and porosity for Li-ion battery electrodes. *J. Phys. Chem. C* **2011**, *115*, 8400–8406.

[202] Wu, Z.; Ren, W.; Wen, L.; Gao, L.; Zhao, J.; Chen, Z.; Zhou, G.; Li, F.; Cheng, H. Graphene anchored with Co_3O_4 nanoparticles as anode of lithium ion capacity and cyclic performance. *ACS Nano* **2010**, *4*, 3187–3194.

[203] Kim, H.; Seo, D.-H.; Kim, S.-W.; Kim, J.; Kang, K. Highly reversible Co_3O_4/graphene hybrid anode for lithium rechargeable batteries. *Carbon* **2011**, *49*, 326–332.

[204] Cheng, H.; Lu, Z. G.; Deng, J. Q.; Chung, C. Y.; Zhang, K.; Li, Y. Y. A facile method to improve the high rate capability of Co_3O_4 nanowire array electrodes. *Nano Res.* **2010**, *3*, 895–901.

[205] Wang, X.; Yang, Z.; Sun, X.; Li, X.; Wang, D.; Wang, P.; He, D. NiO nanocone array electrode with high capacity and rate capability for Li-ion batteries. *J. Mater. Chem.* **2011**, *21*, 9988–9990.

[206] Hassan, M. F.; Guo, Z. P.; Chen, Z.; Liu, H. K. Carbon-coated MoO_3 nanobelts as anode materials for lithium-ion batteries. *J. Power Sources* **2010**, *195*, 2372–2376.

[207] Zhong, K.; Xia, X.; Zhang, B.; Li, H.; Wang, Z.; Chen, L. MnO powder as anode active materials for lithium ion batteries. *J. Power Sources* **2010**, *195*, 3300–3308.

[208] Xu, G.-L.; Xu, Y.-F.; Sun, H.; Fu, F.; Zheng, X.-M.; Huang, L.; Li, J.-T.; Yang, S.-H.; Sun, S.-G. Facile synthesis of porous MnO/C nanotubes as a high capacity anode material for lithium ion batteries. *Chem. Commun.* **2012**, *48*, 8502–8504.

[209] Li, L.; Nan, C.; Lu, J.; Peng, Q.; Li, Y. α-MnO_2 nanotubes: high surface area and enhanced lithium battery properties. *Chem. Commun.* **2012**, *48*, 6945–6947.

[210] Reddy, A. L. M.; Shaijumon, M. M.; Gowda, S. R.; Ajayan, P. M. Coaxial MnO_2/carbon nanotube array electrodes for high-performance lithium batteries. *Nano Lett.* **2009**, *9*, 1002–1006.

[211] Xia, H.; Lai, M.; Lu, L. Nanoflaky MnO_2/carbon nanotube nanocomposites as anode materials for lithium-ion batteries. *J. Mater. Chem.* **2010**, *20*, 6896–6902.

[212] Ji, L.; Zhang, X. Manganese oxide nanoparticle-loaded porous carbon nanofibers as anode materials for high-performance lithium-ion batteries. *Electrochem. Commun.* **2009**, *11*, 795–798.

[213] Wang, H.; Cui, L.-F.; Yang, Y.; Sanchez Casalongue, H.; Robinson, J. T.; Liang, Y.; Cui, Y.; Dai, H. Mn_3O_4–graphene hybrid as a high-capacity anode

material for lithium ion batteries. *J. Am. Chem. Soc.* **2010**, *132*, 13978–139780.

[214] Varghese, B.; Reddy, M. V.; Yanwu, Z.; Lit, C. S.; Hoong, T. C.; Subba Rao, G. V.; Chowdari, B. V. R.; Wee, A. T. S.; et al. Fabrication of NiO nanowall electrodes for high performance lithium ion battery. *Chem. Mater.* **2008**, *20*, 3360–3367.

[215] Wang, X.; Li, X.; Sun, X.; Li, F.; Liu, Q.; Wang, Q.; He, D. Nanostructured NiO electrode for high rate Li-ion batteries. *J. Mater. Chem.* **2011**, *21*, 3571–3573.

[216] Ci, S.; Zou, J.; Zeng, G.; Peng, Q.; Luo, S.; Wen, Z. Improved electrochemical properties of single crystalline NiO nanoflakes for lithium storage and oxygen electroreduction. *RSC Adv.* **2012**, *2*, 5185–5192.

[217] Mai, Y. J.; Tu, J. P.; Xia, X. H.; Gu, C. D.; Wang, X. L. Co-doped NiO nanoflake arrays toward superior anode materials for lithium ion batteries. *J. Power Sources* **2011**, *196*, 6388–6393.

[218] Zhou, G.; Wang, D.-W.; Yin, L.-C.; Li, N.; Li, F.; Cheng, H.-M. Oxygen bridges between NiO nanosheets and graphene for improvement of lithium storage. *ACS Nano* **2012**, *6*, 3214–3223.

[219] Huang, Y.; Huang, X.; Lian, J.; Xu, D.; Wang, L.; Zhang, X. Self-assembly of ultrathin porous NiO nanosheets/graphene hierarchical structure for high-capacity and high-rate lithium storage. *J. Mater. Chem.* **2012**, *22*, 2844–2847.

[220] Xu, C.; Sun, J.; Gao, L. Large scale synthesis of nickel oxide/multiwalled carbon nanotube composites by direct thermal decomposition and their lithium storage properties. *J. Power Sources* **2011**, *196*, 5138–5142.

[221] Liu, H.; Wang, G.; Liu, J.; Qiao, S.; Ahn, H. Highly ordered mesoporous NiO anode material for lithium ion batteries with an excellent electrochemical performance. *J. Mater. Chem.* **2011**, *21*, 3046–3052.

[222] Chen, X.; Zhang, N.; Sun, K. Facile fabrication of CuO 1D pine-needle-like arrays for super-rate lithium storage. *J. Mater. Chem.* **2012**, *22*, 15080–15084.

[223] Wang, L.; Cheng, W.; Gong, H.; Wang, C.; Wang, D.; Tang, K.; Qian, Y. Facile synthesis of nanocrystalline-assembled bundle-like CuO nanostructure with high rate capacities and enhanced cycling stability as an anode material for lithium-ion batteries. *J. Mater. Chem.* **2012**, *22*, 11297–11302.

[224] Wang, F.; Tao, W.; Zhao, M.; Xu, M.; Yang, S.; Sun, Z.; Wang, L.; Song, X. Controlled synthesis of uniform ultrafine CuO nanowires as anode material for lithium-ion batteries. *J. Alloys Compd.* **2011**, *509*, 9798–9803.

[225] Chen, L. B.; Lu, N.; Xu, C. M.; Yu, H. C.; Wang, T. H. Electrochemical performance of polycrystalline CuO nanowires as anode material for Li ion batteries. *Electrochim. Acta* **2009**, *54*, 4198–4201.

[226] Ke, F.-S.; Huang, L.; Wei, G.-Z.; Xue, L.-J.; Li, J.-T.; Zhang, B.; Chen, S.-R.; Fan, X.-Y.; Sun, S.-G. One-step fabrication of CuO nanoribbons array electrode and its excellent lithium storage performance. *Electrochim. Acta* **2009**, *54*, 5825–5829.

[227] Chen, X.; Zhang, N.; Sun, K. Facile fabrication of CuO mesoporous nanosheet cluster array electrodes with super lithium-storage properties. *J. Mater. Chem.* **2012**, *22*, 13637–13642.

[228] Wang, Z.; Su, F.; Madhavi, S.; Lou, X. W. CuO nanostructures supported on Cu substrate as integrated electrodes for highly reversible lithium storage. *Nanoscale* **2011**, *3*, 1618–1623.

[229] Wang, H.; Pan, Q.; Zhao, J.; Yin, G.; Zuo, P. Fabrication of CuO film with network-like architectures through solution-immersion and their application in lithium ion batteries. *J. Power Sources* **2007**, *167*, 206–211.

[230] Xiang, J. Y.; Tu, J. P.; Huang, X. H.; Yang, Y. Z. A comparison of anodically grown CuO nanotube film and Cu_2O film as anodes for lithium ion batteries. *J. Solid State Electrochem.* **2007**, *12*, 941–945.

[231] Wang, B.; Wu, X.-L.; Shu, C.-Y.; Guo, Y.-G.; Wang, C.-R. Synthesis of CuO/graphene nanocomposite as a high-performance anode material for lithium-ion batteries. *J. Mater. Chem.* **2010**, *20*, 10661–10664.

[232] Mai, Y. J.; Wang, X. L.; Xiang, J. Y.; Qiao, Y. Q.; Zhang, D.; Gu, C. D.; Tu, J. P. CuO/graphene composite as anode materials for lithium-ion batteries. *Electrochim. Acta* **2011**, *56*, 2306–2311.

[233] Lu, L. Q.; Wang, Y. Sheet-like and fusiform CuO nanostructures grown on graphene by rapid microwave heating for high Li-ion storage capacities. *J. Mater. Chem.* **2011**, *21*, 17916–17921.

[234] Ko, S.; Lee, J.-I.; Yang, H. S.; Park, S.; Jeong, U. Mesoporous CuO particles threaded with CNTs for high-performance lithium-ion battery anodes. *Adv. Mater.* **2012**, *24*, 4451–4456.

[235] Xiang, J. Y.; Tu, J. P.; Zhang, J.; Zhong, J.; Zhang, D.; Cheng, J. P. Incorporation of MWCNTs into leaf-like CuO nanoplates for superior reversible Li-ion storage. *Electrochem. Commun.* **2010**, *12*, 1103–1107.

[236] Wang, H.; Pan, Q.; Cheng, Y.; Zhao, J.; Yin, G. Evaluation of ZnO nanorod arrays with dandelion-like morphology as negative electrodes for lithium-ion batteries. *Electrochim. Acta* **2009**, *54*, 2851–2855.

[237] Huang, X. H.; Xia, X. H.; Yuan, Y. F.; Zhou, F. Porous ZnO nanosheets grown on copper substrates as anodes for lithium ion batteries. *Electrochim. Acta* **2011**, *56*, 4960–4965.

[238] Liu, J.; Li, Y.; Ding, R.; Jiang, J.; Hu, Y.; Ji, X.; Chi, Q.; Zhu, Z.; Huang, X. Carbon/ZnO nanorod array electrode with significantly improved lithium storage capability. *J. Phys. Chem. C* **2009**, *113*, 5336–5339.

[239] Ahmad, M.; Yingying, S.; Nisar, A.; Sun, H.; Shen, W.; Wei, M.; Zhu, J. Synthesis of hierarchical flower-like ZnO nanostructures and their functionalization by Au nanoparticles for improved photocatalytic and high performance Li-ion battery anodes. *J. Mater. Chem.* **2011**, *21*, 7723–7729.

[240] Zhang, C. Q.; Tu, J. P.; Yuan, Y. F.; Huang, X. H.; Chen, X. T.; Mao, F. Electrochemical performances of Ni-coated ZnO as an anode material for lithium-ion batteries. *J. Electrochem. Soc.* **2007**, *154*, A65–A69.

[241] Shi, Y.; Guo, B.; Corr, S. a; Shi, Q.; Hu, Y.-S.; Heier, K. R.; Chen, L.; Seshadri, R.; Stucky, G. D. Ordered mesoporous metallic MoO_2 materials with highly reversible lithium storage capacity. *Nano Lett.* **2009**, *9*, 4215–4220.

[242] Sun, Y.; Hu, X.; Yu, J. C.; Li, Q.; Luo, W.; Yuan, L.; Zhang, W.; Huang, Y. Morphosynthesis of a hierarchical MoO_2 nanoarchitecture as a binder-free anode for lithium-ion batteries. *Energy Environ. Sci.* **2011**, *4*, 2870–2877.

[243] Wang, Z.; Chen, J. S.; Zhu, T.; Madhavi, S.; Lou, X. W. One-pot synthesis of uniform carbon-coated MoO_2 nanospheres for high-rate reversible lithium storage. *Chem. Commun.* **2010**, *46*, 6906–6908.

[244] Luo, W.; Hu, X.; Sun, Y.; Huang, Y. Electrospinning of carbon-coated MoO_2 nanofibers with enhanced lithium-storage properties. *Phys. Chem. Chem. Phys.* **2011**, *13*, 16735–16740.

[245] Zhou, L.; Wu, H. Bin; Wang, Z.; Lou, X. W. D. Interconnected MoO_2 nanocrystals with carbon nanocoating as high-capacity anode materials for lithium-ion batteries. *ACS Appl. Mater. Interfaces* **2011**, *3*, 4853–4857.

[246] Lee, S.-H.; Kim, Y.-H.; Deshpande, R.; Parilla, P. A.; Whitney, E.; Gillaspie, D. T.; Jones, K. M.; Mahan, A. H.; Zhang, S.; Dillon, A. C. Reversible lithium-ion insertion in molybdenum oxide nanoparticles. *Adv. Mater.* **2008**, *20*, 3627–3632.

[247] Riley, L. A.; Lee, S.-H.; Gedvilias, L.; Dillon, A. C. Optimization of MoO_3 nanoparticles as negative-electrode material in high-energy lithium ion batteries. *J. Power Sources* **2010**, *195*, 588–592.

[248] Mizushima, K.; Jones, P. C.; Wiseman, P. J.; Goodenough, J. B. Li_xCoO_2 ($0 < x \leq 1$): A new cathode material for batteries of high energy density. *Mater. Res. Bull.* **1980**, *15*, 783–789.

[249] Chen, H.; Grey, C. P. Molten salt synthesis and high rate performance of the "Desert-Rose" form of $LiCoO_2$. *Adv. Mater.* **2008**, *20*, 2206–2210.

[250] Lu, H.-W.; Yu, L.; Zeng, W.; Li, Y.-S.; Fu, Z.-W. Fabrication and electrochemical properties of three-dimensional structure of $LiCoO_2$ fibers. *Electrochem. Solid-State Lett.* **2008**, *11*, A140–A144.

[251] Pentyala, N.; Guduru, R. K.; Mohanty, P. S. Binder free porous ultrafine/nano structured $LiCoO_2$ cathode from plasma deposited cobalt. *Electrochim. Acta* **2011**, *56*, 9851–9859.

[252] Quan, Z.; Iwase, K.; Sonoyama, N. Synthesis and electrochemical property of $LiCoO_2$ thin films composed of nanosize compounds synthesized via nanosheet restacking method. *J. Power Sources* **2011**, *196*, 6762–6767.

[253] Xiao, X.; Yang, L.; Zhao, H.; Hu, Z.; Li, Y. Facile synthesis of $LiCoO_2$ nanowires with high electrochemical performance. *Nano Res.* **2011**, *5*, 27–32.

[254] Xiao, X.; Liu, X.; Wang, L.; Zhao, H.; Hu, Z.; He, X.; Li, Y. $LiCoO_2$ nanoplates with exposed (001) planes and high rate capability for lithium-ion batteries. *Nano Res.* **2012**, *5*, 395–401.

[255] Mizuno, Y.; Hosono, E.; Saito, T.; Okubo, M.; Nishio-Hamane, D.; Oh-ishi, K.; Kudo, T.; Zhou, H. Electrospinning synthesis of wire-structured $LiCoO_2$ for electrode materials of high-power Li-ion batteries. *J. Phys. Chem. C* **2012**, *116*, 10774–10780.

[256] Jung, Y. S.; Cavanagh, A. S.; Dillon, A. C.; Groner, M. D.; George, S. M.; Lee, S.-H. Enhanced stability of $LiCoO_2$ cathodes in lithium-ion batteries using surface modification by atomic layer deposition. *J. Electrochem. Soc.* **2010**, *157*, A75–A81.

[257] Luo, S.; Wang, K.; Wang, J.; Jiang, K.; Li, Q.; Fan, S. Binder-free $LiCoO_2$/carbon nanotube cathodes for high-performance lithium ion batteries. *Adv. Mater.* **2012**, *24*, 2294–2298.

[258] Tarascon, J.; Armand, M. Issues and challenges facing rechargeable lithium batteries. *Nature* **2001**, *414*, 359–367.

[259] Chen, Z.; Qin, Y.; Amine, K.; Sun, Y.-K. Role of surface coating on cathode materials for lithium-ion batteries. *J. Mater. Chem.* **2010**, *20*, 7606–7612.

[260] Hao, Q.; Ma, H.; Ju, Z.; Li, G.; Li, X.; Xu, L.; Qian, Y. Nano-CuO coated $LiCoO_2$: Synthesis, improved cycling stability and good performance at high rates. *Electrochim. Acta* **2011**, *56*, 9027–9031.

[261] Pu, X.; Yin, L.; Yu, C. Functional surface modifications on nanostructured $LiCoO_2$ with lithium vanadates. *J. Nanopart. Res.* **2012**, *14*, 788.

[262] Scott, I. D.; Jung, Y. S.; Cavanagh, A. S.; Yan, Y.; Dillon, A. C.; George, S. M.; Lee, S.-H. Ultrathin coatings on nano-$LiCoO_2$ for Li-ion vehicular applications. *Nano Lett.* **2011**, *11*, 414–418.

[263] Cheng, H.-M.; Wang, F.-M.; Chu, J. P.; Santhanam, R.; Rick, J.; Lo, S.-C. Enhanced cycleabity in lithium ion batteries: Resulting from atomic layer depostion of Al_2O_3 or TiO_2 on $LiCoO_2$ electrodes. *J. Phys. Chem. C* **2012**, *116*, 7629–7637.

[264] Park, O. K.; Cho, Y.; Lee, S.; Yoo, H.-C.; Song, H.-K.; Cho, J. Who will drive electric vehicles, olivine or spinel? *Energy Environ. Sci.* **2011**, *4*, 1621–1633.

[265] Hosono, E.; Kudo, T.; Honma, I.; Matsuda, H.; Zhou, H. Synthesis of single crystalline spinel $LiMn_2O_4$ nanowires for a lithium ion battery with high power density. *Nano Lett.* **2009**, *9*, 1045–1051.

[266] Kim, J.-H.; Ayalasomayajula, T.; Gona, V.; Choi, D. Fabrication and electrochemical characterization of a vertical array of MnO_2 nanowires grown on silicon substrates as a cathode material for lithium rechargeable batteries. *J. Power Sources* **2008**, *183*, 366–369.

[267] Lee, H.-W.; Muralidharan, P.; Ruffo, R.; Mari, C. M.; Cui, Y.; Kim, D. K. Ultrathin spinel $LiMn_2O_4$ nanowires as high power cathode materials for Li-ion batteries. *Nano Lett.* **2010**, *10*, 3852–3856.

[268] Luo, J.-Y.; Xiong, H.-M.; Xia, Y.-Y. $LiMn_2O_4$ nanorods, nanothorn microspheres, and hollow nanospheres as enhanced cathode materials of lithium ion battery. *J. Phys. Chem. C* **2008**, *112*, 12051–12057.

[269] Fang, H.; Li, L.; Yang, Y.; Yan, G.; Li, G. Low-temperature synthesis of highly crystallized $LiMn_2O_4$ from α-manganese dioxide nanorods. *J. Power Sources* **2008**, *184*, 494–497.

[270] Yang, Y.; Xie, C.; Ruffo, R.; Peng, H.; Kim, D. K.; Cui, Y. Single nanorod devices for battery diagnostics: a case study on $LiMn_2O_4$. *Nano Lett.* **2009**, *9*, 4109–4114.

[271] Kim, D. K.; Muralidharan, P.; Lee, H.-W.; Ruffo, R.; Yang, Y.; Chan, C. K.; Peng, H.; Huggins, R. A.; Cui, Y. Spinel $LiMn_2O_4$ nanorods as lithium ion battery cathodes. *Nano Lett.* **2008**, *8*, 3948–3952.

[272] Cho, J. VO_x-coated $LiMn_2O_4$ nanorod clusters for lithium battery cathode materials. *J. Mater. Chem.* **2008**, *18*, 2257–2261.

[273] Ding, Y.-L.; Xie, J.; Cao, G.-S.; Zhu, T.-J.; Yu, H.-M.; Zhao, X.-B. Single-crystalline $LiMn_2O_4$ nanotubes synthesized via template-engaged reaction as cathodes for high-power lithium ion batteries. *Adv. Funct. Mater.* **2011**, *21*, 348–355.

[274] Shaju, K. M.; Bruce, P. G. A Stoichiometric nano-$LiMn_2O_4$ spinel electrode exhibiting high power and stable cycling. *Chem. Mater.* **2008**, *20*, 5557–5562.

[275] Okubo, M.; Mizuno, Y.; Yamada, H.; Kim, J.; Hosono, E.; Zhou, H.; Kudo, T.; Honma, I. Fast Li-ion insertion into nanosized $LiMn_2O_4$ without domain boundaries. *ACS Nano* **2010**, *4*, 741–752.

[276] Tang, W.; Wang, X. J.; Hou, Y. Y.; Li, L. L.; Sun, H.; Zhu, Y. S.; Bai, Y.; Wu, Y. P.; Zhu, K.; van Ree, T. Nano $LiMn_2O_4$ as cathode material of high rate capability for lithium ion batteries. *J. Power Sources* **2012**, *198*, 308–311.

[277] Jiao, F.; Bao, J.; Hill, A. H.; Bruce, P. G. Synthesis of ordered mesoporous Li–Mn–O spinel as a positive electrode for rechargeable lithium batteries. *Angew. Chem. Int. Edit.* **2008**, *47*, 9711–9716.

[278] Tonti, D.; Torralvo, M. J.; Enciso, E.; Sobrados, I.; Sanz, J. Three-dimensionally ordered macroporous lithium manganese oxide for rechargeable lithium batteries. *Chem. Mater.* **2008**, *20*, 4783–4790.

[279] Thackeray, M. M.; David, W. I. F.; Bruce, P. G.; Goodenough, J. B. Lithium insertion into manganese spinels. *Mater. Res. Bull.* **1983**, *18*, 461–472.

[280] Şahan, H.; Göktepe, H.; Patat, S.; Ülgen, A. The effect of LBO coating method on electrochemical performance of $LiMn_2O_4$ cathode material. *Solid State Ionics* **2008**, *178*, 1837–1842.

[281] Lim, S.; Cho, J. PVP-Assisted ZrO_2 coating on $LiMn_2O_4$ spinel cathode nanoparticles prepared by MnO_2 nanowire templates. *Electrochem. Commun.* **2008**, *10*, 1478–1481.

[282] Feng, L.; Wang, S.; Han, L.; Qin, X.; Wei, H.; Yang, Y. Enhanced electrochemical properties of $LiMn_2O_4$ cathode material coated by 5 wt.% of nano-La_2O_3. *Mater. Lett.* **2012**, *78*, 116–119.

[283] Ito, A.; Li, D.; Lee, Y.; Kobayakawa, K.; Sato, Y. Influence of Co substitution for Ni and Mn on the structural and electrochemical characteristics of $LiNi_{0.5}Mn_{1.5}O_4$. *J. Power Sources* **2008**, *185*, 1429–1433.

[284] Xiao, L.; Zhao, Y.; Yang, Y.; Cao, Y.; Ai, X.; Yang, H. Enhanced electrochemical stability of Al-doped $LiMn_2O_4$ synthesized by a polymer-pyrolysis method. *Electrochim. Acta* **2008**, *54*, 545–550.

[285] Armstrong, A. R.; Bruce, P. G. Synthesis of layered $LiMnO_2$ as an electrode for rechargeable lithium batteries. *Nature* **1996**, *381*, 499–500.

[286] Ji, H.; Yang, G.; Miao, X.; Hong, A. Efficient microwave hydrothermal synthesis of nanocrystalline orthorhombic $LiMnO_2$ cathodes for lithium batteries. *Electrochim. Acta* **2010**, *55*, 3392–3397.

[287] Bruce, P. G.; Armstrong, A. R.; Gitzendanner, R. L. New intercalation compounds for lithium batteries: layered $LiMnO_2$. *J. Mater. Chem.* **1999**, *9*, 193–198.

[288] Xiao, X.; Wang, L.; Wang, D.; He, X.; Peng, Q.; Li, Y. Hydrothermal synthesis of orthorhombic $LiMnO_2$ nano-particles and $LiMnO_2$ nanorods and comparison of their electrochemical performances. *Nano Res.* **2010**, *2*, 923–930.

[289] Ren, Y.; Armstrong, A. R.; Jiao, F.; Bruce, P. G. Influence of size on the rate of mesoporous electrodes for lithium batteries. *J. Am. Chem. Soc.* **2010**, *132*, 996–1004.

[290] Liu, Q.; Li, Y.; Hu, Z.; Mao, D.; Chang, C.; Huang, F. One-step hydrothermal routine for pure-phased orthorhombic $LiMnO_2$ for Li ion battery application. *Electrochim. Acta* **2008**, *53*, 7298–7302.

[291] He, Y.; Li, R.; Ding, X.; Jiang, L.; Wei, M. Hydrothermal synthesis and electrochemical properties of orthorhombic $LiMnO_2$ nanoplates. *J. Alloys Compd.* **2010**, *492*, 601–604.

[292] Liu, J.; Manthiram, A. Understanding the improved electrochemical performances of Fe-substituted 5 V spinel cathode $LiMn_{1.5}Ni_{0.5}O_4$. *J. Phys. Chem. C* **2009**, *113*, 15073–15079.

[293] Wang, H.; Xia, H.; Lai, M. O.; Lu, L. Enhancements of rate capability and cyclic performance of spinel $LiNi_{0.5}Mn_{1.5}O_4$ by trace Ru-doping. *Electrochem. Commun.* **2009**, *11*, 1539–1542.

[294] Patoux, S.; Sannier, L.; Lignier, H.; Reynier, Y.; Bourbon, C.; Jouanneau, S.; Le Cras, F.; Martinet, S. High voltage nickel manganese spinel oxides for Li-ion batteries. *Electrochim. Acta* **2008**, *53*, 4137–4145.

[295] Yi, T.-F.; Zhu, Y.-R. Synthesis and electrochemistry of 5V $LiNi_{0.4}Mn_{1.6}O_4$ cathode materials synthesized by different methods. *Electrochim. Acta* **2008**, *53*, 3120–3126.

[296] Kim, M. G.; Jo, M.; Hong, Y.-S.; Cho, J. Template-free synthesis of $Li[Ni_{0.25}Li_{0.15}Mn_{0.6}]O_2$ nanowires for high performance lithium battery cathode. *Chem. Commun.* **2009**, 218–220.

[297] Wu, H. M.; Belharouak, I.; Abouimrane, A.; Sun, Y.-K.; Amine, K. Surface modification of $LiNi_{0.5}Mn_{1.5}O_4$ by ZrP_2O_7 and ZrO_2 for lithium-ion batteries. *J. Power Sources* **2010**, *195*, 2909–2913.

[298] Arrebola, J. C.; Caballero, A.; Hernán, L.; Morales, J. A high energy Li-ion battery based on nanosized $LiNi_{0.5}Mn_{1.5}O_4$ cathode material. *J. Power Sources* **2008**, *183*, 310–315.

[299] Santhanam, R.; Rambabu, B. Research progress in high voltage spinel $LiNi_{0.5}Mn_{1.5}O_4$ material. *J. Power Sources* **2010**, *195*, 5442–5451.

[300] Arunkumar, T. A.; Manthiram, A. Influence of lattice parameter differences on the electrochemical performance of the 5 V spinel $LiMn_{1.5-y}Ni_{0.5}M_{y+z}O_4$ (M = Li, Mg, Fe, Co, and Zn). *Electrochem. Solid-State Lett.* **2005**, *8*, A403–A405.

[301] Liu, J.; Manthiram, A. Improved electrochemical performance of the 5 V spinel cathode $LiMn_{1.5}Ni_{0.42}Zn_{0.08}O_4$ by surface modification. *J. Electrochem. Soc.* **2009**, *156*, A66–A72.

[302] Aklalouch, M.; Amarilla, J. M.; Rojas, R. M.; Saadoune, I.; Rojo, J. M. Chromium doping as a new approach to improve the cycling performance at high temperature of 5V $LiNi_{0.5}Mn_{1.5}O_4$-based positive electrode. *J. Power Sources* **2008**, *185*, 501–511.

[303] Liu, J.; Manthiram, A. Understanding the improvement in the electrochemical properties of surface modified 5 V $LiMn_{1.42}Ni_{0.42}Co_{0.16}O_4$ spinel cathodes in lithium-ion cells. *Chem. Mater.* **2009**, *21*, 1695–1707.

[304] Hassoun, J.; Lee, K.-S.; Sun, Y.-K.; Scrosati, B. An advanced lithium ion battery based on high performance electrode materials. *J. Am. Chem. Soc.* **2011**, *133*, 3139–3143.

[305] Hu, S.-K.; Cheng, G.-H.; Cheng, M.-Y.; Hwang, B.-J.; Santhanam, R. Cycle life improvement of ZrO_2-coated spherical $LiNi_{1/3}Co_{1/3}Mn_{1/3}O_2$ cathode material for lithium ion batteries. *J. Power Sources* **2009**, *188*, 564–569.

[306] Lin, B.; Wen, Z.; Gu, Z.; Huang, S. Morphology and electrochemical performance of $Li[Ni_{1/3}Co_{1/3}Mn_{1/3}]O_2$ cathode material by a slurry spray drying method. *J. Power Sources* **2008**, *175*, 564–569.

[307] Yabuuchi, N.; Yoshii, K.; Myung, S.-T.; Nakai, I.; Komaba, S. Detailed studies of a high-capacity electrode material for rechargeable batteries, Li_2MnO_3–$LiCo_{1/3}Ni_{1/3}Mn_{1/3}O_2$. *J. Am. Chem. Soc.* **2011**, *133*, 4404–4419.

[308] Martha, S. K.; Sclar, H.; Szmuk Framowitz, Z.; Kovacheva, D.; Saliyski, N.; Gofer, Y.; Sharon, P.; Golik, E.; Markovsky, B.; Aurbach, D. A comparative study of electrodes comprising nanometric and submicron particles of $LiNi_{0.50}Mn_{0.50}O_2$, $LiNi_{0.33}Mn_{0.33}Co_{0.33}O_2$, and $LiNi_{0.40}Mn_{0.40}Co_{0.20}O_2$ layered compounds. *J. Power Sources* **2009**, *189*, 248–255.

[309] Park, S.-H.; Kang, S.-H.; Belharouak, I.; Sun, Y. K.; Amine, K. Physical and electrochemical properties of spherical $Li_{1+x}(Ni_{1/3}Co_{1/3}Mn_{1/3})_{1-x}O_2$ cathode materials. *J. Power Sources* **2008**, *177*, 177–183.

[310] Guo, R.; Shi, P.; Cheng, X.; Du, C. Synthesis and characterization of carbon-coated $LiNi_{1/3}Co_{1/3}Mn_{1/3}O_2$ cathode material prepared by polyvinyl alcohol pyrolysis route. *J. Alloys Compd.* **2009**, *473*, 53–59.

[311] Huang, Y.; Chen, J.; Ni, J.; Zhou, H.; Zhang, X. A modified ZrO_2-coating process to improve

electrochemical performance of $Li(Ni_{1/3}Co_{1/3}Mn_{1/3})O_2$. *J. Power Sources* **2009**, *188*, 538–545.

[312] Santhanam, R.; Rambabu, B. High rate cycling performance of $Li_{1.05}Ni_{1/3}Co_{1/3}Mn_{1/3}O_2$ materials prepared by sol–gel and co-precipitation methods for lithium-ion batteries. *J. Power Sources* **2010**, *195*, 4313–4317.

[313] Jiang, M.; Key, B.; Meng, Y. S.; Grey, C. P. Electrochemical and structural sudy of the layered, "Li-excess" lithium-ion battery electrode material $Li[Li_{1/9}Ni_{1/3}Mn_{5/9}]O_2$. *Chem. Mater.* **2009**, *21*, 2733–2745.

[314 Wei, G.-Z.; Lu, X.; Ke, F.-S.; Huang, L.; Li, J.-T.; Wang, Z.-X.; Zhou, Z.-Y.; Sun, S.-G. Crystal habit-tuned nanoplate material of $Li[Li_{1/3-2x/3}Ni_xMn_{2/3-x/3}]O_2$ for high-rate performance lithium-ion batteries. *Adv. Mater.* **2010**, *22*, 4364–4367.

[315] Ito, A.; Li, D.; Sato, Y.; Arao, M.; Watanabe, M.; Hatano, M.; Horie, H.; Ohsawa, Y. Cyclic deterioration and its improvement for Li-rich layered cathode material $Li[Ni_{0.17}Li_{0.2}Co_{0.07}Mn_{0.56}]O_2$. *J. Power Sources* **2010**, *195*, 567–573.

[316] O'Dwyer, C.; Lavayen, V.; Newcomb, S. B.; Santa Ana, M. A.; Benavente, E.; González, G.; Sotomayor Torres, C. M. Vanadate conformation variations in vanadium pentoxide nanostructures. *J. Electrochem. Soc.* **2007**, *154*, K29–K35.

[317] Wang, Y.; Cao, G. Synthesis and enhanced intercalation properties of nanostructured vanadium oxides. *Chem. Mater.* **2006**, *18*, 2787–2804.

[318] Delmas, C.; Cognacauradou, H.; Cocciantelli, J.; Ménétrier, M.; Doumerc, J. The $Li_xV_2O_5$ system: An overview of the structure modifications induced by the lithium intercalation. *Solid State Ionics* **1994**, *69*, 257–264.

[319] Cocciantelli, J. M.; Ménétrier, M.; Delmas, C.; Doumerc, J. P.; Pouchard, M.; Broussely, M.; Labat, J. On the $\delta \rightarrow \gamma$ irreversible transformation in $Li//V_2O_5$ secondary batteries. *Solid State Ionics* **1995**, *78*, 143–150.

[320] Leger, C.; Bach, S.; Soudan, P.; Pereira-Ramos, J.-P. Structural and electrochemical properties of ω-$Li_xV_2O_5$ ($0.4 \leq x \leq 3$) as rechargeable cathodic material for lithium batteries. *J. Electrochem. Soc.* **2005**, *152*, A236–A241.

[321] Chan, C. K.; Peng, H.; Twesten, R. D.; Jarausch, K.; Zhang, X. F.; Cui, Y. Fast, completely reversible Li insertion in vanadium pentoxide nanoribbons. *Nano Lett.* **2007**, *7*, 490–495.

[322] Murphy, D.; Christian, P. Lithium incorporation by vanadium pentoxide. *Inorg. Chem.* **1979**, *18*, 2800–2803

[323] Pan, A.; Zhang, J.-G.; Nie, Z.; Cao, G.; Arey, B. W.; Li, G.; Liang, S.; Liu, J. Facile synthesized nanorod structured vanadium pentoxide for high-rate lithium batteries. *J. Mater. Chem.* **2010**, *20*, 9193–9199.

[324] Reddy, C. V. S.; Wicker, S. A.; Walker, E. H.; Williams, Q. L.; Kalluru, R. R. Vanadium oxide nanorods for Li-ion battery applications. *J. Electrochem. Soc.* **2008**, *155*, A599–A602.

[325] Zhai, T.; Liu, H.; Li, H.; Fang, X.; Liao, M.; Li, L.; Zhou, H.; Koide, Y.; Bando, Y.; Golberg, D. Centimeter-long V_2O_5 nanowires: From synthesis to field-emission, electrochemical, electrical transport, and photoconductive properties. *Adv. Mater.* **2010**, *22*, 2547–2552.

[326] Yu, D.; Chen, C.; Xie, S.; Liu, Y.; Park, K.; Zhou, X.; Zhang, Q.; Li, J.; Cao, G. Mesoporous vanadium pentoxide nanofibers with significantly enhanced Li-ion storage properties by electrospinning. *Energy Environ. Sci.* **2011**, *4*, 858–861.

[327] Liu, H.; Yang, W. Ultralong single crystalline V_2O_5 nanowire/graphene composite fabricated by a facile green approach and its lithium storage behavior. *Energy Environ. Sci.* **2011**, *4*, 4000–4008.

[328] Cheah, Y. L.; Gupta, N.; Pramana, S. S.; Aravindan, V.; Wee, G.; Srinivasan, M. Morphology, structure and electrochemical properties of single phase electrospun vanadium pentoxide nanofibers for lithium ion batteries. *J. Power Sources* **2011**, *196*, 6465–6472.

[329] Mai, L.; Xu, L.; Han, C.; Xu, X.; Luo, Y.; Zhao, S.; Zhao, Y. Electrospun ultralong hierarchical vanadium oxide nanowires with high performance for lithium ion batteries. *Nano Lett.* **2010**, *10*, 4750–4755.

[330] Cheah, Y. L.; Aravindan, V.; Madhavi, S. Improved elevated temperature performance of Al-intercalated V_2O_5 electrospun nanofibers for lithium-ion batteries. *ACS Appl. Mater. Interfaces* **2012**, *4*, 3270–3277.

[331] Wang, H.-G.; Ma, D.-L.; Huang, Y.; Zhang, X.-B. Electrospun V_2O_5 nanostructures with controllable morphology as high-performance cathode materials for lithium-ion batteries. *Chem. Eur. J.* **2012**, *18*, 8987–8993.

[332] Ban, C.; Chernova, N. A.; Whittingham, M. S. Electrospun nano-vanadium pentoxide cathode. *Electrochem. Commun.* **2009**, *11*, 522–525.

[333] Armstrong, G.; Canales, J.; Armstrong, A. R.; Bruce, P. G. The synthesis and lithium intercalation electrochemistry of VO_2(B) ultra-thin nanowires. *J. Power Sources* **2008**, *178*, 723–728.

[334] Wang, Y.; Zhang, H. J.; Lim, W. X.; Lin, J. Y.; Wong, C. C. Designed strategy to fabricate a patterned V_2O_5 nanobelt array as a superior electrode for Li-ion batteries. *J. Mater. Chem.* **2011**, *21*, 2362–2368.

[335] Wang, Y.; Zhang, H. J.; Siah, K. W.; Wong, C. C.; Lin, J.; Borgna, A. One pot synthesis of self-assembled V_2O_5 nanobelt membrane via capsule-like hydrated precursor as improved cathode for Li-ion battery. *J. Mater. Chem.* **2011**, *21*, 10336–10341.

[336] Ragupathy, P.; Shivakumara, S.; Vasan, H. N.; Munichandraiah, N. Preparation of nanostrip V_2O_5 by the polyol method and its electrochemical characterization as cathode material for rechargeable lithium batteries. *J. Phys. Chem. C* **2008**, *112*, 16700–16707.

[337] Rui, X.; Zhu, J.; Liu, W.; Tan, H.; Sim, D.; Xu, C.; Zhang, H.; Ma, J.; Hng, H. H.; Lim, T. M. et al. Facile preparation of hydrated vanadium pentoxide nanobelts based bulky paper as flexible binder-free cathodes for high-performance lithium ion batteries. *RSC Adv.* **2011**, *1*, 117–122.

[338] Mohan, V. M.; Hu, B.; Qiu, W.; Chen, W. Synthesis, structural, and electrochemical performance of V_2O_5 nanotubes as cathode material for lithium battery. *J. Appl. Electrochem.* **2009**, *39*, 2001–2006.

[339] O'Dwyer, C.; Lavayen, V.; Newcomb, S. B.; Benavente, E.; Santa Ana, M. A.; González, G.; Sotomayor Torres, C. M. Atomic layer structure of vanadium oxide nanotubes grown on nanourchin structures. *Electrochem. Solid-State Lett.* **2007**, *10*, A111–A114.

[340] Zhang, X.-F.; Wang, K.-X.; Wei, X.; Chen, J.-S. Carbon-coated V_2O_5 nanocrystals as high performance cathode material for lithium ion batteries. *Chem. Mater.* **2011**, *23*, 5290–5292.

[341] Wang, S.; Lu, Z.; Wang, D.; Li, C.; Chen, C.; Yin, Y. Porous monodisperse V_2O_5 microspheres as cathode materials for lithium-ion batteries. *J. Mater. Chem.* **2011**, *21*, 6365–6369.

[342] Sasidharan, M.; Gunawardhana, N.; Yoshio, M.; Nakashima, K. V_2O_5 hollow nanospheres: A lithium intercalation host with good rate capability and capacity retention. *J. Electrochem. Soc.* **2012**, *159*, A618–A621.

[343] Liu, J.; Xia, H.; Xue, D.; Lu, L. Double-shelled nanocapsules of V_2O_5-based composites as high-performance anode and cathode materials for Li ion batteries. *J. Am. Chem. Soc.* **2009**, *131*, 12086–12087.

[344] O'Dwyer, C.; Navas, D.; Lavayen, V.; Benavente, E.; Santa Ana, M. A.; González, G.; Newcomb, S. B.; Sotomayor Torres, C. M. Nano-urchin: The formation and structure of high-density spherical clusters of vanadium oxide nanotubes. *Chem. Mater.* **2006**, *18*, 3016–3022.

[345] Lavayen, V.; O'Dwyer, C.; Santa Ana, M. A.; Newcomb, S. B.; Benavente, E.; González, G.; Sotomayor Torres, C. M. Comparative structural–vibrational study of nano-urchin and nanorods of vanadium oxide. *Phys. Status Solidi B* **2006**, *243*, 3285–3289.

[346] Lee, J.-K.; Kim, G.-P.; Song, I. K.; Baeck, S.-H. Electrodeposition of mesoporous V_2O_5 with enhanced lithium-ion intercalation property. *Electrochem. Commun.* **2009**, *11*, 1571–1574.

[347] Wang, S.; Li, S.; Sun, Y.; Feng, X.; Chen, C. Three-dimensional porous V_2O_5 cathode with ultra high rate capability. *Energy Environ. Sci.* **2011**, *4*, 2854–2857.

[348] Hu, Y.-S.; Liu, X.; Müller, J.-O.; Schlögl, R.; Maier, J.; Su, D. S. Synthesis and electrode performance of nanostructured V_2O_5 by using a carbon tube-in-tube as a nanoreactor and an efficient mixed-conducting network. *Angew. Chem. Int. Edit.* **2009**, *48*, 210–214.

[349] Sathiya, M.; Prakash, a S.; Ramesha, K.; Tarascon, J. M.; Shukla, A. K. V_2O_5-anchored carbon nanotubes for enhanced electrochemical energy storage. *J. Am. Chem. Soc.* **2011**, *133*, 16291–16299.

[350] Du, G.; Seng, K. H.; Guo, Z.; Liu, J.; Li, W.; Jia, D.; Cook, C.; Liu, Z.; Liu, H. Graphene–V_2O_5·nH_2O xerogel composite cathodes for lithium ion batteries. *RSC Adv.* **2011**, *1*, 690–697.

[351] Liu, D.; Liu, Y.; Pan, A.; Nagle, K. P.; Seidler, G. T.; Jeong, Y.-H.; Cao, G. Enhanced lithium-ion intercalation properties of V_2O_5 xerogel electrodes with surface defects. *J. Phys. Chem. C* **2011**, *115*, 4959–4965.

[352] Liu, Y.; Clark, M.; Zhang, Q.; Yu, D.; Liu, D.; Liu, J.; Cao, G. V_2O_5 nano-electrodes with high power and energy densities for thin film Li-ion batteries. *Adv. Energy Mater.* **2011**, *1*, 194–202.

[353] Dewangan, K.; Sinha, N. N.; Chavan, P. G.; Sharma, P. K.; Pandey, A. C.; More, M. A.; Joag, D. S.; Munichandraiah, N.; Gajbhiye, N. S. Synthesis and characterization of self-assembled nanofiber-bundles of V_2O_5: Their electrochemical and field emission properties. *Nanoscale* **2012**, *4*, 645–651.

[354] Seng, K. H.; Liu, J.; Guo, Z. P.; Chen, Z. X.; Jia, D.; Liu, H. K. Free-standing V_2O_5 electrode for flexible lithium ion batteries. *Electrochem. Commun.* **2011**, *13*, 383–386.

[355] Li, D.; Xia, Y. Electrospinning of nanofibers: Reinventing the wheel? *Adv. Mater.* **2004**, *16*, 1151–1170.

[356] Greiner, A.; Wendorff, J. H. Electrospinning: A fascinating method for the preparation of ultrathin fibers. *Angew. Chem. Int. Edit.* **2007**, *46*, 5670–703.

[357] Cao, J.; Choi, J.; Musfeldt, J. Effect of sheet distance on the optical properties of vanadate nanotubes. *Chem. Mater.* **2004**, *16*, 731–736.

[358] Petkov, V.; Zavalij, P.; Lutta, S.; Whittingham, M.; Parvanov, V.; Shastri, S. Structure beyond Bragg: Study of V_2O_5 nanotubes. *Phys. Rev. B* **2004**, *69*, 085410.

[359] O'Dwyer, C.; Lavayen, V.; Tanner, D. A.; Newcomb, S. B.; Benavente, E.; González, G.; Torres, C. M. S. Reduced surfactant uptake in three dimensional assemblies of VO_x nanotubes improves reversible Li^+ intercalation and charge capacity. *Adv. Funct. Mater.* **2009**, *19*, 1736–1745.

[360] Livage, J. Vanadium pentoxide gels. *Chem. Mater.* **1991**, *3*, 578–593.

[361] Zhang, X.-F.; Wang, K.-X.; Wei, X.; Chen, J.-S. Carbon-coated V_2O_5 nanocrystals as high performance cathode material for lithium ion batteries. *Chem. Mater.* **2011**, *23*, 5290–5292.

[362] Wadsley, A. D. Crystal chemistry of non-stoichiometric pentavalent vandadium oxides: Crystal structure of $Li_{1+x}V_3O_8$. *Acta Crystallogr.* **1957**, *10*, 261–267.

[363] Pan, A.; Liu, J.; Zhang, J.-G.; Cao, G.; Xu, W.; Nie, Z.; Jie, X.; Choi, D.; Arey, B. W.; Wang, C. et al. Template free synthesis of LiV_3O_8 nanorods as a cathode material for high-rate secondary lithium batteries. *J. Mater. Chem.* **2011**, *21*, 1153–1161.

[364] Sakunthala, A.; Reddy, M.; Selvasekarapandian, S.; Chowdari, B.; Selvin, P. C. Preparation, characterization, and electrochemical performance of lithium trivanadate rods by a surfactant-assisted polymer precursor method for lithium batteries. *J. Phys. Chem. C* **2010**, *114*, 8099–8107.

[365] Ju, S. H.; Kang, Y. C. Morphological and electrochemical properties of LiV_3O_8 cathode powders prepared by spray pyrolysis. *Electrochim. Acta* **2010**, *55*, 6088–6092.

[366] Liu, H.; Wang, Y.; Wang, K.; Wang, Y.; Zhou, H. Synthesis and electrochemical properties of single-crystalline LiV_3O_8 nanorods as cathode materials for rechargeable lithium batteries. *J. Power Sources* **2009**, *192*, 668–673.

[367] Qiao, Y. Q.; Wang, X. L.; Zhou, J. P.; Zhang, J.; Gu, C. D.; Tu, J. P. Synthesis and electrochemical performance of rod-like LiV_3O_8 cathode materials for rechargeable lithium batteries. *J. Power Sources* **2012**, *198*, 287–293.

[368] Shi, Q.; Liu, J.; Hu, R.; Zeng, M.; Dai, M.; Zhu, M. An amorphous wrapped nanorod LiV_3O_8 electrode with enhanced performance for lithium ion batteries. *RSC Adv.* **2012**, *2*, 7273–7278.

[369] Xu, X.; Luo, Y.-Z.; Mai, L.-Q.; Zhao, Y.-L.; An, Q.-Y.; Xu, L.; Hu, F.; Zhang, L.; Zhang, Q.-J. Topotactically synthesized ultralong LiV_3O_8 nanowire cathode materials for high-rate and long-life rechargeable lithium batteries. *NPG Asia Mater.* **2012**, *4*, e20.

[370] Wang, H.; Ren, Y.; Wang, Y.; Wang, W.; Liu, S. Synthesis of LiV_3O_8 nanosheets as a high-rate cathode material for rechargeable lithium batteries. *CrystEngComm* **2012**, *14*, 2831–2836.

[371] Pan, A.; Zhang, J.-G.; Cao, G.; Liang, S.; Wang, C.; Nie, Z.; Arey, B. W.; Xu, W.; Liu, D.; Xiao, J.; Li, G.; Liu, J. Nanosheet-structured LiV_3O_8 with high capacity and excellent stability for high energy lithium batteries. *J. Mater. Chem.* **2011**, *21*, 10077–10084.

[372] Patey, T. J.; Ng, S. H.; Buˇchel, R.; Tran, N.; Krumeich, F.; Wang, J.; Liu, H. K.; Novák, P. Electrochemistry of LiV_3O_8 nanoparticles made by flame spray pyrolysis. *Electrochem. Solid-State Lett.* **2008**, *11*, A46–A50.

[373] Padhi, A. K. Phospho-olivines as positive-electrode materials for rechargeable lithium batteries. *J. Electrochem. Soc.* **1997**, *144*, 1188–1194.

[374] Wang, Y.; He, P.; Zhou, H. Olivine $LiFePO_4$: Development and future. *Energy Environ. Sci.* **2011**, *4*, 805–817.

[375] Zhang, W.-J. Structure and performance of $LiFePO_4$ cathode materials: A review. *J. Power Sources* **2011**, *196*, 2962–2970.

[376] Li, Z.; Zhang, D.; Yang, F. Developments of lithium-ion batteries and challenges of $LiFePO_4$ as one promising cathode material. *J. Mater. Sci.* **2009**, *44*, 2435–2443.

[377] Kang, B.; Ceder, G. Battery materials for ultrafast charging and discharging. *Nature* **2009**, *458*, 190–193.

[378] Gong, Z.; Yang, Y. Recent advances in the research of polyanion-type cathode materials for Li-ion batteries. *Energy Environ. Sci.* **2011**, *4*, 3223–3242.

[379] Bhuvaneswari, M. S.; Bramnik, N. N.; Ensling, D.; Ehrenberg, H.; Jaegermann, W. Synthesis and characterization of carbon nano fiber/$LiFePO_4$ composites for Li-ion batteries. *J. Power Sources* **2008**, *180*, 553–560.

[380] Konarova, M.; Taniguchi, I. Synthesis of carbon-coated $LiFePO_4$ nanoparticles with high rate performance in lithium secondary batteries. *J. Power Sources* **2010**, *195*, 3661–3667.

[381] Doherty, C. M.; Caruso, R. A.; Smarsly, B. M.; Adelhelm, P.; Drummond, C. J. Hierarchically porous monolithic $LiFePO_4$/carbon composite electrode materials for high power lithium ion batteries. *Chem. Mater.* **2009**, *21*, 5300–5306.

[382] Lu, C.; Fey, G.; Kao, H. Study of $LiFePO_4$ cathode materials coated with high surface area carbon. *J. Power Sources* **2009**, *189*, 155–162.

[383] Zhao, B.; Jiang, Y.; Zhang, H.; Tao, H.; Zhong, M.; Jiao, Z. Morphology and electrical properties of carbon coated $LiFePO_4$ cathode materials. *J. Power Sources* **2009**, *189*, 462–466.

[384] Wang, Y.; Wang, Y.; Hosono, E.; Wang, K.; Zhou, H. The design of a $LiFePO_4$/carbon nanocomposite with a core–shell structure and its synthesis by an in situ polymerization restriction method. *Angew. Chem. Int. Edit.* **2008**, *47*, 7461–7465.

[385] Chen, J.-M.; Hsu, C.-H.; Lin, Y.-R.; Hsiao, M.-H.; Fey, G. T.-K. High-power $LiFePO_4$ cathode materials with a continuous nano carbon network for lithium-ion batteries. *J. Power Sources* **2008**, *184*, 498–502.

[386] Ferrari, S.; Lavall, R. L.; Capsoni, D.; Quartarone, E.; Magistris, A.; Mustarelli, P.; Canton, P. Influence of particle size and crystal orientation on the electrochemical behavior of carbon-coated $LiFePO_4$. *J. Phys. Chem. C* **2010**, *114*, 12598–12603.

[387] Joachin, H.; Kaun, T. D.; Zaghib, K.; Prakash, J. Electrochemical and thermal studies of carbon-coated $LiFePO_4$ cathode. *J. Electrochem. Soc.* **2009**, *156*, A401–A406.

[388] Muraliganth, T.; Murugan, A. V.; Manthiram, A. Nanoscale networking of $LiFePO_4$ nanorods synthesized by a microwave-solvothermal route with carbon nanotubes for lithium ion batteries. *J. Mater. Chem.* **2008**, *18*, 5661–5668.

[389] Kuwahara, A.; Suzuki, S.; Miyayama, M. High-rate properties of $LiFePO_4$/carbon composites as cathode materials for lithium-ion batteries. *Ceram. Int.* **2008**, *34*, 863–866.

[390] Cho, Y.-D.; Fey, G. T.-K.; Kao, H.-M. The effect of carbon coating thickness on the capacity of $LiFePO_4$/C composite cathodes. *J. Power Sources* **2009**, *189*, 256–262.

[391] Wu, X.-L.; Jiang, L.-Y.; Cao, F.-F.; Guo, Y.-G.; Wan, L.-J. $LiFePO_4$ nanoparticles embedded in a nanoporous carbon matrix: Superior cathode material for electrochemical energy-storage devices. *Adv. Mater.* **2009**, *21*, 2710–2714.

[392] Zhu, C.; Yu, Y.; Gu, L.; Weichert, K.; Maier, J. Electrospinning of highly electroactive carbon-coated single-crystalline $LiFePO_4$ nanowires. *Angew. Chem. Int. Edit.* **2011**, *50*, 6278–6282.

[393] Liu, Y.; Cao, C.; Li, J. Enhanced electrochemical performance of carbon nanospheres–$LiFePO_4$ composite by PEG based sol–gel synthesis. *Electrochim. Acta* **2010**, *55*, 3921–3926.

[394] Wang, K.; Cai, R.; Yuan, T.; Yu, X.; Ran, R.; Shao, Z. Process investigation, electrochemical characterization and optimization of $LiFePO_4$/C composite from mechanical activation using sucrose as carbon source. *Electrochim. Acta* **2009**, *54*, 2861–2868.

[395] Chen, Z.; Zhu, H.; Ji, S.; Fakir, R.; Linkov, V. Influence of carbon sources on electrochemical performances of $LiFePO_4$/C composites. *Solid State Ionics* **2008**, *179*, 1810–1815.

[396] Dong, Y. Z.; Zhao, Y. M.; Chen, Y. H.; He, Z. F.; Kuang, Q. Optimized carbon-coated $LiFePO_4$ cathode material for lithium-ion batteries. *Mater. Chem. Phys.* **2009**, *115*, 245–250.

[397] Kim, J.-K.; Cheruvally, G.; Ahn, J.-H.; Hwang, G.-C.; Choi, J.-B. Electrochemical properties of carbon-coated $LiFePO_4$ synthesized by a modified mechanical activation process. *J. Phys. Chem. Solids* **2008**, *69*, 2371–2377.

[398] Zhang, Y.; Feng, H.; Wu, X.; Wang, L.; Zhang, A.; Xia, T.; Dong, H.; Liu, M. One-step microwave synthesis and characterization of carbon-modified nanocrystalline $LiFePO_4$. *Electrochim. Acta* **2009**, *54*, 3206–3210.

[399] Zhou, Y.; Wang, J.; Hu, Y.; O'Hayre, R.; Shao, Z. A porous $LiFePO_4$ and carbon nanotube composite. *Chem. Commun.* **2010**, *46*, 7151–7153.

[400] Liu, Y.; Li, X.; Guo, H.; Wang, Z.; Peng, W.; Yang, Y.; Liang, R. Effect of carbon nanotube on the electrochemical performance of C-$LiFePO_4$/graphite battery. *J. Power Sources* **2008**, *184*, 522–526.

[401] Liu, H.; Tang, D. The low cost synthesis of nanoparticles $LiFePO_4$/C composite for lithium rechargeable batteries. *Solid State Ionics* **2008**, *179*, 1897–1901.

[402] Saravanan, K.; Balaya, P.; Reddy, M. V.; Chowdari, B. V. R.; Vittal, J. J. Morphology controlled synthesis of $LiFePO_4$/C nanoplates for Li-ion batteries. *Energy Environ. Sci.* **2010**, *3*, 457–464.

[403] Murugan, A. V.; Muraliganth, T.; Manthiram, A. Comparison of microwave assisted solvothermal and hydrothermal syntheses of $LiFePO_4$/C nanocomposite cathodes for lithium ion batteries. *J. Phys. Chem. C* **2008**, *112*, 14665–14671.

[404] Kadoma, Y.; Kim, J.-M.; Abiko, K.; Ohtsuki, K.; Ui, K.; Kumagai, N. Optimization of electrochemical properties of $LiFePO_4$/C prepared by an aqueous solution method using sucrose. *Electrochim. Acta* **2010**, *55*, 1034–1041.

[405] Yan, X.; Yang, G.; Liu, J.; Ge, Y.; Xie, H.; Pan, X.; Wang, R. An effective and simple way to synthesize $LiFePO_4$/C composite. *Electrochim. Acta* **2009**, *54*, 5770–5774.

[406] Wang, G.; Liu, H.; Liu, J.; Qiao, S.; Lu, G. M.; Munroe, P.; Ahn, H. Mesoporous $LiFePO_4$/C nanocomposite cathode materials for high power lithium ion batteries with superior performance. *Adv. Mater.* **2010**, *22*, 4944–4948.

[407] Yu, F.; Zhang, J.; Yang, Y.; Song, G. Preparation and characterization of mesoporous $LiFePO_4$/C microsphere by spray drying assisted template method. *J. Power Sources* **2009**, *189*, 794–797.

[408] Yu, F.; Zhang, J.-J.; Yang, Y.-F.; Song, G.-Z. Up-scalable synthesis, structure and charge storage properties of porous microspheres of $LiFePO_4$@C nanocomposites. *J. Mater. Chem.* **2009**, *19*, 9121–1925.

[409] Huang, Y.; Ren, H.; Yin, S.; Wang, Y.; Peng, Z.; Zhou, Y. Synthesis of $LiFePO_4$/C composite with high-rate performance by starch sol assisted rheological phase method. *J. Power Sources* **2010**, *195*, 610–613.

[410] Chang, Z.-R.; Lv, H.-J.; Tang, H.-W.; Li, H.-J.; Yuan, X.-Z.; Wang, H. Synthesis and characterization of high-density $LiFePO_4$/C composites as cathode materials for lithium-ion batteries. *Electrochim. Acta* **2009**, *54*, 4595–4599.

[411] Gao, F.; Tang, Z. Kinetic behavior of $LiFePO_4$/C cathode material for lithium-ion batteries. *Electrochim. Acta* **2008**, *53*, 5071–5075.

[412] Wang, Y.; Yang, Y.; Hu, X.; Yang, Y.; Shao, H. Electrochemical performance of Ru-doped $LiFePO_4$/C cathode material for lithium-ion batteries. *J. Alloys Compd.* **2009**, *481*, 590–594.

[413] Beninati, S.; Damen, L.; Mastragostino, M. Fast sol–gel synthesis of $LiFePO_4$/C for high power lithium-ion batteries for hybrid electric vehicle application. *J. Power Sources* **2009**, *194*, 1094–1098.

[414] Sun, C. S.; Zhou, Z.; Xu, Z. G.; Wang, D. G.; Wei, J. P.; Bian, X. K.; Yan, J. Improved high-rate charge/discharge performances of $LiFePO_4$/C via V-doping. *J. Power Sources* **2009**, *193*, 841–845.

[415] Yu, F.; Zhang, J.; Yang, Y.; Song, G. Porous micro-spherical aggregates of $LiFePO_4$/C nanocomposites: A novel and simple template-free concept and synthesis via sol–gel-spray drying method. *J. Power Sources* **2010**, *195*, 6873–6878.

[416] Oh, S. W.; Myung, S.-T.; Oh, S.-M.; Oh, K. H.; Amine, K.; Scrosati, B.; Sun, Y.-K. Double carbon coating of $LiFePO_4$ as high rate electrode for rechargeable lithium batteries. *Adv. Mater.* **2010**, *22*, 4842–4845.

[417] Lai, C.; Xu, Q.; Ge, H.; Zhou, G.; Xie, J. Improved electrochemical performance of $LiFePO_4$/C for lithium-ion batteries with two kinds of carbon sources. *Solid State Ionics* **2008**, *179*, 1736–1739.

[418] Liu, J.; Wang, J.; Yan, X.; Zhang, X.; Yang, G.; Jalbout, A. F.; Wang, R. Long-term cyclability of $LiFePO_4$/carbon composite cathode material for lithium-ion battery applications. *Electrochim. Acta* **2009**, *54*, 5656–5659.

[419] Jin, B.; Gu, H.-B.; Zhang, W.; Park, K.-H.; Sun, G. Effect of different carbon conductive additives on electrochemical properties of $LiFePO_4$–C/Li batteries. *J. Solid State Electrochem.* **2008**, *12*, 1549–1554.

[420] Wu, Y.; Wen, Z.; Li, J. Hierarchical carbon-coated $LiFePO_4$ nanoplate microspheres with high electrochemical performance for Li-ion batteries. *Adv. Mater.* **2011**, *23*, 1126–1129.

[421] Delmas, C.; Maccario, M.; Croguennec, L.; Le Cras, F.; Weill, F. Lithium deintercalation in $LiFePO_4$ nanoparticles via a domino-cascade model. *Nature materials* **2008**, *7*, 665–671.

[422] Yamada, A.; Koizumi, H.; Nishimura, S.-I.; Sonoyama, N.; Kanno, R.; Yonemura, M.; Nakamura, T.; Kobayashi, Y. Room-temperature miscibility gap in Li_xFePO_4. *Nat. Mater.* **2006**, *5*, 357–360.

[423] Malik, R.; Zhou, F.; Ceder, G. Kinetics of non-equilibrium lithium incorporation in $LiFePO_4$. *Nat. Mater.* **2011**, *10*, 587–590.

[424] Nishimura, S.; Kobayashi, G.; Ohoyama, K.; Kanno, R.; Yashima, M.; Yamada, A. Experimental visualization of lithium diffusion in Li_xFePO_4. *Nat. Mater.* **2008**, *7*, 707–711.

[425] Gibot, P.; Casas-Cabanas, M.; Laffont, L.; Levasseur, S.; Carlach, P.; Hamelet, S.; Tarascon, J.-M.; Masquelier, C. Room-temperature single-phase Li insertion/extraction in nanoscale Li_xFePO_4. *Nat. Mater.* **2008**, *7*, 741–7.

[426] Hosono, E.; Wang, Y.; Kida, N.; Enomoto, M.; Kojima, N.; Okubo, M.; Matsuda, H.; Saito, Y.; Kudo, T.; Honma, I.; Zhou, H. Synthesis of triaxial $LiFePO_4$ nanowire with a VGCF core column and a carbon shell through the electrospinning method. *ACS Appl. Mater. Interfaces* **2010**, *2*, 212–218.

[427] Lim, S.; Yoon, C. S.; Cho, J. Synthesis of nanowire and hollow $LiFePO_4$ cathodes for high-performance lithium batteries. *Chem. Mater.* **2008**, *20*, 4560–4564.

[428] Recham, N.; Dupont, L.; Courty, M.; Djellab, K.; Larcher, D.; Armand, M.; Tarascon, J.-M. Ionothermal synthesis of tailor-made $LiFePO_4$ powders for Li-ion battery applications. *Chem. Mater.* **2009**, *21*, 1096–1107.

[429] Konarova, M.; Taniguchi, I. Physical and electrochemical properties of $LiFePO_4$ nanoparticles synthesized by a combination of spray pyrolysis with wet ball-milling. *J. Power Sources* **2009**, *194*, 1029–1035.

[430] Doherty, C. M.; Caruso, R. A.; Smarsly, B. M.; Drummond, C. J. Colloidal crystal templating to produce hierarchically porous $LiFePO_4$ electrode materials for high power lithium ion batteries. *Chem. Mater.* **2009**, *21*, 2895–2903.

[431] Zheng, J.; Li, X.; Wang, Z.; Guo, H.; Zhou, S. $LiFePO_4$ with enhanced performance synthesized by a novel synthetic route. *J. Power Sources* **2008**, *184*, 574–577.

[432] Qin, X.; Wang, X.; Xiang, H.; Xie, J. Mechanism for hydrothermal synthesis of $LiFePO_4$ platelets as cathode material for lithium-ion batteries. *J. Phys. Chem. C* **2010**, *114*, 16806–16812.

[433] Jin, B.; Gu, H. Preparation and characterization of $LiFePO_4$ cathode materials by hydrothermal method. *Solid State Ionics* **2008**, *178*, 1907–1914.

[434] Yang, H.; Wu, X.-L.; Cao, M.-H.; Guo, Y.-G. Solvothermal synthesis of $LiFePO_4$ hierarchically dumbbell-like microstructures by nanoplate self-assembly and their application as a cathode material in lithium-ion batteries. *J. Phys. Chem. C* **2009**, *113*, 3345–3351.

[435] Liu, H.; Yang, H.; Li, J. A novel method for preparing $LiFePO_4$ nanorods as a cathode material for lithium-ion power batteries. *Electrochim. Acta* **2010**, *55*, 1626–1629.

[436] Bilecka, I.; Hintennach, A.; Djerdj, I.; Novák, P.; Niederberger, M. Efficient microwave-assisted synthesis of $LiFePO_4$ mesocrystals with high cycling stability. *J. Mater. Chem.* **2009**, *19*, 5125–5128.

[437] Sun, C.; Rajasekhara, S.; Goodenough, J. B.; Zhou, F. Monodisperse porous $LiFePO_4$ microspheres for a high power Li-ion battery cathode. *J. Am. Chem. Soc.* **2011**, *133*, 2132–2135.

[438] Huang, Y.-H.; Goodenough, J. B. High-rate $LiFePO_4$ lithium rechargeable battery promoted by electrochemically active polymers. *Chem. Mater.* **2008**, *20*, 7237–7241.

[439] Qian, J.; Zhou, M.; Cao, Y.; Ai, X.; Yang, H. Template-free hydrothermal synthesis of nanoembossed mesoporous $LiFePO_4$ microspheres for high-performance lithium-ion batteries. *J. Phys. Chem. C* **2010**, *114*, 3477–3482.

[440] Yang, S.; Zhou, X.; Zhang, J.; Liu, Z. Morphology-controlled solvothermal synthesis of $LiFePO_4$ as a cathode material for lithium-ion batteries. *J. Mater. Chem.* **2010**, *20*, 8086–8091.

[441] Saravanan, K.; Reddy, M. V.; Balaya, P.; Gong, H.; Chowdari, B. V. R.; Vittal, J. J. Storage performance of $LiFePO_4$ nanoplates. *J. Mater. Chem.* **2009**, *19*, 605–610.

[442] Ni, J.; Morishita, M.; Kawabe, Y.; Watada, M.; Takeichi, N.; Sakai, T. Hydrothermal preparation of $LiFePO_4$ nanocrystals mediated by organic acid. *J. Power Sources* **2010**, *195*, 2877–2882.

[443] Zhou, X.; Wang, F.; Zhu, Y.; Liu, Z. Graphene modified $LiFePO_4$ cathode materials for high power lithium ion batteries. *J. Mater. Chem.* **2011**, *21*, 3353–3358.

[444] Liu, H.; Wang, G. X.; Wexler, D.; Wang, J. Z.; Liu, H. K. Electrochemical performance of $LiFePO_4$ cathode material coated with ZrO_2 nanolayer. *Electrochem. Commun.* **2008**, *10*, 165–169.

[445] Malik, R.; Burch, D.; Bazant, M.; Ceder, G. Particle size dependence of the ionic diffusivity. *Nano Lett.* **2010**, *10*, 4123–4127.

[446] Amin, R.; Maier, J.; Balaya, P.; Chen, D. P.; Lin, C. T. Ionic and electronic transport in single crystalline $LiFePO_4$ grown by optical floating zone technique. *Solid State Ionics* **2008**, *179*, 1683–1687.

[447] Oh, S.-M.; Oh, S.-W.; Yoon, C.-S.; Scrosati, B.; Amine, K.; Sun, Y.-K. High-performance carbon–$LiMnPO_4$ nanocomposite cathode for lithium batteries. *Adv. Funct. Mater.* **2010**, *20*, 3260–3265.

[448] Li, G.; Azuma, H.; Tohda, M. $LiMnPO_4$ as the cathode for lithium batteries. *Electrochem. Solid-State Lett.* **2002**, *5*, A135–A137.

[449] Bakenov, Z.; Taniguchi, I. Electrochemical performance of nanocomposite $LiMnPO_4$/C cathode materials for lithium batteries. *Electrochem. Commun.* **2010**, *12*, 75–78.

[450] Fang, H.; Pan, Z.; Li, L.; Yang, Y.; Yan, G.; Li, G.; Wei, S. The possibility of manganese disorder in $LiMnPO_4$ and its effect on the electrochemical activity. *Electrochem. Commun.* **2008**, *10*, 1071–1073.

[451] Vadivel Murugan, A.; Muraliganth, T.; Ferreira, P. J.; Manthiram, A. Dimensionally modulated, single-crystalline $LiMPO_4$ (M = Mn, Fe, Co, and Ni) with nano-thumblike shapes for high-power energy storage. *Inorg. Chem.* **2009**, *48*, 946–52.

[452] Drezen, T.; Kwon, N.-H.; Bowen, P.; Teerlinck, I.; Isono, M.; Exnar, I. Effect of particle size on $LiMnPO_4$ cathodes. *J. Power Sources* **2007**, *174*, 949–953.

[453] Wang, D.; Buqa, H.; Crouzet, M.; Deghenghi, G.; Drezen, T.; Exnar, I.; Kwon, N.-H.; Miners, J. H.; Poletto, L.; Grätzel, M. High-performance, nano-structured $LiMnPO_4$ synthesized via a polyol method. *J. Power Sources* **2009**, *189*, 624–628.

[454] Bakenov, Z.; Taniguchi, I. Physical and electrochemical properties of $LiMnPO_4$/C composite cathode prepared with different conductive carbons. *J. Power Sources* **2010**, *195*, 7445–7451.

[455] Chen, G.; Richardson, T. J. Thermal instability of olivine-type $LiMnPO_4$ cathodes. *J. Power Sources* **2010**, *195*, 1221–1224.

[456] Wang, D.; Ouyang, C.; Drézen, T.; Exnar, I.; Kay, A.; Kwon, N.-H.; Gouerec, P.; Miners, J. H.; Wang, M.; Grätzel, M. Improving the electrochemical activity of $LiMnPO_4$ via Mn-site substitution. *J. Electrochem. Soc.* **2010**, *157*, A225–A229.

[457] Delacourt, C.; Laffont, L.; Bouchet, R.; Wurm, C.; Leriche, J.-B.; Morcrette, M.; Tarascon, J.-M.; Masquelier, C. Toward understanding of electrical limitations (electronic, ionic) in $LiMPO_4$ (M = Fe, Mn) electrode materials. *J. Electrochem. Soc.* **2005**, *152*, A913–A921.

[458] Choi, D.; Wang, D.; Bae, I.-T.; Xiao, J.; Nie, Z.; Wang, W.; Viswanathan, V. V; Lee, Y. J.; Zhang, J.-G.; Graff, G. L. et al. $LiMnPO_4$ nanoplate grown via solid-state reaction in molten hydrocarbon for Li-ion battery cathode. *Nano Lett.* **2010**, *10*, 2799–2805.

[459] Chen, G.; Wilcox, J. D.; Richardson, T. J. Improving the performance of lithium manganese phosphate through divalent cation substitution. *Electrochem. Solid-State Lett.* **2008**, *11*, A190–A194.

[460] Allen, C.; Jia, Q.; Chinnasamy, C. Synthesis, structure and electrochemistry of lithium vanadium phosphate cathode materials. *J. Electrochem. Soc.* **2011**, *158*, 1250–1259.

[461] Yang, Y.; Fang, H.; Zheng, J.; Li, L.; Li, G.; Yan, G. Towards the understanding of poor electrochemical activity of triclinic $LiVOPO_4$: Experimental characterization and theoretical investigations. *Solid State Sci.* **2008**, *10*, 1292–1298.

[462] Azmi, B. M.; Ishihara, T.; Nishiguchi, H.; Takita, Y. $LiVOPO_4$ as a new cathode materials for Li-ion rechargeable battery. *J. Power Sources* **2005**, *146*, 525–528.

[463] Ren, M.; Zhou, Z.; Su, L.; Gao, X. $LiVOPO_4$: A cathode material for 4V lithium ion batteries. *J. Power Sources* **2009**, *189*, 786–789.

[464] Gover, R.; Burns, P.; Bryan, a; Saidi, M.; Swoyer, J.; Barker, J. $LiVPO_4F$: A new active material for safe lithium-ion batteries. *Solid State Ionics* **2006**, *177*, 2635–2638.

[465] Zheng, J.; Zhang, B.; Yang, Z. Novel synthesis of $LiVPO_4F$ cathode material by chemical lithiation and postannealing. *J. Power Sources* **2012**, *202*, 380–383.

[466] Pan, A.; Liu, J.; Zhang, J.-G.; Xu, W.; Cao, G.; Nie, Z.; Arey, B. W.; Liang, S. Nano-structured $Li_3V_2(PO_4)_3$/carbon composite for high-rate lithium-ion batteries. *Electrochem. Commun.* **2010**, *12*, 1674–1677.

[467] Wang, L.; Zhang, L.-C.; Lieberwirth, I.; Xu, H.-W.; Chen, C.-H. A $Li_3V_2(PO_4)_3$/C thin film with high rate capability as a cathode material for lithium-ion batteries. *Electrochem. Commun.* **2010**, *12*, 52–55.

[468] Zhou, X.; Liu, Y.; Guo, Y. Effect of reduction agent on the performance of $Li_3V_2(PO_4)_3$/C positive material by one-step solid-state reaction. *Electrochim. Acta* **2009**, *54*, 2253–2258.

[469] Qiao, Y. Q.; Wang, X. L.; Zhou, Y.; Xiang, J. Y.; Zhang, D.; Shi, S. J.; Tu, J. P. Electrochemical performance of carbon-coated $Li_3V_2(PO_4)_3$ cathode materials derived from polystyrene-based carbon-thermal reduction synthesis. *Electrochim. Acta* **2010**, *56*, 510–516.

[470] Wang, J.; Liu, J.; Yang, G.; Zhang, X.; Yan, X.; Pan, X.; Wang, R. Electrochemical performance of $Li_3V_2(PO_4)_3$/C cathode material using a novel carbon source. *Electrochim. Acta* **2009**, *54*, 6451–6454.

[471] Qiao, Y. Q.; Wang, X. L.; Xiang, J. Y.; Zhang, D.; Liu, W. L.; Tu, J. P. Electrochemical performance of $Li_3V_2(PO_4)_3$/C cathode materials using stearic acid as a carbon source. *Electrochim. Acta* **2011**, *56*, 2269–2275.

[472] Rui, X. H.; Ding, N.; Liu, J.; Li, C.; Chen, C. H. Analysis of the chemical diffusion coefficient of lithium ions in $Li_3V_2(PO_4)_3$ cathode material. *Electrochim. Acta* **2010**, *55*, 2384–2390.

[473] Rui, X. H.; Li, C.; Chen, C. H. Synthesis and characterization of carbon-coated $Li_3V_2(PO_4)_3$ cathode materials with different carbon sources. *Electrochim. Acta* **2009**, *54*, 3374–3380.

[474] Chang, C.; Xiang, J.; Shi, X.; Han, X.; Yuan, L.; Sun, J. Rheological phase reaction synthesis and electrochemical performance of $Li_3V_2(PO_4)_3$/carbon cathode for lithium ion batteries. *Electrochim. Acta* **2008**, *53*, 2232–2237.

[475] Jiang, T.; Pan, W.; Wang, J.; Bie, X.; Du, F.; Wei, Y.; Wang, C.; Chen, G. Carbon coated $Li_3V_2(PO_4)_3$ cathode material prepared by a PVA assisted sol–gel method. *Electrochim. Acta* **2010**, *55*, 3864–3869.

[476] Chen, Y.; Zhao, Y.; An, X.; Liu, J.; Dong, Y.; Chen, L. Preparation and electrochemical performance studies on Cr-doped $Li_3V_2(PO_4)_3$ as cathode materials for lithium-ion batteries. *Electrochim. Acta* **2009**, *54*, 5844–5850.

[477] Rui, X. H.; Li, C.; Liu, J.; Cheng, T.; Chen, C. H. The $Li_3V_2(PO_4)_3$/C composites with high-rate capability prepared by a maltose-based sol–gel route. *Electrochim. Acta* **2010**, *55*, 6761–6767.

[478] Kuang, Q.; Zhao, Y.; An, X.; Liu, J.; Dong, Y.; Chen, L. Synthesis and electrochemical properties of Co-doped $Li_3V_2(PO_4)_3$ cathode materials for lithium-ion batteries. *Electrochim. Acta* **2010**, *55*, 1575–1581.

[479] Wang, L.; Li, Z.; Xu, H.; Zhang, K. Studies of $Li_3V_2(PO_4)_3$ additives for the $LiFePO_4$-based Li ion batteries. *J. Phys. Chem. C* **2008**, *112*, 308–312.

[480] Ren, M.; Zhou, Z.; Gao, X.; Peng, W. X.; Wei, J. P. Core–Shell $Li_3V_2(PO_4)_3$@C composites as cathode materials for lithium-ion batteries. *J. Phys. Chem. C* **2008**, *112*, 5689–5693.

[481] Zheng, J.-C.; Li, X.-H.; Wang, Z.-X.; Guo, H.-J.; Hu, Q.-Y.; Peng, W.-J. $Li_3V_2(PO_4)_3$ cathode material synthesized by chemical reduction and lithiation method. *J. Power Sources* **2009**, *189*, 476–479.

[482] Zhang, L.; Wang, X. L.; Xiang, J. Y.; Zhou, Y.; Shi, S. J.; Tu, J. P. Synthesis and electrochemical performances of $Li_3V_2(PO_4)_3$/(Ag+C) composite cathode. *J. Power Sources* **2010**, *195*, 5057–5061.

[483] Tang, A.; Wang, X.; Liu, Z. Electrochemical behavior of $Li_3V_2(PO_4)_3$/C composite cathode material for lithium-ion batteries. *Mater. Lett.* **2008**, *62*, 1646–1648.

[484] Liu, H.; Gao, P.; Fang, J.; Yang, G. $Li_3V_2(PO_4)_3$/graphene nanocomposites as cathode material for lithium ion batteries. *Chem. Commun.* **2011**, *47*, 9110–9112.

[485] Cho, A. R.; Son, J. N.; Aravindan, V.; Kim, H.; Kang, K. S.; Yoon, W. S.; Kim, W. S.; Lee, Y. S. Carbon supported, Al doped-$Li_3V_2(PO_4)_3$ as a high rate cathode material for lithium-ion batteries. *J. Mater. Chem.* **2012**, *22*, 6556–6560.

[486] Liu, H.; Yang, G.; Zhang, X.; Gao, P.; Wang, L.; Fang, J.; Pinto, J.; Jiang, X. Kinetics of conventional carbon coated-$Li_3V_2(PO_4)_3$ and nanocomposite $Li_3V_2(PO_4)_3$/graphene as cathode materials for lithium ion batteries. *J. Mater. Chem.* **2012**, *22*, 11039–11047.

[487] Sun, C.; Rajasekhara, S.; Dong, Y.; Goodenough, J. B. Hydrothermal synthesis and electrochemical properties of $Li_3V_2(PO_4)_3$/C-based composites for lithium-ion batteries. *ACS Appl. Mater. Interfaces* **2011**, *3*, 3772–3776.

[488] Xun, S.; Chong, J.; Song, X.; Liu, G.; Battaglia, V. S. $Li_4P_2O_7$ modified high performance $Li_3V_2(PO_4)_3$ cathode material. *J. Mater. Chem.* **2012**, *22*, 15775–15781.

[489] Zhang, L.-L.; Liang, G.; Peng, G.; Zou, F.; Huang, Y.-H.; Croft, M. C.; Ignatov, A. Significantly improved electrochemical performance in $Li_3V_2(PO_4)_3$/C promoted by SiO_2 coating for lithium-ion batteries. *J. Phys. Chem. C* **2012**, *116*, 12401–12408.

[490] Saravanan, K.; Lee, H. S.; Kuezma, M.; Vittal, J. J.; Balaya, P. Hollow α-$LiVOPO_4$ sphere cathodes for high energy Li-ion battery application. *J. Mater. Chem.* **2011**, *21*, 10042–10050.

[491] Lii, K. H.; Li, C. H.; Cheng, C. Y.; Wang, S. L. Hydrothermal synthesis, structure, and magnetic properties of a new polymorph of lithium vanadyl(IV) orthophosphate: β-$LiVOPO_4$. *J. Solid State Chem.* **1991**, *95*, 352–359.

[492] Islam, M. S.; Dominko, R.; Masquelier, C.; Sirisopanaporn, C.; Armstrong, A. R.; Bruce, P. G. Silicate cathodes for lithium batteries: Alternatives to phosphates? *J. Mater. Chem.* **2011**, *21*, 9811–9818.

[493] Dominko, R.; Bele, M.; Kokalj, A.; Gaberscek, M.; Jamnik, J. Li_2MnSiO_4 as a potential Li-battery cathode material. *J. Power Sources* **2007**, *174*, 457–461.

[494] Nishimura, S.; Hayase, S.; Kanno, R.; Yashima, M.; Nakayama, N.; Yamada, A. Structure of Li_2MnSiO_4. *J. Am. Chem. Soc.* **2008**, *130*, 13212–13213.

[495] Belharouak, I.; Abouimrane, A.; Amine, K. Structural and electrochemical characterization of Li_2MnSiO_4 cathode material. *J. Phys. Chem. C* **2009**, *113*, 20733–20737.

[496] Boulineau, A.; Sirisopanaporn, C.; Dominko, R.; Armstrong, A. R.; Bruce, P. G.; Masquelier, C. Polymorphism and structural defects in Li_2MnSiO_4. *Dalton Trans.* **2010**, *39*, 6310–6316.

[497] Kuganathan, N.; Islam, M. S. Li2MnSiO4 Lithium battery material: Atomic-scale study of defects, lithium mobility, and trivalent dopants. *Chem. Mater.* **2009**, *21*, 5196–5202.

[498] Eames, C.; Armstrong, A. R.; Bruce, P. G.; Islam, M. S. Insights into changes in voltage and structure of Li_2FeSiO_4 polymorphs for lithium-ion batteries. *Chem. Mater.* **2012**, *24*, 2155–2161.

[499] Sirisopanaporn, C.; Masquelier, C.; Bruce, P. G.; Armstrong, A. R.; Dominko, R. Dependence of Li_2FeSiO_4 electrochemistry on structure. *J. Am. Chem. Soc.* **2011**, *133*, 1263–1265.

[500] Armstrong, A. R.; Kuganathan, N.; Islam, M. S.; Bruce, P. G. Structure and lithium transport pathways in Li_2FeSiO_4 cathodes for lithium batteries. *J. Am. Chem. Soc.* **2011**, *133*, 13031–13035.

[501] Ensling, D.; Stjerndahl, M.; Nytén, A.; Gustafsson, T.; Thomas, J. O. A comparative XPS surface study of Li_2FeSiO_4/C cycled with LiTFSI- and $LiPF_6$-based electrolytes. *J. Mater. Chem.* **2009**, *19*, 82–88.

[502] Lv, D.; Wen, W.; Huang, X.; Bai, J.; Mi, J.; Wu, S.; Yang, Y. A novel Li_2FeSiO_4/C composite: Synthesis, characterization and high storage capacity. *J. Mater. Chem.* **2011**, *21*, 9506–9512.

[503] Zuo, P.; Wang, T.; Cheng, G.; Cheng, X.; Du, C.; Yin, G. Effects of carbon on the structure and electrochemical performance of Li_2FeSiO_4 cathode

materials for lithium-ion batteries. *RSC Adv.* **2012**, *2*, 6994–6998.

[504] Li, L.; Guo, H.; Li, X.; Wang, Z.; Peng, W.; Xiang, K.; Cao, X. Effects of roasting temperature and modification on properties of Li_2FeSiO_4/C cathode. *J. Power Sources* **2009**, *189*, 45–50.

[505] Muraliganth, T.; Stroukoff, K. R.; Manthiram, A. Microwave-solvothermal synthesis of nanostructured Li_2MSiO_4/C (M = Mn and Fe) cathodes for lithium-ion batteries. *Chem. Mater.* **2010**, *22*, 5754–5761.

[506] Huang, X.; Chen, H.; Zhou, S.; Chen, Y.; Yang, J.; Ren, Y.; Wang, H.; Qu, M.; Pan, Z.; Yu, Z. Synthesis and characterization of nano-$Li_{1.95}FeSiO_4$/C composite as cathode material for lithium-ion batteries. *Electrochim. Acta* **2012**, *60*, 239–243.

[507] Yan, Z.; Cai, S.; Zhou, X.; Zhao, Y.; Miao, L. Sol–gel synthesis of nanostructured Li_2FeSiO_4/C as cathode material for lithium ion battery. *J. Electrochem. Soc.* **2012**, *159*, A894–A898.

[508] Kam, K. C.; Gustafsson, T.; Thomas, J. O. Synthesis and electrochemical properties of nanostructured Li_2FeSiO_4/C cathode material for Li-ion batteries. *Solid State Ionics* **2011**, *192*, 356–359.

[509] Zhang, S.; Deng, C.; Yang, S. Preparation of nano-Li_2FeSiO_4 as cathode material for lithium-ion batteries. *Electrochem. Solid-State Lett.* **2009**, *12*, A136–A139.

[510] Deng, C.; Zhang, S.; Fu, B. L.; Yang, S. Y.; Ma, L. Characterization of Li_2MnSiO_4 and Li_2FeSiO_4 cathode materials synthesized via a citric acid assisted sol–gel method. *Mater. Chem. Phys.* **2010**, *120*, 14–17.

[511] Gong, Z. L.; Li, Y. X.; He, G. N.; Li, J.; Yang, Y. Nanostructured Li_2FeSiO_4 electrode material synthesized through hydrothermal-assisted sol–gel process. *Electrochem. Solid-State Lett.* **2008**, *11*, A60–A63.

[512] Rangappa, D.; Murukanahally, K. D.; Tomai, T.; Unemoto, A.; Honma, I. Ultrathin nanosheets of Li_2MSiO_4 (M = Fe, Mn) as high-capacity Li-ion battery electrode. *Nano Lett.* **2012**, *12*, 1146–1151.

[513] McDowell, M. T.; Lee, S. W.; Harris, J. T.; Korgel, B. A.; Wang, C.; Nix, W. D.; Cui, Y. In situ TEM of two-phase lithiation of amorphous silicon nanospheres. *Nano Lett.* **2013**, *13*, 758–764.

[514] Liu, N.; Wu, H.; McDowell, M. T.; Yao, Y.; Wang, C.; Cui, Y. A yolk–shell design for stabilized and scalable Li-ion battery alloy anodes. *Nano Lett.* **2012**, *12*, 3315–3321.

[515] Wang, F.; Yu, H.-C.; Chen, M.-H.; Wu, L.; Pereira, N.; Thornton, K.; van der Ven, A.; Zhu, Y.; Amatucci, G. G.; Graetz, J. Tracking lithium transport and electrochemical reactions in nanoparticles. *Nat. Commun.* **2012**, *3*, 1201.

[516] Ceder, G.; Hautier, G.; Jain, A.; Ong, S. P. Recharging lithium battery research with first-principles methods. *MRS Bull.* **2012**, *37*, 185–191.

[517] Roberts, M.; Johns, P.; Owen, J.; Brandell, D.; Edstrom, K.; El Enany, G.; Guery, C.; Golodnitsky, D.; Lacey, M.; Lecoeur, C. et al. 3D lithium ion batteries—from fundamentals to fabrication. *J. Mater. Chem.* **2011**, *21*, 9876–9890.

[518] Ma, D.; Cao, Z.; Wang, H.; Huang, X.; Wang, L.; Zhang, X. Three-dimensionally ordered macroporous FeF_3 and its in situ homogenous polymerization coating for high energy and power density lithium ion batteries. *Energy Environ. Sci.* **2012**, *5*, 8538–8542.

[519] Kang, D.-Y.; Kim, S.-O.; Chae, Y. J.; Lee, J. K.; Moon, J. H. Particulate inverse opal carbon electrodes for lithium-ion batteries. *Langmuir* **2013**, *29*, 1192–1198.

[520] Cheah, S. K.; Perre, E.; Rooth, M.; Fondell, M.; Hårsta, A.; Nyholm, L.; Boman, M.; Gustafsson, T.; Lu, J.; Simon, P.; Edström, K. Self-supported three-dimensional nanoelectrodes for microbattery applications. *Nano Lett.* **2009**, *9*, 3230–3233.

[521] Zhang, H.; Yu, X.; Braun, P. V. Three-dimensional bicontinuous ultrafast-charge and -discharge bulk battery electrodes. *Nat. Nanotechnol.* **2011**, *6*, 277–281.

[522] Shao, Y.; Park, S.; Xiao, J.; Zhang, J.-G.; Wang, Y.; Liu, J. Electrocatalysts for nonaqueous lithium–air batteries: Status, challenges, and perspective. *ACS Catal.* **2012**, *2*, 844–857.

[523] Lu, Y.; Gallant, B.; Kwabi, D.; Harding, J.; Mitchell, R.; Whittingham, M. S.; S-H, Y. Lithium–oxygen batteries: Bridging mechanistic understanding and battery performance. *Energy Environ. Sci.* **2013**, *6*, 750–768.

[524] Bruce, P. G.; Freunberger, S. A.; Hardwick, L. J.; Tarascon, J.-M. Li–O_2 and Li–S batteries with high energy storage. *Nat. Mater.* **2012**, *11*, 19–29.

[525] Girishkumar, G.; McCloskey, B.; Luntz, A. C.; Swanson, S.; Wilcke, W. Lithium−air battery: Promise and challenges. *J. Phys. Chem. Lett.* **2010**, *1*, 2193–2203.

[526] Shao, Y.; Ding, F.; Xiao, J.; Zhang, J.; Xu, W.; Park, S.; Zhang, J.-G.; Wang, Y.; Liu, J. Making Li–air batteries rechargeable: Material challenges. *Adv. Funct. Mater.* **2013**, *23*, 987–1004.

[527] Capsoni, D.; Bini, M.; Ferrari, S.; Quartarone, E.; Mustarelli, P. Recent advances in the development of Li–air batteries. *J. Power Sources* **2012**, *220*, 253–263.